



UNIVERSITY OF SHEFFIELD

ELECTRONIC & ELECTRICAL ENGINEERING

---

Growth optimisation of III-V semiconductors using  
bismuth as a surfactant and a constituent.

Thesis

---

*Author:*

Nicholas James Bailey

*1st Supervisor:*

Dr. Robert Richards

*2nd Supervisor:*

Prof. John David

December 15, 2022

A Thesis submitted for Doctorate of Philosophy to the Department of Electronic and  
Electrical Engineering.

## Acknowledgements

---

I would like to give my heartfelt thanks my supervisors, Doctor Robert Richards and Professor John David, who have kept my work on course through some particularly challenging and blighted years.

I am also deeply grateful to thank my colleagues in the dilute bismides group who are always available for help and advice, and Dr Edmund Clarke and Mr Richard Frith for humouring me with corridor MBE discussions.

My examiners, too, are deserving of earnest gratitude for battling through a particularly disjointed first submission and helping me turn this work from initial, manic ravings into something coherent and insightful.

Finally, and most of all, my family and fiancée, Hannah. They have supported me through all the low points of my work without being able to enjoy the high points.

## Abstract

---

Dilute bismide materials have been of interest for various applications including infra-red emitters, detectors and photovoltaics for many years. Incorporating bismuth into semiconductor materials is a challenge though, which requires abnormal growth conditions within a narrow window. This often leads to poor material quality which, despite the many reports in the literature on optimising the growth of this material; it is yet to be fully understood.

A major characteristic observed in bismide materials is the formation of a localised distribution of states above the valence band of the alloys containing it. The first experimental chapter explores this state distribution via low-temperature power-dependent photo-luminescence measurements. Through the development of an existing model and applying it to a comprehensive series gallium arsenide bismide layers the effect of growth temperature and bismuth flux on this distribution of localised states is analysed. From the modelling results it is shown that this technique can be used to predict the growth regime the layer was synthesised under and inform on the requirements for further optimising the growth conditions for devices.

The second experimental chapter investigates the impacts of bismuth in a more conventional regime. Here it is used as a surfactant during the growth of indium arsenide quantum dots on gallium arsenide at two different growth temperatures. The effect of changing the magnitude of the bismuth flux is investigated to provide deeper understanding of its influence on quantum dot nucleation. Atomic force microscopy results show that increasing the magnitude of the bismuth flux consistently increases the quantum dot height. At low growth temperatures, bismuth is shown to induce the formation of quantum dots where they would not form without it. Finally, combined surface and optical studies reveal an anomalous morphology transition in the quantum dot layer grown with a low bismuth flux at high temperature. The increased quantum dot aspect ratio in this layer is believed to be the cause of its unexpected red-shift in emission wavelength, relative to the other layers in the series.

The third experimental chapter details the growth of a quaternary alloy containing bismuth, aluminium gallium arsenide bismide. The quality of this material and the

way bismuth incorporates into it is compared to gallium arsenide bismide through the use of crystallographic and ion beam techniques. Results confirm that bismuth is incorporated substitutionally as in other ternary bismuth alloys. From the measurement of bismuth contents greater than achieved in gallium arsenide it is confirmed that the pathway of bismuth incorporation is not impeded by aluminium composition and it is predicted that this alloy could be grown at higher temperatures to further improve crystal quality.

## List of publications

---

### Peer reviewed publications

1. Y. Liu, X. Yi, **N. J. Bailey**, Z. Zhou, T. B. O. Rockett, L. W. Lim, C. H. Tan, R. D. Richards and J. P. R. David, Valence band engineering of *GaAsBi* for low noise avalanche photodiodes. *Nature Communications* **12.1**, 1-8 (2021)
2. R. D. Richards, **N. J. Bailey**, Y. Liu, T. B. O. Rockett, A. R. Mohmad, *GaAsBi*: From Molecular Beam Epitaxy Growth to Devices. *physica status solidi (b)*, (2022)
3. **N. J. Bailey**, T. B. O. Rockett, S. Flores, D. F. Reyes, J. P. R. David and R. D. Richards, Effect of MBE growth conditions on *GaAsBi* photoluminescence lineshape and localised state filling. *Scientific Reports* **12.1**, 1-8 (2022)
4. **N. J. Bailey**, M. R. Carr, J. P. R. David, R. D. Richards, Growth of *InAs(Bi)/GaAs* Quantum Dots Under a Bismuth Surfactant at High and Low Temperature. *Journal of Nanomaterials*, **2022** (2022)
5. S. Flores, D. F. Reyes, T. Ben, V. Braza, **N. J. Bailey**, M. R. Carr, R. D. Richards, D. Gonzalez, Exploring the formation of *InAs(Bi)/GaAs* QDs at two growth-temperature regimes under different *Bi* supply conditions. *Applied Surface Science* **607**, 154966 (2022)

### Poster presentations

1. **N. J. Bailey**, T. Wilson, T. B. O. Rockett, J. P. R. David, R. D. Richards, Modelling Localized State Distribution in *GaAsBi* across an Array of Growth Conditions. *UK Semiconductors*, (2019)
2. **N. J. Bailey**, N. A. Adham, M. R. Carr, E. Harbord and R. D. Richards, Extending the wavelength of *InAs* quantum dots using bismuth. *IOP Quantum Dot day*, (2021)
3. **N. J. Bailey**, T. B. O. Rockett, J. P. R. David, R. D. Richards, PL modelling of *GaAsBi* layers to assist with improving material quality in optoelectronic devices. *34th Semiconductor and Integrated Optoelectronics Conference (SIOE)*, (2021)
4. **N. J. Bailey**, M. R. Carr, N. A. Adham, E. G. H. Harbord, D. F. Reyes, G. Kusch, R. A. Oliver, J. P. R. David, R. D. Richards, Control of *InAs/GaAs* QD properties through the use of a Bi surfactant. *21st International Conference on Molecular Beam Epitaxy*, (2021)

### Oral presentations

1. Y Liu, R. D. Richards, **N. J. Bailey**, T. B. O. Rockett, M. R. Nawawi, Update on Sheffield bismides activity: Back to bismuth as usual. *UK MBE Working Party Group*, (2018)
2. **N. J. Bailey**, T. Wilson, T. B. O. Rockett, J. P. R. David, R. D. Richards, Effect of growth conditions on the shape of bismuth induced localized states in *GaAsBi*. *10th International Workshop on Bismuth-Containing Semiconductors*, (2019)

3. **N. J. Bailey**, E. Harbord, D. F. Reyes, G. Kusch, M. R. Carr, R. A. Oliver, S. Flores, T. Ben, D. Gonzalez and R. D. Richards, Bi surfactant for tailoring *InAs(Bi)* quantum dots. *15th Mid-Infrared Optoelectronic Materials and Devices*, (2021)
4. R. D. Richards, **N. J. Bailey**, Y. Liu, Z. Zhou, T. B. O. Rockett, C. H. Tan, J. P. R. David, Growth of Thick *GaAsBi* Diodes for Detectors. *21st International Conference on Molecular Beam Epitaxy*, (2021)
5. **N. J. Bailey**, M. R. Carr, J. Dulai, M. K. Sharpe, J. England, J. P. R. David and R. D. Richards, Molecular Beam Epitaxy growth of Aluminium Gallium Arsenide Bismide. *22nd International Conference on Molecular Beam Epitaxy*, (2022)

# CONTENTS

<b>I</b>	<b>Theoretical Background</b>	<b>14</b>
<b>1</b>	<b>A Brief Introduction to Bismuth</b>	<b>14</b>
<b>2</b>	<b>III-V Semiconductors</b>	<b>15</b>
2.1	Semiconductor Band Formation . . . . .	15
2.2	Common III-V Semiconductors and Alloying . . . . .	18
2.3	The PN Junction . . . . .	19
2.4	<i>GaAs</i> . . . . .	23
2.5	<i>InAs</i> . . . . .	23
2.5.1	<i>InAs</i> Quantum Dots on <i>GaAs</i> . . . . .	24
2.6	<i>AlAs</i> . . . . .	26
2.7	<i>GaAsBi</i> . . . . .	26
2.7.1	<i>GaAsBi</i> growth . . . . .	26
2.7.2	<i>GaAsBi</i> band gap . . . . .	28
2.7.3	<i>GaAsBi</i> for Telecommunications . . . . .	28
2.7.4	<i>GaAsBi</i> for Avalanche Photo-diodes . . . . .	29
2.8	<i>AlGaAsBi</i> . . . . .	31
2.8.1	<i>AlGaAsBi</i> for Avalanche Detectors . . . . .	31
<b>3</b>	<b>Molecular Beam Epitaxy</b>	<b>32</b>
3.1	Producing and Sustaining a Vacuum . . . . .	32
3.2	Molecular Sources and Generating a Molecular Beam . . . . .	34
3.3	Cell Temperature Control and Outgassing . . . . .	37
3.4	Automation . . . . .	37
3.5	III-V Growth overview . . . . .	38
3.6	Reflection High-Energy Electron Diffraction (RHEED) . . . . .	38
3.6.1	RHEED Measurements For Substrate Heater Calibration . . . . .	39
3.6.2	RHEED Measurements For Finding Growth Rates . . . . .	40
3.6.3	RHEED Measurements for $As_2:Ga$ 1:1 Calibration . . . . .	41
3.7	Heater Calibration Process . . . . .	43
3.8	Growth Rate Calibration . . . . .	46
<b>4</b>	<b>Material Characterisation</b>	<b>47</b>
4.1	Photo-luminescence . . . . .	47
4.1.1	The Varshni Relation . . . . .	48
4.2	X-ray Diffraction . . . . .	49
4.2.1	Diffraction theory . . . . .	49
4.2.2	Symmetric and Asymmetric scans . . . . .	52
4.2.3	Reciprocal Space Mapping . . . . .	55

4.3	Nomarski Microscopy . . . . .	57
4.4	Rutherford Backscattering Spectroscopy . . . . .	58
4.5	Atomic Force Microscopy . . . . .	60
4.6	Scanning Electron Microscopy . . . . .	61
4.6.1	Energy Dispersive X-ray Spectroscopy . . . . .	62
<b>II</b>	<b>Photo-luminescence Modelling of Localised States in <i>GaAsBi</i></b>	<b>67</b>
<b>5</b>	<b>Literature Review</b>	<b>67</b>
<b>6</b>	<b>Experimental Setup</b>	<b>68</b>
6.1	Growth Condition Layers . . . . .	68
6.2	PL Model . . . . .	70
6.3	Model Implementation . . . . .	76
6.4	Model Constraints, Finding The Best Fit and Calculating Error Bars . . . . .	79
<b>7</b>	<b>Results and Discussion</b>	<b>84</b>
<b>8</b>	<b>Conclusions</b>	<b>90</b>
<b>III</b>	<b><i>InAs(Bi)</i> Quantum Dot Growth</b>	<b>93</b>
<b>9</b>	<b>Literature Review</b>	<b>93</b>
<b>10</b>	<b>Growth and Analysis</b>	<b>94</b>
10.1	Layer Growth . . . . .	94
10.2	AFM Analysis . . . . .	96
10.3	PL Analysis . . . . .	103
<b>11</b>	<b>Results and Discussion</b>	<b>104</b>
11.1	AFM Results . . . . .	104
11.2	PL Results . . . . .	110
<b>12</b>	<b>Conclusions</b>	<b>113</b>
<b>IV</b>	<b>Growth of <i>AlGaAsBi</i> by MBE</b>	<b>118</b>
<b>13</b>	<b>Literature Review</b>	<b>118</b>
<b>14</b>	<b>Material Growth Conditions and Characterisation</b>	<b>118</b>
<b>15</b>	<b>Results and Discussion</b>	<b>119</b>
15.1	Nomarski Microscopy Results . . . . .	119
15.2	X-ray Diffraction Results . . . . .	128
15.3	Rutherford Backscattering Results . . . . .	129

15.4 XRD and RBS comparison . . . . .	131
15.5 Bismuth incorporation in <i>AlGaAs</i> . . . . .	133
<b>16 Conclusions</b>	<b>136</b>
<b>V Conclusions</b>	<b>138</b>
<b>VI Future Work</b>	<b>138</b>
<b>Glossary</b>	<b>140</b>

## LIST OF TABLES

6.1	STG3 series growth conditions. . . . .	69
7.1	PL modelling results: STG3 series best fit parameters. . . . .	87
10.1	QD series growth conditions . . . . .	95
11.1	Summary of STK7 AFM characterisation. . . . .	106
11.2	Summary of the QD PL characterisation. . . . .	113
14.1	Summary of STL4 growth conditions. . . . .	118
15.1	STL4 Rocking Curve FWHM . . . . .	129
15.2	Summary of STL4 RBS characterisation. . . . .	129
15.3	Comparison of <i>Al</i> and <i>Bi</i> compositions of the STL4 layers characterised by RBS and XRD. . . . .	133
15.4	STL4 and STG3 growth conditions for comparison . . . . .	134

## LIST OF FIGURES

1.1	Periodic table excerpt . . . . .	15
2.1	General band alignment for insulators, semiconductors and metals . . . . .	16
2.2	Indirect and direct band alignment . . . . .	17
2.3	Lattice constant and band gap relation for common semiconductor alloys. . . . .	18
2.4	Doping in <i>GaAs</i> . . . . .	20
2.5	PN Junction . . . . .	21
2.6	PN Junction - Forward Bias . . . . .	22
2.7	PN Junction - Reverse Bias . . . . .	22
2.8	Zinc blende unit cell . . . . .	23
2.9	SK growth process . . . . .	24
2.10	Effect of quantum confinement on the semiconductor band structure. . . . .	25
2.11	Lu growth model . . . . .	27
2.12	Lewis growth model. . . . .	28
2.13	Auger recombination. . . . .	29
2.14	Impact ionisation within an APD . . . . .	30
3.1	MBE-STM layout . . . . .	33
3.2	Substrate and cell positioning within the MBE-STM . . . . .	34
3.3	Knudsen effusion cell cross-section . . . . .	35
3.4	RHEED System. . . . .	39
3.5	Monolayer growth sequence. . . . .	40
3.6	Bismuth incorporation under $As_2$ and $As_4$ . . . . .	41
3.7	<i>GaAs</i> reconstruction map. . . . .	42
3.8	RHEED: Oxide Removed Surface. . . . .	43
3.9	RHEED: $(2 \times 4)$ Surface. . . . .	44
3.10	RHEED: <i>As</i> Capped Surface. . . . .	44
3.11	RHEED: $c(4 \times 4)$ Surface. . . . .	45
3.12	MBE-STM Heater Calibration . . . . .	45
3.13	MBE-STM Growth Rate Calibration . . . . .	46
4.1	Photo-luminescence Energy Diagram. . . . .	47
4.2	Photo-luminescence Practical Layout. . . . .	48
4.3	Varshni Example and Fit. . . . .	49
4.4	Bragg's law of diffraction. . . . .	50
4.5	Ewald sphere. . . . .	50
4.6	Limiting sphere for accessible reflections. . . . .	51
4.7	Symmetric diffraction scan . . . . .	52
4.8	Symmetric diffraction scan - theory . . . . .	53
4.9	Symmetric diffraction scan - example . . . . .	54
4.10	Asymmetric diffraction scan - layout . . . . .	54
4.11	Asymmetric diffraction scan - theory . . . . .	55

4.12	Strained and Relaxed epilayer diagram . . . . .	56
4.13	Example RSM . . . . .	57
4.14	Nomarski microscopy examples . . . . .	58
4.15	RBS Shadow Cone Formation . . . . .	59
4.16	Atomic Force Microscopy block diagram . . . . .	60
4.17	Atomic Force Microscopy tip convolution diagram . . . . .	61
4.18	Scanning Electron Microscope block diagram . . . . .	62
6.1	Dopant luminescence correction . . . . .	69
6.2	Explanation of PL model from an initial classical direct band diagram layout . . . . .	70
6.3	Single distribution fitting by Wilson <i>et al.</i> . . . . .	72
6.4	Raw Power Dependent PL from the Growth Temperature Series . . . . .	73
6.5	Raw Power Dependent PL from the Bismuth Flux Series . . . . .	74
6.6	Model Illustration with representative PL . . . . .	75
6.7	PL Brute Force Model UI . . . . .	78
6.8	<i>GaAsBi</i> Alloy Fluctuation. . . . .	80
6.9	Primary model flowchart. . . . .	81
6.10	Ideal and Realistic Model Error . . . . .	82
6.11	PL Error Bar Model UI . . . . .	83
6.12	Error bar model flowchart. . . . .	84
7.1	Model fits to PL from the Growth Temperature Series . . . . .	85
7.2	Model fits to PL from the Bismuth Flux Series . . . . .	86
7.3	Trends in Fitting parameters Vs <i>Bi</i> content. . . . .	88
7.4	Trends in Fitting parameters Vs <i>Bi</i> coverage. . . . .	89
10.1	Quantum dot layer structure . . . . .	95
10.2	Nanoscope software limitations . . . . .	97
10.3	User interface for MATLAB particle detection software. . . . .	98
10.4	Comparison of detection settings on map of detected particles. . . . .	100
10.5	AFM UI Particle Correction Window . . . . .	101
10.6	AFM UI Particle Correction 3D Viewer . . . . .	102
10.7	AFM Particle Splitting . . . . .	103
11.1	Quantum dot AFM images . . . . .	105
11.2	Quantum dot height histograms . . . . .	107
11.3	Quantum dot density versus <i>Bi</i> flux . . . . .	108
11.4	Quantum dot aspect ratio charts . . . . .	109
11.5	Quantum dot equivalent deposition thickness Vs <i>Bi</i> flux . . . . .	110
11.6	QD PL comparison . . . . .	112
11.7	Integrated QD PL comparison . . . . .	113
14.1	General Growth Structure of the STL4 layer series. . . . .	119
15.1	<i>AlGaAsBi</i> Nomarski: STL46 . . . . .	120
15.2	<i>AlGaAsBi</i> Nomarski: STL43 . . . . .	121
15.3	<i>AlGaAsBi</i> Nomarski: STL47 . . . . .	122

15.4	<i>AlGaAsBi</i> Nomarski: STL4A . . . . .	123
15.5	<i>AlGaAsBi</i> Nomarski: STL49 . . . . .	124
15.6	<i>AlGaAsBi</i> Nomarski: STL4G . . . . .	125
15.7	<i>AlGaAsBi</i> Nomarski: STL4H . . . . .	126
15.8	<i>AlGaAsBi</i> Nomarski: STL4J . . . . .	127
15.9	30% <i>Al</i> rocking curves . . . . .	128
15.10	RBS Spectra: STL46 and STL4J . . . . .	130
15.11	STL4G Substitutional Profile . . . . .	131
15.12	STL4 $\omega - 2\theta$ Fitting . . . . .	132
15.13	STL4 Rocking Curve FWHM Vs <i>Bi</i> and <i>Al</i> Content . . . . .	133
15.14	STL4 <i>Bi</i> incorporation efficiency . . . . .	135
15.15	<i>GaAsBi</i> reported growth temperatures and <i>Bi</i> contents . . . . .	136

# DECLARATION

I, the author, confirm that this Thesis is my own work. I am aware of the University's Guidance on the Use of Unfair Means ([www.sheffield.ac.uk/ssid/unfair-means](http://www.sheffield.ac.uk/ssid/unfair-means)). This work has not been previously presented for an award at this, or any other, university.

# THESIS INTRODUCTION

The aim of this thesis is to further develop the literature understanding on the use of bismuth as a constituent element in semiconductor alloys. Bismuth alloys have unique benefits which make them materials of interest for future energy-efficient and sustainable electronic devices, as will be discussed later. Despite this, the growth of bismuth containing alloys still requires further study with regard to optimising the quality of material produced and understanding how their quality is impacted by the growth conditions used. Therefore, the objectives of this work are to build upon the current literature work of the most studied bismuth alloy, gallium arsenide bismide, to add to the limited literature coverage on the use of bismuth in quantum dot growth, both as a surfactant and constituent, and finally to establish foundation work on the growth of an as yet undocumented quaternary alloy, aluminium gallium arsenide bismide, which has potential in next-generation photo-detectors. These subjects will be dealt with in separate experimental chapters, but before this, there is a summary of the theoretical knowledge and techniques which underpin this work.

## PART I

# THEORETICAL BACKGROUND

This part of the thesis covers the core theoretical knowledge which this work is based on. Primarily this includes a summary of semiconductor physics and an introduction to the semiconductor materials which are used in this work. Following this is an overview of the molecular beam epitaxy (MBE) growth process by which these materials are synthesised. Finally, the material characterisation techniques which are used to observe and measure various structural and optical properties of these materials are discussed.

## 1 A BRIEF INTRODUCTION TO BISMUTH

Bismuth (*Bi*) is a post-transition metal sitting below antimony (*Sb*) in the group V elements on the periodic table with an atomic number of 83. It liquefies at  $\sim 271^\circ\text{C}$  and has a boiling point of  $\sim 1564^\circ\text{C}$ . *Bi* containing semiconductors were first experimented with in the 1950s when synthesis indium bismide (*InBi*) was first reported [1, 2]. Since then *Bi* has been incorporated into a variety of semiconductor materials including (but not limited to) indium antimonide (*InSb*), indium arsenide (*InAs*), and gallium arsenide (*GaAs*) [3].

13 IIIA 3A	14 IVA 4A	15 VA 5A
5 <b>B</b> Boron 10.811	6 <b>C</b> Carbon 12.011	7 <b>N</b> Nitrogen 14.007
13 <b>Al</b> Aluminum 26.982	14 <b>Si</b> Silicon 28.086	15 <b>P</b> Phosphorus 30.974
31 <b>Ga</b> Gallium 69.723	32 <b>Ge</b> Germanium 72.631	33 <b>As</b> Arsenic 74.922
49 <b>In</b> Indium 114.818	50 <b>Sn</b> Tin 118.711	51 <b>Sb</b> Antimony 121.760
81 <b>Tl</b> Thallium 204.383	82 <b>Pb</b> Lead 207.2	83 <b>Bi</b> Bismuth 208.980
113 <b>Nh</b> Nihonium [286]	114 <b>Fl</b> Flerovium [289]	115 <b>Mc</b> Moscovium [289]

Figure 1.1: Excerpt from the periodic table showing metal groups III, IV and V. The element of interest in this thesis, bismuth, has been highlighted in green.

## 2 III-V SEMICONDUCTORS

### 2.1 SEMICONDUCTOR BAND FORMATION

Semiconductors are crystalline materials made up of many atoms in an ordered, repeating structure. Due to the overlapping electron orbitals used in bonding, the available electron energy levels split from discrete states into quasi-continuous bands. This follows the Pauli exclusion principle which states that two fermions, in this case electrons, cannot have the same quantum numbers.

The highest energy band occupied by electrons is referred to as the valence band, and the lowest unoccupied energy level is referred to as the conduction band. Depending on the alignment of these bands, a material may be classed as a metal, a semiconductor or an insulator, as shown in Figure 2.1.

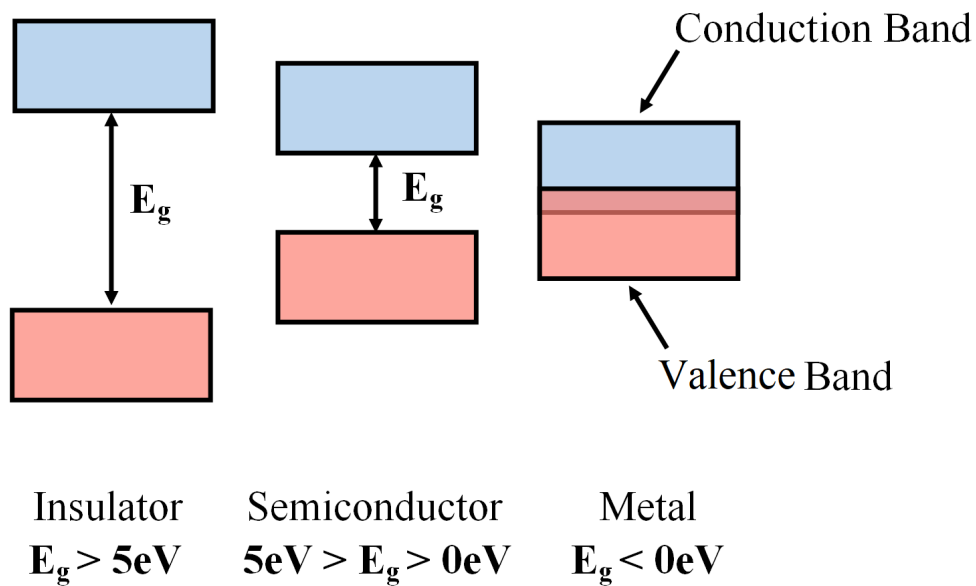


Figure 2.1: The general band alignments for insulators, semiconductors and metals. Approximated band gap energies are added for indicative purposes.

The actual band structures of semiconductors, however, are somewhat more complex than shown in Figure 2.1. A more descriptive depiction is shown in Figure 2.2. This shows the band diagrams for *Si* and *GaAs*. Whilst only the three higher, degenerate bands are displayed for *GaAs*; the valence band is made up of four sub-bands, when neglecting electron spin. The conduction band is also made up of multiple sub-bands as seen in Figure 2.2 [4].

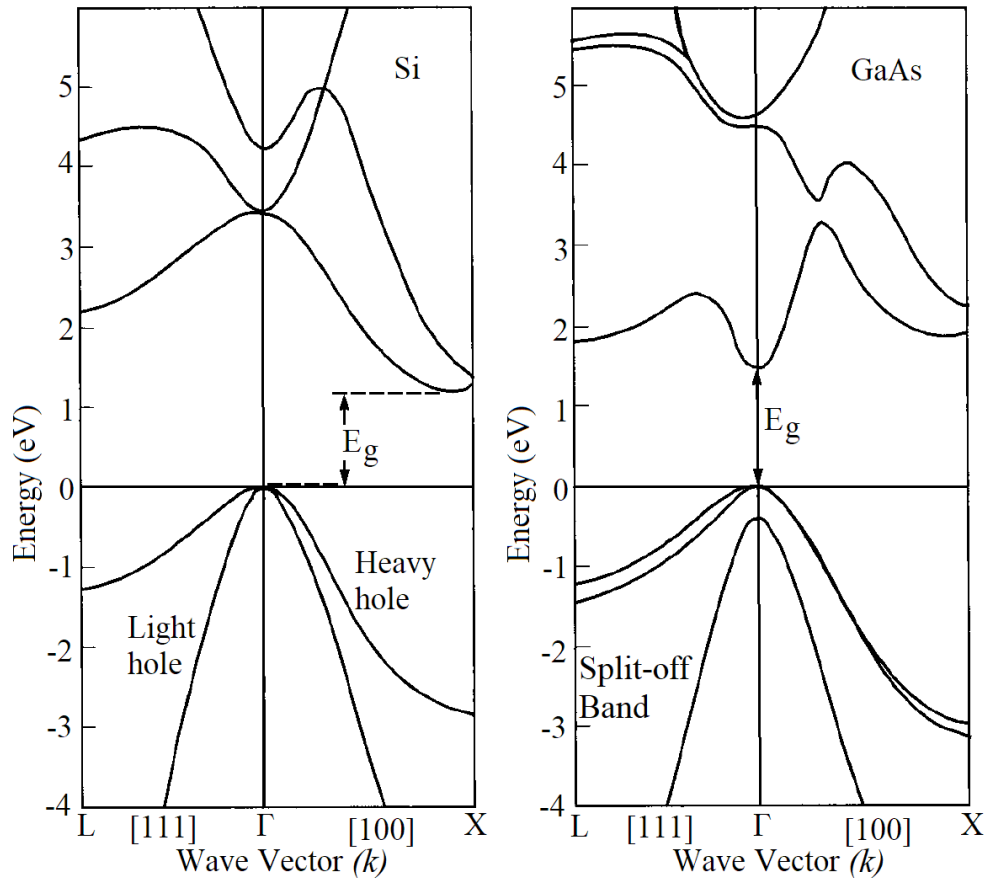


Figure 2.2: Energy gaps of *Si* and *GaAs* with respect to wave vector. The alignment of the conduction and valence bands shown for *GaAs* indicates a direct band gap. Adapted from [4].

As seen in Figure 2.2 for *Si* and *GaAs*, the conduction band minimum can occur at different  $k$  values. Where the conduction band minimum meets the valence band maximum, at  $k = 0$ , this results in a direct band gap. If the conduction band minimum occurs elsewhere,  $k \neq 0$ , this is an indirect band gap. Direct band gap materials are useful for optoelectronic applications as carrier energy transitions are much more likely to result in the emission or absorption of a photon. Indirect band gaps, however, involve more phonon interactions due to the difference in momentum between the bands.

Near the band edge, the  $E - k$  relationship is well approximated by Equation 2.1 [4]. Where  $m^*$  is the effective mass,  $\hbar$  is the reduced Planck's constant and  $k$  is the wave vector. From the form of Equation 2.1 it can be seen that the gradient of the plot is proportional to the inverse of the effective mass, hence the relative curvatures of the heavy and light hole bands.

$$E(k) = \frac{\hbar^2 k^2}{2m^*} \quad (2.1)$$

In addition to the allowed energy levels indicated by Figure 2.2 another important energy relation for semi-conductors is the density of states. This gives the density of available states for an electron with respect to energy. For a bulk, 3D-system without any quantum confinement, this is proportional to the square root of energy as shown in Equation 2.2, however, as will be seen in Section 2.5.1, this changes dramatically as carriers are confined.

$$N(E) = \frac{m^* \sqrt{2m^* E}}{\pi^2 \hbar^3} \quad (2.2)$$

## 2.2 COMMON III-V SEMICONDUCTORS AND ALLOYING

Figure 2.3 below displays the lattice constants and band gaps of some of the most common group IV and III-V semiconductors. The main materials of interest in this work are *GaAs*, *InAs*, aluminium arsenide (*AlAs*) and the various alloys which be made from them and *Bi*.

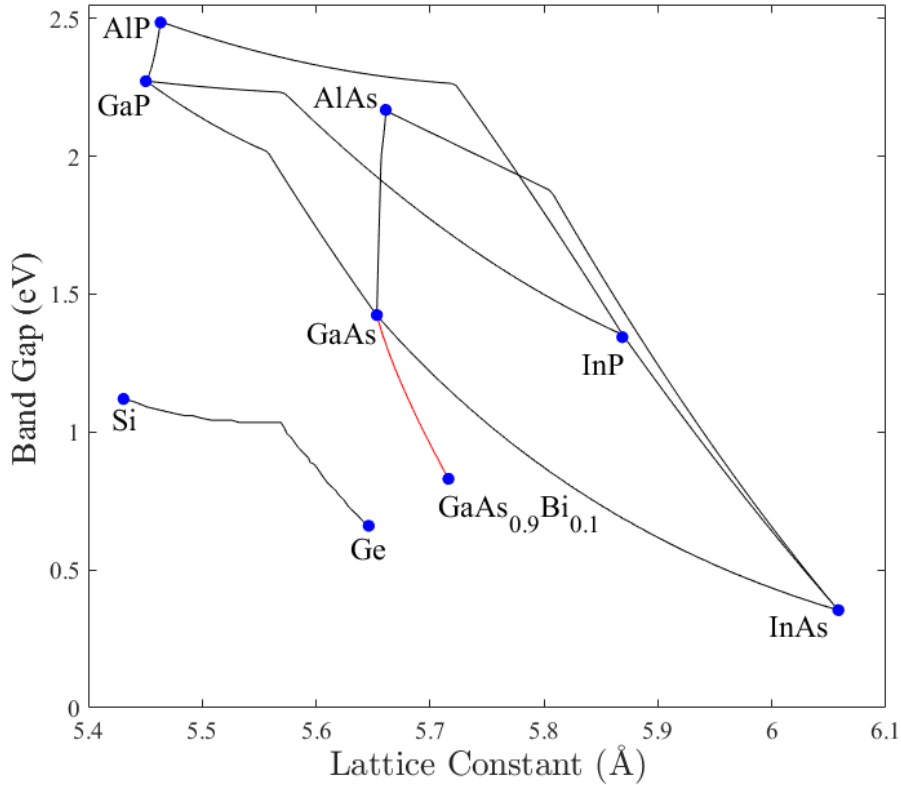


Figure 2.3: Lattice constant and band gap relation for multiple common semiconductor alloys [5]. Experimental data for  $\text{GaAs}_{1-x}\text{Bi}_x$  up to  $x = 0.1$  has been added (red line) [6].

As it has been established that the band structure is determined by the physical structure of the crystal lattice, it is also clear that physical changes to this lattice will therefore have a consequent effect on the band structure. These changes can be manifested as compressive or tensile strain imparted from surrounding semiconductor layers, environmental pressure which can be applied by sophisticated apparatus [7] or purely changes in atomic spacing due to ambient temperature. The effect of temperature is quite possibly the most widely known and will be shown in Section 4.1.1.

From Figure 2.3 it can be seen that when alloying two binary compounds to form a ternary alloy (the connecting black lines) the relationship between the lattice constant and band gap is not linear. It is generally accepted that the lattice constant of a ternary alloy is equivalent to the weighted mean of their individual lattice spacings,

this is called Vegards law. For example, the lattice constant of  $Al_xGa_{1-x}As$  can be calculated from the simple formula shown in Equation 2.3 [8].

$$Al_xGa_{1-x}As (\text{\AA}) = 5.6533 + 0.0078x \quad (2.3)$$

This same relation, however, does not apply to the band gap of a ternary compound. It is found that a non-linear relation must be used to describe the change in band gap. This leads to the addition of a ‘bowing parameter’ to the equivalent formula.

Still, even this relationship does not suit all ternary compounds. On close inspection to the alloy lines in Figure 2.3 it can be seen that for the many of the mixed III-V alloys and *SiGe* there are abrupt transitions between two different curves. The cause of this is a change in the relative minima of the different valleys of the conduction band. Where the  $\Gamma$ -valley is the lowest, at  $k = 0$ , the band gap is direct, as discussed earlier. In the case of  $Al_xGa_{1-x}As$  when  $x > 0.45$ , the X-valley minima becomes lower than that of the  $\Gamma$ -valley which causes the band gap to become indirect. This leads two different equations for the band gap depending on the composition, which are shown in Equation 2.4 and 2.5 [9].

$$Al_xGa_{1-x}As (x < 0.45)(eV) = 1.424 + 1.155x + 0.37x^2 \quad (2.4)$$

$$Al_xGa_{1-x}As (x > 0.45)(eV) = 1.9 + 0.124x + 0.144x^2 \quad (2.5)$$

## 2.3 THE PN JUNCTION

Whilst this thesis only deals with material characterisation of various semiconductor alloys grown with *Bi*, the scientific and commercial attraction of them is undoubtedly in their application to specific electronic devices. Therefore there will be discussion on some of the requirements and properties of these devices, which first necessitates an overview of the foundation of all electronic devices. Semiconductor doping and the PN junction.

An un-doped semiconductor is referred to as intrinsic and the distribution of free charge carriers within an ideal material is perfectly split between electrons and holes (bonding sites vacant of an electron which can move through the crystal lattice). Electrons and holes are the carriers which transfer negative and positive charge, respectively, through a semiconductor. Through doping of a semiconductor the balance between these carriers can be shifted and the material becomes extrinsic. Doping involves replacing a small fraction of the lattice atoms with different elements from different periodic table groups. For *GaAs* common dopants are silicon (*Si*) and beryllium (*Be*) which are incorporated as donor or acceptor atoms. These preferentially occupy *Ga* sites within the lattice and increase the number of electrons and holes, respectively. *GaAs* doped with *Si* therefore has a large number of free electrons and is referred to as n-doped, whereas *Be*-doped *GaAs* has a large number of holes and is referred to as p-doped. An illustration of *Be* and *Si* doping is shown in Figure 2.4.

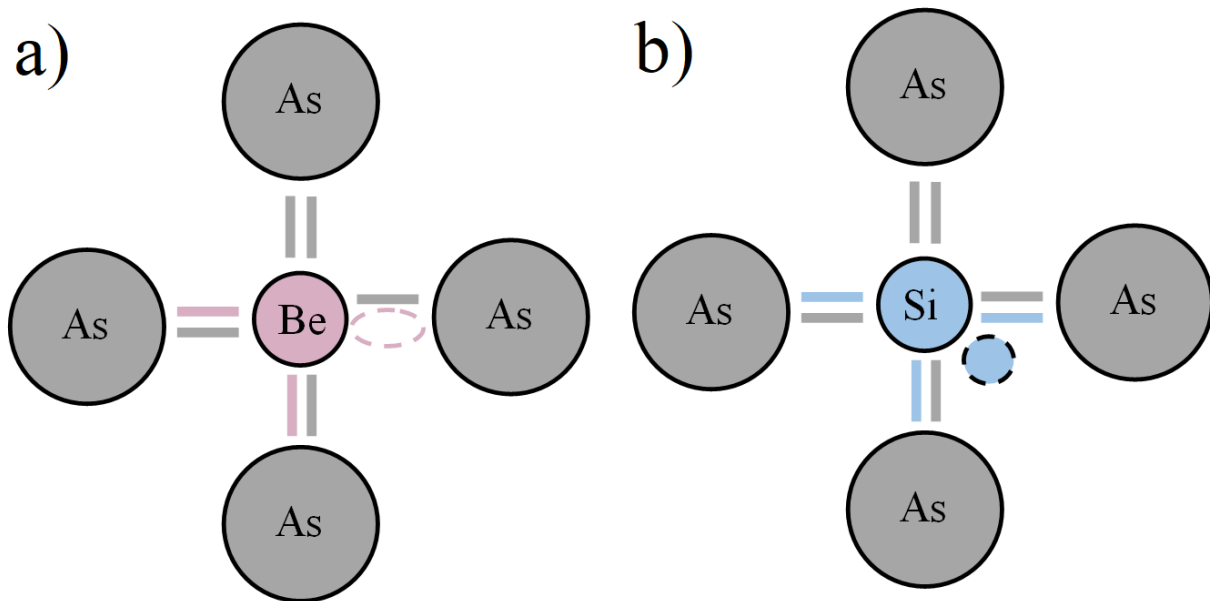


Figure 2.4: a) Be and b) Si doping in GaAs. Be, a group II element, leaves one acceptor state (pink dashed oval) which can accept an electron from a neighbouring Ga-As bond thereby producing a hole. Si, a group IV element, has a loosely bonded electron (blue dashed circle) which is easily delocalised producing a mobile electron within the lattice and therefore acts as a donor.

A PN junction is formed when a p-doped layer is connected with an n-doped layer, as shown in Figure 2.5. In reality this isn't actually how PN junctions are made, practically these layers are grown sequentially or produced using a post-growth doping method called ion implantation, but this example of two semiconductors being fused together makes the explanation much more convenient and straightforward.

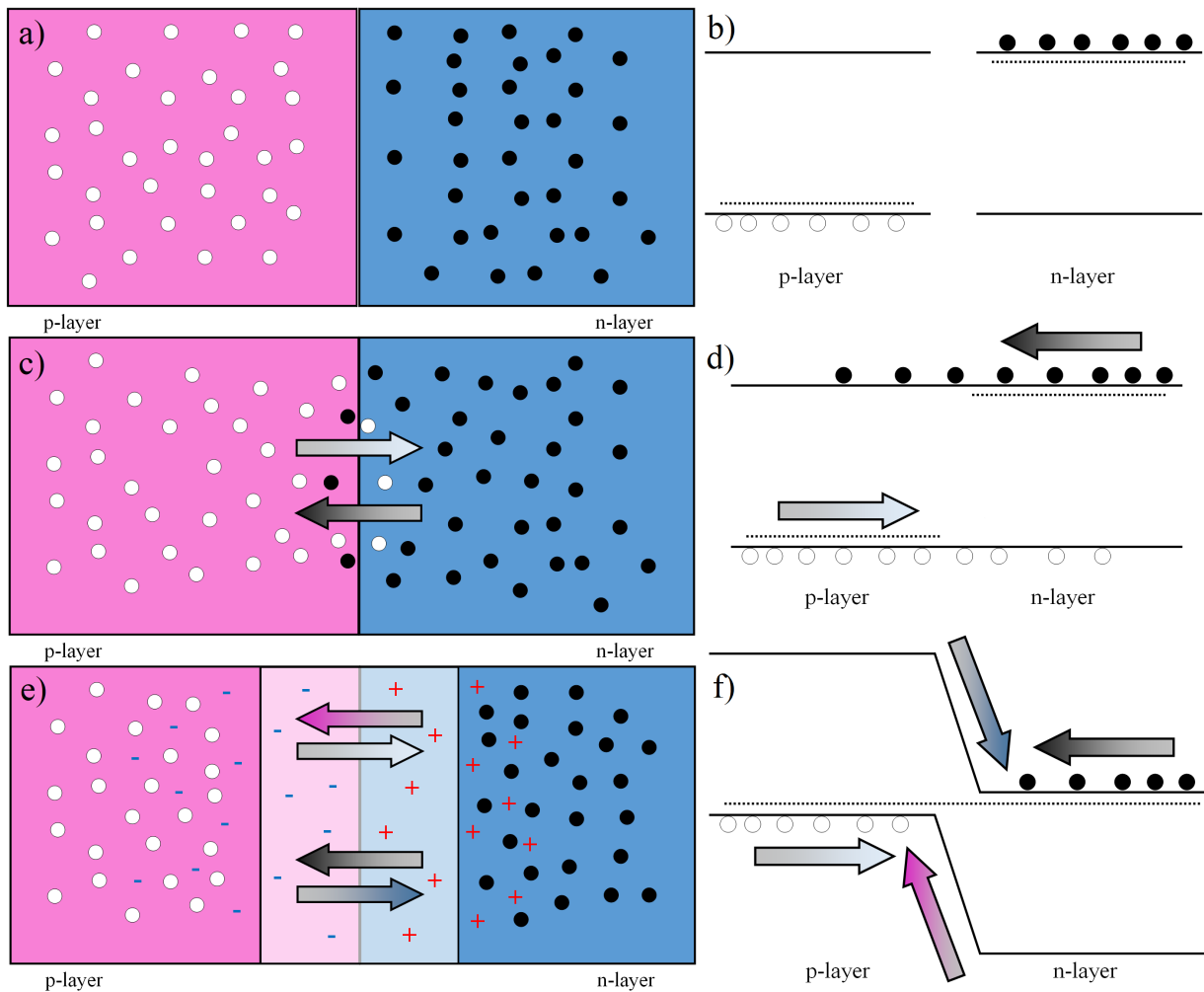


Figure 2.5: PN junction diagram at various stages which indicates the movement of electrons (filled circles) and holes (open circles). a) and b) demonstrate the initial concept of separate p and n materials. If connected, or an invisible barrier were removed, carriers would diffuse across the boundary as shown in c) and d). When the carriers recombine in these new regions an electric field is set up due to the net charge on the donor and acceptor nuclei, shown in e) and f). This electric field produces a drift current which equals and opposes the diffusion current, leaving the junction in equilibrium. The depletion region in the structure is marked with a translucent white rectangle.

In Figure 2.5 the left-hand side illustrates a physical example of a PN junction and the right-hand side shows a simplified band diagram for the structure. In 2.5a and 2.5b the two layers are separate with a uniform distribution of their respective majority carriers. When connected in 2.5c and 2.5d the electrons and holes begin to diffuse across the boundary as indicated by the white and black gradient arrows. As these charge carriers diffuse, the net charge left on the donor and acceptor becomes exposed, shown in 2.5e and 2.5f as red plus and blue minus symbols. This results in a potential difference and electric field which cancels out the diffusion current across the boundary with an equal and opposite drift current, as shown by the pink and blue coloured arrows. The area around this boundary is referred to as the depletion region where there essentially no free charge carriers and the material is highly resistive.

This equilibrium condition can be altered with the application of an external bias. If a positive voltage is applied to the p-region and a negative bias applied to the n-region, referred to as forward bias and shown in Figure 2.6, the internal electric field is reduced. This allows further diffusion across the junction, injecting minority carriers into each doped layer where they can recombine with the oppositely charged majority carriers. This recombination leads to the emission of photons in direct band gap materials and is the basis of the light emitting diode (LED).

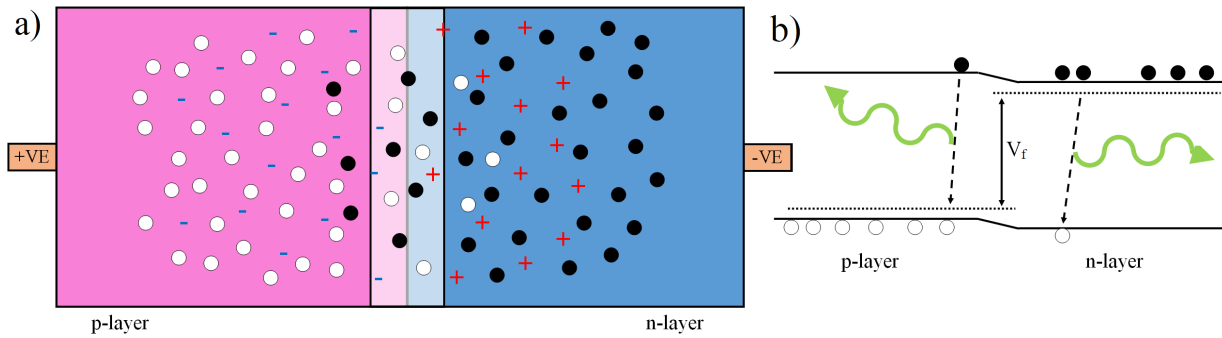


Figure 2.6: PN junction diagram under forward bias. a) Shows the reduction of the depletion region width and the transport of carriers across the PN junction. b) Illustrates the equivalent band diagram where the barrier to electrons and holes is reduced and a diffusion current flows across the junction, allowing minority carrier recombination and photon emission [10].

In the case of a reverse bias being applied, the electric field within the structure is increased. As shown in Figure 2.7. The depletion width of the junction is also increased due to majority carriers being attracted to the opposing charge applied to their terminals. Any carriers which are generated in the depletion region, by photon absorption for instance, are swept apart by the strong electric field to their respective majority regions. Holes are swept into the p-region and electrons to the n-region, which represents a net charge flow across the junction and through the device. This process is exploited using photo-detectors under reverse bias in order to measure photon intensity.

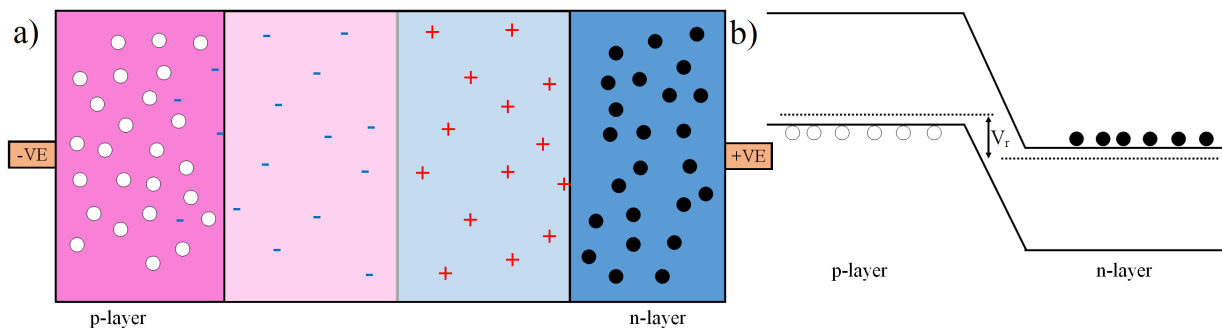


Figure 2.7: PN junction diagram under reverse bias. a) demonstrates how this widens the depletion region and attracts the holes and electrons to their respective terminals. b) displays an equivalent band diagram where .

In practice, a current will still be measurable through a reverse biased device even with no incident photo-

excitation. There are multiple causes for this. One is thermal excitation of carriers, this is a particular problem for long wavelength (narrow band gap material) detectors, which require cooling to reduce this current. Another is surface leakage where charge flows through un-passivated surface states of devices. At high reverse bias, large currents will also flow through the depletion region due to avalanche multiplication and can cause damage to the device in a process called avalanche breakdown. Collectively the currents which flow under a reverse bias with no intended excitation are referred to as the dark current, this is a metric often used for photodetectors and other diode based devices. Its magnitude can be related to the growth quality of the semiconductor layers, as well as the fabrication process, where poor growth and increased defect density lead to higher device dark currents.

In some applications the design of a PN (or equally NP) junction will include an un-doped (intrinsic, or I) region between the two doped layers. These are called PIN or NIP junction devices and have several benefits. These include reduced junction capacitance, higher breakdown voltages and increased detectivity for photo-detectors due to the thicker absorbing regions [10].

## 2.4 *GaAs*

*GaAs* is a III-V semiconductor with a direct, room-temperature band gap of  $1.424\text{ eV}$  and a lattice constant of  $5.6533\text{ \AA}$  (at  $300\text{ K}$ ). It forms a zinc blende structure as shown in Figure 2.8 which is equivalent to two face-centred cubic (FCC) sub-lattices, one of arsenic (*As*) and one of gallium (*Ga*), superimposed over each other with a relative displacement of  $5.6533\text{ \AA} / 4$  in the (001), (010) and (100) unit directions [11]. In a unit cell diagram it appears as a single FCC lattice with four tetrahedral interstices. Although there appears to be more of the light grey group in the unit cell; the corner and face centre atoms are shared between multiple cells and each unit cell actually contains four *As* and four *Ga* atoms.

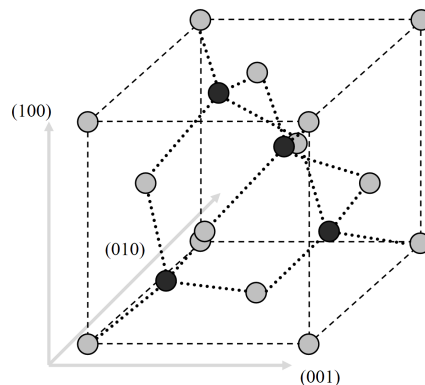


Figure 2.8: Zinc blende unit cell. FCC lattice (light grey) and tetrahedral interstices (dark grey).

## 2.5 *InAs*

*InAs* is another zinc blende III-V semiconductor. Structurally it is similar to *GaAs* but with a larger,  $6.0583\text{ \AA}$ , lattice constant and a much lower room-temperature direct band gap of  $0.354\text{ eV}$ . One of the primary applications of this binary semiconductor in III-V epitaxy is in the growth of quantum dots (QDs) on *GaAs*.

### 2.5.1 *InAs* QUANTUM DOTS ON *GaAs*

The nucleation of *InAs* QDs arises due to a shift between two different epitaxial growth modes during deposition. These are Frank-van der Merwe (FvdM) and Volmer-Weber (VM).

Consider a semiconductor substrate with a surface free energy of  $\gamma_1$ , upon which another semiconductor film with surface energy of  $\gamma_2$  is grown, inducing an interface energy of  $\gamma_{12}$ . There are two possible conditions from this which lead to either FvdM or VM growth [12]. The first is when  $\gamma_1 > \gamma_{12} + \gamma_2$  in which the deposited film will wet the surface and grow in the FvdM mode as a flat film. The second is when  $\gamma_1 < \gamma_{12} + \gamma_2$  where the deposited material forms 3D islands in VM growth.

The build up of strain induced by lattice mismatch in heteroepitaxial growth cannot be ignored from this process, however, and provides a third possibility. If the initial growth conditions satisfy  $\gamma_1 > \gamma_{12} + \gamma_2$ , for FvdM growth, then the initial monolayers of deposition will form a 2D wetting layer across the surface. With the addition of thickness dependent strain energy ( $\mu(t)$ ), then at a critical thickness ( $t_c$ ) the conditions may reverse to  $\gamma_1 < \gamma_{12} + \gamma_2 + \mu(t_c)$ . This can result in either strain reduction through dislocation formation or 3D island nucleation. Instances in which this results in 3D islands are referred to as Stranski-Krastanov (SK) growth. A simplified illustration of this is shown in Figure 2.9

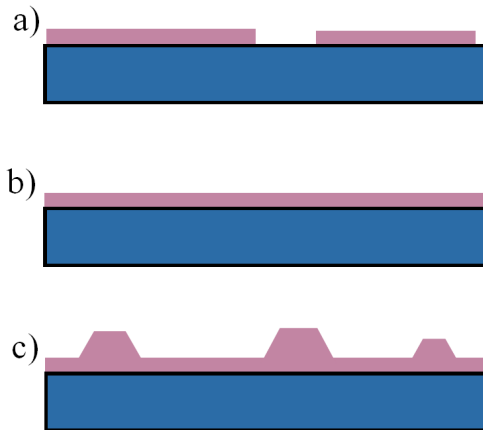


*Figure 2.9: Illustration of the Stranski-Krastanov growth process. a)-b) early growth proceeds as layer-by-layer but when past the critical thickness growth turns to c) island nucleation.*

*InAs* deposited on *GaAs* is one such instance of SK growth [13]. Historically this was reported to only occur on the (001) surface orientation of *GaAs* [14] and was discussed to be enabled by *In* – *Ga* alloying through substrate mass transport [15]. More recently, however, there have also been reports of 3D island nucleation on the (110) *GaAs* surface through the application of a surfactant during growth [16] or through the use of an *AlAs* intermediary layer [17].

The device applications of QDs have been of interest since they were suggested for improving the threshold current of lasers in the 1980's [18]. The source of this interest is from the unique density of states they exhibit due to quantum confinement in three dimensions. This is illustrated in Figure 2.10 for all levels of confinement

from bulk material, with three dimensions of freedom, down to QDs, with zero dimensions of freedom.

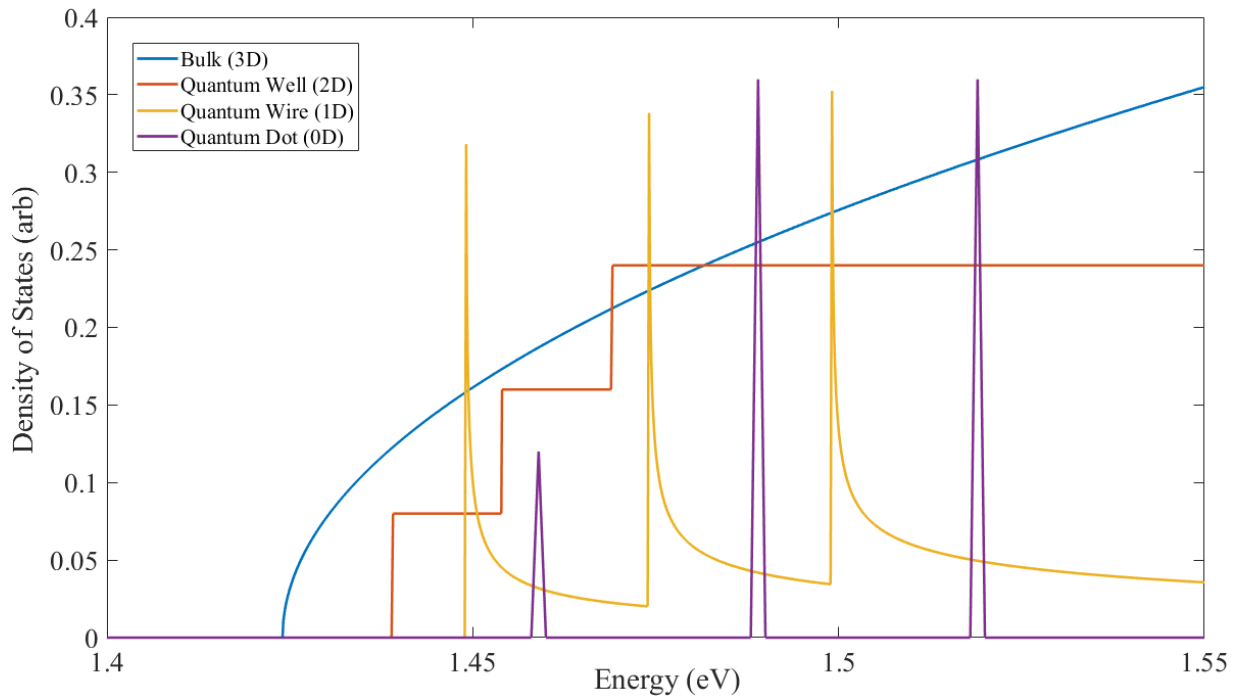


Figure 2.10: Illustration of the effect of quantum confinement. The example shown here is a general depiction of the density of states in *GaAs* at various dimensions of freedom.

There have been many literature reports investigating the synthesis and properties of QDs in various material systems, but particular attention has been paid to growing *InAs* QDs on *GaAs*. Two of the main reasons for this are:

1. *InAs* will readily nucleate QDs through strain-driven self-assembly, making them relatively simple to synthesise on *GaAs*.
2. The *GaAs* material system is a mature commercial technology and has access to near perfectly lattice-matched mirrors using *AlGaAs* superlattices. This is particularly useful for developing advanced optoelectronic devices.

There are some challenges with applying *InAs/GaAs* QDs to commercial devices though. These include:

1. Red-shifting QD emission into the desired wavelength bands - 1350 and 1500 *nm* for telecoms.
2. Controlling QD uniformity and density.

These issues and the techniques which have been studied to overcome them are further discussed later in Chapter III.

## 2.6 *AlAs*

*AlAs*, like *InAs* and *GaAs*, is another III-V semiconductor with a zinc blende structure. It has a room-temperature band gap of 2.12 eV and a lattice constant of 5.6611 Å. The interesting properties of this material are that its band gap, unlike *InAs* and *GaAs*, is indirect. This means that it has very little radiative recombination of excited electron-hole pairs due to the conduction band and valence band not being vertically aligned in k-space (momentum space). The other notable property of this material is that its lattice constant is almost identical to that of *GaAs* (0.118 % difference) meaning thick layers of *AlAs* can be grown on *GaAs* without issue, which allows for relatively easy grow of semiconductor mirrors as mentioned in Section 2.5.1.

These mirrors, referred to as distributed Bragg reflectors (DBRs), are extremely important in the production of semiconductor lasers, and other devices. Structurally DBRs are composed of a repeating superlattice of two semiconductor materials with differing refractive indices. By increasing the number of superlattice repetitions or the contrast in refractive indices, the reflectivity of these mirrors is increased.

## 2.7 *GaAsBi*

Gallium arsenide bismide (*GaAsBi*), as previously mentioned, is a ternary alloy of *GaAs*. It is formed when *Bi* bonds to *Ga* in sites normally occupied by *As* during *GaAs* growth. Out of the various *Bi* containing alloys, *GaAsBi* has attracted the most interest for the following reasons:

- *GaAsBi* could be grown to cover the 1.3 and 1.55  $\mu\text{m}$  wavelength ranges which are currently used in telecommunications.
- *GaAs* alloys are used in many multi-junction photovoltaic cells. Given the large initial band gap reduction caused by introducing *Bi*, there is the possibility for *GaAsBi* to be used to make a new small band gap junction for multi-junction solar cells, leading to improved efficiencies.
- *Bi* also causes a large, downward shift in the spin-orbit (SO) split-off band. When the SO splitting energy, the gap between the SO and valence band, is greater than the band gap ( $E_g$ ), Auger recombination and inter-valence band absorption is expected to be suppressed [3]. This would be particularly beneficial for telecommunication optoelectronics.

### 2.7.1 *GaAsBi* GROWTH

Growth of *GaAsBi* is not trivial and constricts growth conditions in several ways. The first is that due to a large miscibility gap and weak bonding energy between *Ga* and *Bi* [19], growth must be done at much lower temperatures than *GaAs*. This is because at higher temperatures normally used for *GaAs* growth ( $\sim 580^\circ\text{C}$ ) *Bi* is thermally ejected back onto the surface before it can be fully incorporated into the lattice [20]. As of writing, MBE growth of *GaAsBi* has only been reported at temperatures  $\leq 400^\circ\text{C}$  [21].

Another restriction which has been found is that to aid in *Bi* incorporation, stoichiometric *As* fluxes must be used. This can be done using  $\text{As}_4$ , which is the primary form of *As* sublimated from the bulk material, or the more commonly used, and thermally ‘cracked’,  $\text{As}_2$ . Research by Richards *et al.* has shown that while the *As*

flux is optimised for different atomic flux ratios of  $As_4$  or  $As_2$  compared to the same  $Ga$  flux, after accounting for the 0.5 sticking coefficient of  $As_4$  the conditions for both  $As$  species is around a unity incorporation rate of  $As:Ga$  [22]. The process limiting  $As_4$  incorporation during  $GaAs$  growth has long been reported in the literature and is believed to be due to the requirement for two adjacent  $As_4$  molecules which are chemisorbed on the  $GaAs$  surface to react, producing two  $As_2$  dimers on the surface which can incorporate and one  $As_4$  tetramer being ejected from the surface [23, 24].

There are two main models for  $GaAsBi$  growth which have been proposed. These were presented by Lu *et al.* [20] and Lewis *et al.* [19]. The Lu model considers three processes which are illustrated in Figure 2.11, the first is an incoming  $Ga$  atom which bonds to a  $As$  terminated site creating a  $As - Ga - Bi$  bond with a surface  $Bi$  adatom. The second process, where a  $Ga$  atom bonds between a  $Bi$  terminated site and  $Bi$  adatom is considered unfavourable and is discounted. The final process is an incoming  $As$  atom breaking a  $Ga - Bi$  bond and replacing it with a stronger  $Ga - As$  bond. From these processes at rate equation can be defined.

$$\frac{dx}{dt} \propto \theta_{Bi} F_{Ga} (1 - x) - a F_{As} e^{-\frac{U_1}{kT}} x \quad (2.6)$$

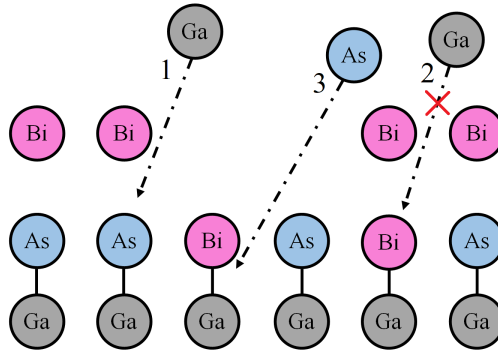


Figure 2.11: Lu model. Process 1 illustrates how  $Bi - Ga$  bonds are formed and the  $Bi$  content is increased at the growing surface. Process 3 shows how these bonds are replaced by stronger  $As - Ga$  bonds, reducing the  $Bi$  content. Adapted from [20].

Here  $\theta_{Bi}$  represents the surface coverage of  $Bi$ , between 0 - 1,  $F_{Ga}$  is the  $Ga$  flux, the  $(1 - x)$  factor accounts for the removal of process two, where  $x$  is the  $Bi$  content.  $F_{As}$  is the  $As$  flux,  $U_1$  is a characteristic energy for the  $Bi - Ga$  bond strength,  $T$  is the growth temperature and  $a$  and  $k$  are fitting constant and Boltzmann constant, respectively. It can be seen from Equation 2.6 how the modelled  $Bi$  content depends on the  $As$  flux and growth temperature where reducing either increases the  $Bi$  content. The limitation of this model is that it does not adequately describe the  $Bi$  content of layers grown at low  $As$  fluxes.

The subsequently developed Lewis model [19] instead sought to explain the growth of  $GaAsBi$  in terms of the surface coverage of  $Ga : As$ . An illustration of the model is shown in Figure 2.12 and equivalent rate equation in Equation 2.7.

$$\frac{dx}{dt} \propto \theta_{Ga} \theta_{Bi} - a_1 x F_{Ga} - a_2 x e^{-\frac{U_1}{kT}} \quad (2.7)$$

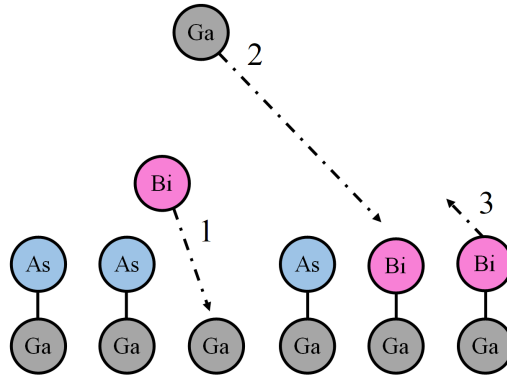


Figure 2.12: Lewis model. Process 1 displays Bi bonding to an exposed Ga site, this increases the Bi surface coverage and reduces that of Ga. Process 2 demonstrates a Ga atom bonding to a Bi site as part of the growth process and reducing the Bi surface coverage. Process 3 shows a Bi atom being thermally ejected to the surface, reducing the Bi surface coverage. Adapted from [19].

The nomenclature of Equation 2.7 follows that of 2.6 where  $\theta_{Bi/Ga}$  is the surface coverage of Bi/Ga respectively,  $F_{Ga}$  is again the Ga flux,  $x$  is the Bi content,  $U_1$  is an activation energy for ejecting Bi and  $a_{1/2}$  and  $k$  are general and the Boltzmann, respectively, constants. Under the reasoning that the rates of processes 1 and 3 were much larger than that of process 2, Lewis *et al.* ignored it in their work. This leaves the Bi content dependent on the As : Ga ratio and growth temperature which impacts the  $a_2 x e^{-\frac{U_1}{kT}}$  term.

### 2.7.2 GaAsBi BAND GAP

The band gap reduction in GaAsBi has been reported to be initially  $\sim 90 meV$  per % Bi [25, 26]. The cause of this reduction has been attributed to hybridisation between localised defect states associated with Bi and valence band states in GaAs [27, 28]. The presence of these localised states has been observed experimentally by various groups through a deviation to the Varshni relation of emission wavelength and lattice temperature (discussed in Section 4.1.1) [6, 29, 30, 31]. This is similar to what has also been seen in the dilute nitride alloy system [32].

At low temperatures, these states trap excitons (a bound state of a valence band hole and conduction band electron) at energies below the band gap. This leads to an anomalous red-shifting of the peak emission energy of the material which is discussed in more detail elsewhere [33]. This localisation is an important effect in GaAsBi and is discussed in the first experimental chapter, Chapter II.

### 2.7.3 GaAsBi FOR TELECOMMUNICATIONS

As mentioned in Section 2.7, there is interest in applying GaAsBi to devices for telecommunications. Current telecoms devices are based on indium gallium arsenide (*InGaAs*) grown on indium phosphide (*InP*) substrates. This has enabled the production of photo-detectors reaching as far as 1700 nm. *InP* is a less desirable material system than *GaAs*, though, for several reasons.

The first is that the *InP* substrates themselves are more expensive and fragile than *GaAs*. *GaAs* can be readily formed into ingots up to  $\sim 6$  inches in diameter [34], whereas current *InP* wafers are only commonly supplied in diameters of  $\sim 4$  inches [35].

Another benefit of the *GaAs* material system is, as mentioned in Section 2.5.1, the ease with which near lattice matched mirrors can be incorporated into device designs using *GaAs/AlAs* superlattices.

A key issue with *InP*-based telecoms devices are Auger recombination losses. This process can account for as much as 50 %, or higher, of the energy use in *InP* devices [36]. The result of this is a large amount of energy used in telecommunications being wasted on maintaining the temperature of the laser devices which are heated from these losses. Figure 2.13 illustrates this process where an electron recombines with a hole, moving from state  $E_{11}$  to  $E_{12}$ . Rather than this energy transition resulting in the emission of a photon it is transferred to another electron which is promoted from  $E_{21}$  to  $E_{22}$  from which it will return to back to the band edge through thermalisation losses. It should be noted that this process could also lead to the excitation of a second hole to a higher valence band state instead of an electron.

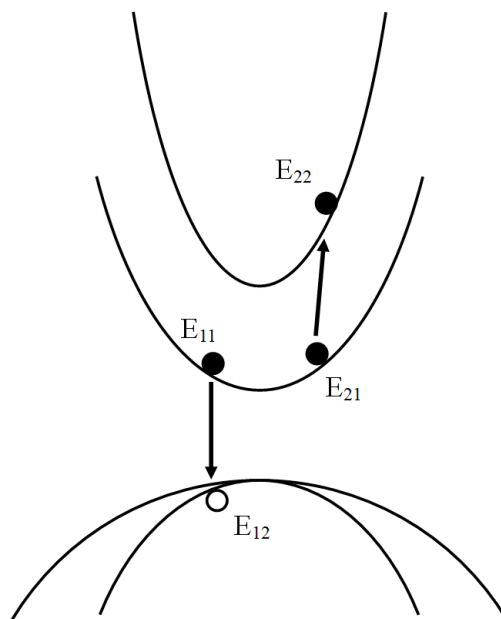


Figure 2.13: Illustration of the Auger recombination process.

The benefit which is offered by *Bi* here is that it shifts the band edge faster than the spin-orbit band per % of *Bi* incorporated and at  $\geq 10\%$  *Bi*, where  $E_g > SO$ , this process is expected to be suppressed [37].

#### 2.7.4 *GaAsBi* FOR AVALANCHE PHOTO-DIODES

Avalanche photo-diodes (APDs) are advanced versions of photo-detectors discussed in Section 2.3. They are highly sensitive detectors which exploit the process of impact ionisation to produce a large electrical signal from small optical excitation, even as low as a single photon. This process is illustrated in Figure 2.14 below.

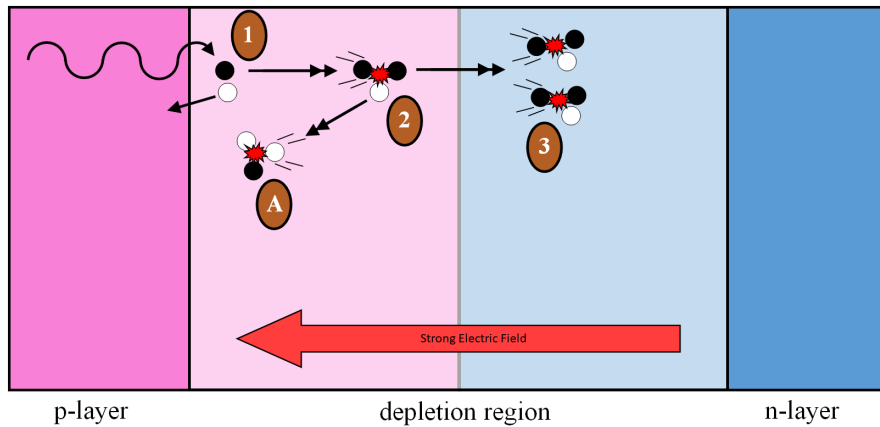


Figure 2.14: Impact ionisation events which occur within an APD. In process 1 the photo-excited electron (filled circle) is accelerated across the depletion region leading to an impact ionisation event, process 2, producing a new electron-hole pair. The two electrons present after this can then continue to accelerate on leading to an increasing number of impact ionisation events, process 3. An issue which can occur, however, is that the excited hole from process 2 can potentially also undergo an impact ionisation event, process A, which results in an electron being excited further back in the device. This electron can then undergo processes 2 and 3 which could in turn trigger further instances of process A. The persistence of this cyclical chain of events can lead to long decay times in avalanche detectors and requires the suppression of impact ionisation of either holes or electrons to prevent.

The conditions for impact ionisation are set up with high, reverse electric field applied to a PN junction. This results in an increase in the depletion width of the device. When an incoming photon is adsorbed it produces an electron-hole pair (process 1). In this example the hole is collected immediately in the p-layer and the electron is accelerated across the depletion region, gaining kinetic energy as it does so. If this electron undergoes a scattering event before reaching the n-layer, whilst it has sufficient energy, it will promote another electron to the conduction band which leaves a hole in the valence band (process 2), this is impact ionisation. The original electron and recently excited electron will then continue to accelerate and may impact ionise further resulting in an exponentially increasing current (process 3), hence the term ‘avalanche’ photo-diode. A problem occurs, however, when the holes excited in processes 2 and 3 accelerate and impact ionise (process A). Whilst this results in increased charge and therefore further amplification of the initial signal, it also results in the promotion of an electron nearer to the start of the depletion region. From here it can be seen how processes 2, 3 and A can persist for a long period, if not indefinitely. It is this cyclical process which can limit the bandwidth of an APD.

The solution to this is to tailor the multiplication region of the device to support impact ionisation of only one carrier (electrons or holes). The measure of this is the  $\alpha/\beta$  ratio where  $\alpha$  and  $\beta$  are parameters which represent the mean number of impact ionisation events, at a given field strength, for electrons and holes, respectively. If these values are similar then the ratio is close to 1 and processes 2, 3 and A can persist for a long time after the initial absorption event. If the ratio is small (low  $\alpha$  value) or large (low  $\beta$  value) then impact ionisation can be suppressed for one of the carriers at low reverse biases and a higher bandwidth device can be achieved.

Recently, work by Liu *et al.* [38] has shown that *Bi* contents up to  $\leq 5.1\%$  in *GaAs* produce a significant reduction in hole ionisation whilst having negligible impact on electron ionisation. This has been demonstrated through various electrical characterisation techniques including multiplication and excess noise measurements on *GaAsBi* devices of both PIN and NIP configuration and at various I-region thicknesses. A remaining issue with *GaAsBi* which restricts its use in APDs is the high dark currents present in device structures which is due to the low growth temperatures necessary for *Bi* incorporation.

## 2.8 *AlGaAsBi*

There is little literature discussion, as of writing, regarding the growth of *AlGaAsBi*. This has therefore been reserved for discussion in Chapter IV. Instead, the following brief subsection will highlight the potential interest in this alloy.

### 2.8.1 *AlGaAsBi* FOR AVALANCHE DETECTORS

As discussed in Section 2.7.4 *Bi* has been shown to produce a large improvement in the  $\alpha/\beta$  ratio in *GaAs*, through the reduction of  $\beta$ . Within this same material system it has also been shown that high fractions of *Al* in *AlGaAs* also lead to an improvement in  $\alpha/\beta$  through the reduction of  $\beta$  [39]. Therefore it can be expected that a combination of these effects in an *AlGaAsBi* avalanche device would result in further improvements. As there has been little growth work on this alloy, however, it is important to investigate its growth to observe any deviations from the better understood alloy *GaAsBi*. It is this which forms the basis of the work reported in Chapter IV.

### 3 MOLECULAR BEAM EPITAXY

MBE is a growth technique which has been used since the 1970s to produce high quality semiconductor layers, with excellent control on thickness [40, 41]. The key elements to this growth technique are:

- A growth chamber sustaining an ultra-high vacuum.
- Several cells containing high purity elemental sources.
- Shutters to allow abrupt changes in molecular flux to a substrate.
- A sample stage with an integrated substrate heater.
- Multiple thermocouples and power supplies to monitor and maintain the various substrate and cell temperatures.

During growth, material in the cells is raised to a temperature where significant sublimation or evaporation occurs and the shutters are opened to allow the material to reach the substrate which is heated in the sample stage. After migrating on the surface briefly, adatoms bond to exposed lattice sites on the substrate forming new semiconductor unit cells. Throughout the rest of this chapter further detail will be given to the various and important areas of this growth process.

#### 3.1 PRODUCING AND SUSTAINING A VACUUM

Maintaining the ultra-high vacuum within an MBE growth chamber is a key factor in producing high quality semiconductor layers as reactive species ( $O_2, H_2, H_2O, CO, CO_2$ ) can incorporate into the growing crystal lattice and introduce a variety of defects [40]. This requires the use of a variety of pumping systems.

- Scroll or Diaphragm pumps: These operate between 1000 *mbar* (atmospheric pressure) and  $\sim 5 \times 10^{-3}$  *mbar* and are often referred to as ‘roughing’ or ‘backing’ pumps. They are primarily used for initial pumping of chambers after they have been exposed to atmospheric pressure. After this they remain running to maintain the low exhaust pressure required by turbo-molecular pumps.
- Turbo-molecular pumps: These take over from ‘roughing’ pumps and make use of extended mean free paths at low pressure and molecular drag to pump gasses at high vacuum [42]. In order to be effective these pumps run at high rotational speeds of  $\geq 750$  *Hz*.
- Cryo pumps or cryo shrouds: Both cryo pumps and cryo shrouds use super-cooled surfaces which act as freezing traps, collecting material from within the chamber [42]. Despite this similarity, there are differences in how they are operated. Cryo pumps use a liquid helium compressor to drive a heat pump which allows them to cool to a minimum temperature of  $\sim 4$  *K* but common practice is for cryo shrouds to be liquid nitrogen ( $LN_2$ ) fed through a vacuum feed-through due to their larger surface area within the chamber. These shrouds therefore have a minimum temperature of  $\sim 80$  *K* but are generally operated at  $\sim 180$  *K*.
- Titanium sublimation pumps: A titanium (*Ti*) sublimation pump exploits the getter effect of *Ti* to trap gas species within the chamber. The pump consists of a set of *Ti*-coated filaments which are ‘fired’ in

the vacuum using ohmic heating and sublimate  $Ti$  which then coats the inside walls of the chamber. Loose gas species around the chamber then bind to this sputtered  $Ti$ , reducing the chamber pressure. An important note is to fit these pumps with a baffle in order to prevent deposition of  $Ti$  on delicate in-vacuum electronics.

- Ion getter pumps: These pumps work in two stages. First a high electric field ( $3 - 7\text{ kV}$ ) is generated between two terminals, gas species within the chamber which enter this high electric field are ionised, causing their electrons to be drawn to the anode and their nuclei drawn to the cathode which is made of a getter material. When a nucleus crashes into the cathode with sufficient force it implants itself in the cathode and sputters some of the cathode material onto the pump wall where it can bind with other loose species within the chamber [42].

The MBE system used to grow layers throughout this work is an Omicron MBE-STM reactor. It is fitted with multiple vacuum pumps, including turbo-molecular pumps backed with scroll pumps, a titanium sublimation pump, an ion pump and a cryo shroud which lines the inside of the growth chamber. The installation layout of these pumps in the two main chambers are shown in Figure 3.1.

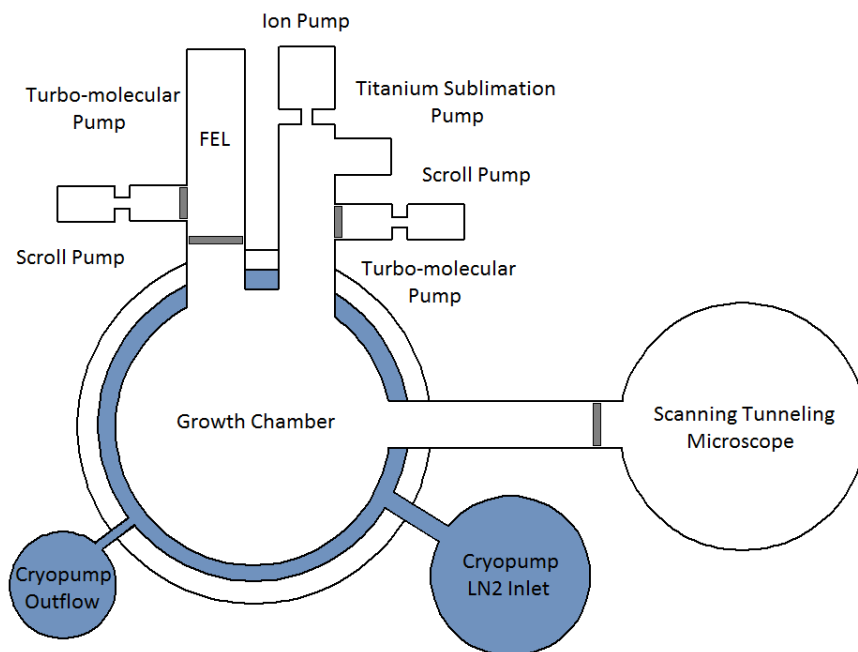


Figure 3.1: Diagram of general pump positioning within the MBE-STM system. The gate valves used to isolate chambers and pumps within the system are represented as filled grey rectangles. The scanning tunnelling microscope connected to the growth chamber was not used in this work and has therefore not been filled out.

There are three main chambers to this system. These are the Fast Entry Load-lock (FEL), the growth chamber and the Scanning Tunnelling Microscope (STM). The STM is not currently functioning, though, and will not be discussed further.

The FEL is the entry chamber to the system. It is routinely brought to atmospheric pressure and is therefore

designed to have a small volume to reduce the time taken to pump down back to vacuum. Finished layers are brought into this chamber when their growth is complete and they are ready to be removed and exchanged with a fresh substrate. During exchange, it is sealed off from the growth chamber and FEL turbo by gate valves, then a dry nitrogen feed is opened into the FEL, bringing it to pressure of  $\sim 1.3 \text{ bar}$ . After this, the blanking flange covering the access port to the FEL is loosened until the nitrogen inside begins to leak out. The blanking flange is then completely removed and the substrates exchanged. Once re-sealed the nitrogen line is closed and the FEL is pumped back down to  $\sim 1 \times 10^{-7} \text{ mbar}$  using the dedicated turbo and backing pump.

The growth chamber, as the name suggests, is where the substrates have new material epitaxially deposited on their surface. It is under vacuum for the longest period of time and has the most pumps attached.

### 3.2 MOLECULAR SOURCES AND GENERATING A MOLECULAR BEAM

To generate the molecular fluxes required for growth extremely high purity elemental sources are required. The purity of the source material is quoted as ‘#N’ where ‘#’ indicates the number of significant figures of purity (i.e. 5N = 99.999% pure). Figure 3.2 below gives a general indication of how the cells are arranged in the growth chamber with respect to the substrate.

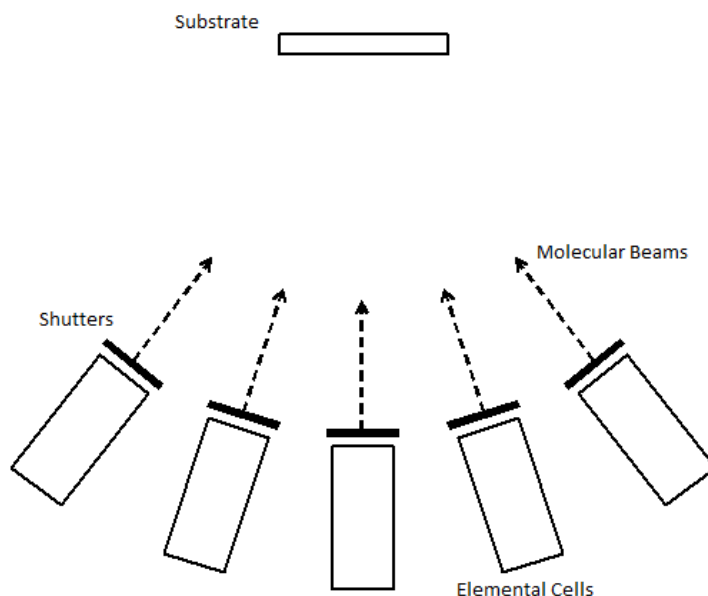


Figure 3.2: Substrate and cell positioning within the MBE reactor. Adapted from [41].

One of the key requirements from a MBE system is that the source beams have high stability. Given source material of sufficient purity the generation of the elemental beam from the bulk is typically performed by a thermal process. Heating the material up inside the vacuum will increase the material’s vapour pressure and eventually a significant flux will be evaporated or sublimated, depending on whether the source is liquid or solid at the given temperature, from the bulk. The traditional apparatus which holds the bulk source material and controls the beam flux through radiative heating is a Knudsen effusion cell.

For a Knudsen effusion cell with a well-defined geometry, the molecular flux output of the cell can be expressed as shown in Equation 3.1 [40].

$$J (\text{atoms cm}^{-2} \text{ s}^{-1}) = 1.118 \times 10^{22} \frac{p \times A}{l^2 \times (M \times T)^{1/2}} \quad (3.1)$$

Where  $p$  (*Torr*) is the source vapour pressure,  $A$  ( $\text{cm}^{-2}$ ) is the cell aperture area,  $l$  ( $\text{cm}$ ) is distance between the cell and the substrate,  $M$  is the source molecular weight and  $T$  ( $\text{K}$ ) is the source temperature. Models have also been used to account for flux non-uniformity across the substrate surface due to non-normal incidence of impinging fluxes and this has been shown to be useful in mapping the effects of growth conditions on semiconductors grown in stationary positions [43].

Beyond the simple theory of a Knudsen cell is significant effort which has been put into the design on this vital MBE component. This includes subtle design features to allow them to run at high temperatures and shield neighbouring cells from thermal interference. An annotated cross-section of a Knudsen cell is shown in Figure 3.3.

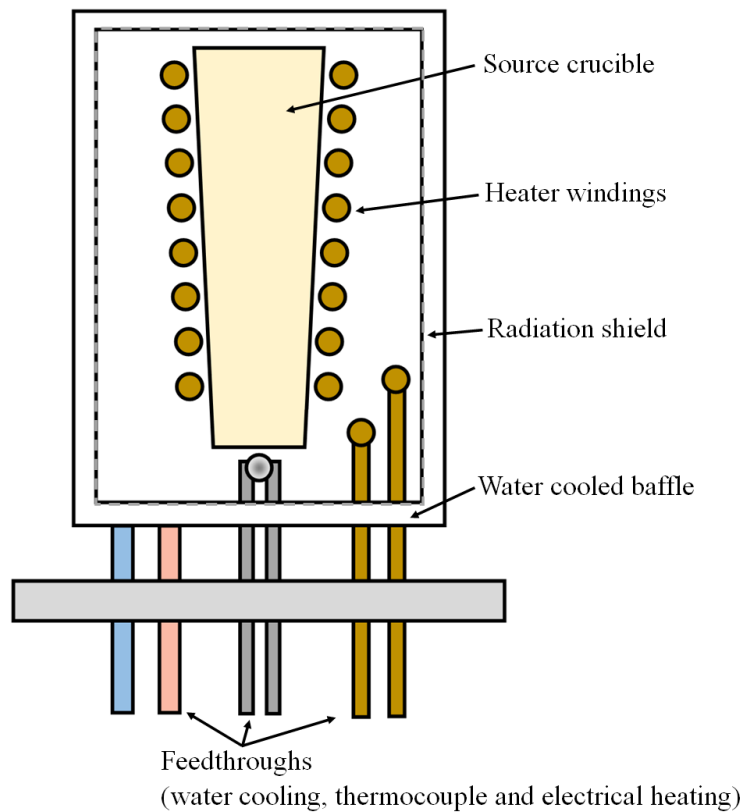


Figure 3.3: A generalised Knudsen effusion cell cross-section.

The use of refractory metals, such as molybdenum, tantalum and tungsten, is common to a large number of MBE components as for temperatures exceeding  $150\text{ }^{\circ}\text{C}$  impurities including manganese, magnesium and chromium are often seen to be released from stainless steel [40]. A similar restrictive material selection process is applied to electrical insulation materials, with the primary victor being pyrolytic boron nitride (PBN).

PBN can be produced with impurity levels  $< 10 \text{ ppm}$  and although this material breaks down above  $1400 \text{ }^\circ\text{C}$ , these temperatures are rarely used and the nitrogen released has not yet been observed to have a significant impact on layer properties. Currently PBN is the preferred material for source crucibles and has been used as electrical insulation around substrate heaters. Alternative materials which have found selective use are graphite and quartz.

To measure the cell temperature in-vacuum during operation, thermocouples are commonly used. These are type-k, which are made of nickel and chromium and can operate in a temperature range of  $0 - 1200 \text{ }^\circ\text{C}$  over which they will output a voltage of  $0 - 50 \text{ mV}$ . This voltage is translated back to a temperature by an analogue-to-digital converter.

The water cooled baffle surrounding the cell is used to capture and remove thermal radiation lost from the cell which would otherwise interfere with the temperatures of adjacent cells. The water network, which feeds the cells on a reactor, operate at low pressures ( $\sim 1.3 \text{ Bar}$ ) and at temperatures ranging from  $14 - 30 \text{ }^\circ\text{C}$ .

In addition to the standard Knudsen cell depicted in Figure 3.3, some sources are modified with a high temperature channel following the crucible and are called ‘dissociation cells’, often instead referred to as a ‘cracker’ cell. These are used for group V sources, such as *As* where the species which sublimates from the bulk is a tetramer ( $As_4$ ). In this cell, sublimated material from the *As* bulk source is directed through a heated channel in the temperature range of  $650 - 1000 \text{ }^\circ\text{C}$ . During molecular collisions between the  $As_4$  tetramers and the walls of this channel there is a probability that the tetramer will split into two  $As_2$  dimers. Through careful design to ensure multiple collisions during transit these cracker cells can reliably output single species beams of  $As_2$  or  $As_4$  depending on the cracker temperature. Whilst cracker cells are sometimes used on other group V elements, they are not widely used for *Bi* cells as the species inherently produced are  $Bi_2$  dimers and *Bi* monomers [44].

Measurement of the molecular flux produced by a cell at a given temperature is performed by an ion gauge which is placed in the direct path of the molecular beam near the focal point of all the cells, where the substrate would be. This flux measurement is based on the change in the ionisation current through the ion gauge before and after the cell shutter is opened. Cell shutters are opened one at a time so the ion gauge detects the flux from each cell individually. The output of the ion gauge is displayed on its controller as a pressure (in units of *mbar* or *Torr*).

Ion gauge readings of fluxes are taken as beam equivalent pressures (BEPs). They are not a direct measurement of the flux and cannot be compared against other cell fluxes with different materials without accounting for differences in ionisation efficiency. They can, however, be used to characterise an individual cell’s behaviour as BEPs from a specific cell and ion gauge can be compared for an individual reactor. As a general guide for the BEP expected for different cells during operation, group III and *Bi* cells are operated in the  $1 \times 10^{-8} - 5 \times 10^{-7} \text{ mbar}$  range and *As* cells in the range of  $1 \times 10^{-7} - 1 \times 10^{-5} \text{ mbar}$ .

### 3.3 CELL TEMPERATURE CONTROL AND OUTGASSING

If the material cells were left at operational temperature when not growing they would quickly run out of material, making downtime and maintenance much more frequent. Instead, when there is going to be a significant gap between growths (overnight or over the weekend) the cells are cooled to a rest temperature to prevent wasting material. Depending on the material this is between 100 – 600 °C below operational temperature. The limits to this are the freezing points of some of the molten sources such as *Al* and *Bi* which limits the rest temperatures to 850 and 300 °C, respectively, once they have been liquefied.

The issue caused by this is that gas species loose in the chamber will condense on the cooling cells. This condensate will be readily released back into the chamber when the cell is reheated to operational temperature and if released during growth these impurities could react with the growing material and introduce defects into the lattice. To prevent these impurities degrading growth quality the cells are heated up to  $\sim 20$  °C above their operational temperature and outgassed prior to a substrate being loaded into the chamber. This rapidly releases the foreign material into the chamber so it can be pumped away before loading. The marginally increased temperature ensures that contaminants which would evaporate at the same temperature of the source material are released quickly and contaminants which have much higher vapour pressures than the source material are undisturbed.

Outgassing is significantly more important after a machine has been brought down for maintenance as it will have been exposed to atmospheric pressure and will have absorbed a substantial amount of reactive species [40]. This process varies depending on individual preference but often begins with a 48 *hour* bake-out of the system where it is heated up to  $\sim 200$  °C whilst being pumped. There is some disagreement on whether MBE chambers should be baked, however, due the risk of damaging delicate equipment and warping gasket interfaces. The purpose of the bake-out is to remove as much moisture as possible from the system as the desorption rate of water is exponentially higher during a bake-out than at room temperature. It has also been reported that purging and pumping an MBE reactor with dry nitrogen at least once before being opened for maintenance to help prevent moisture build up as well as diluting any residual toxic gasses. Purging is also useful after the chamber has been closed to remove some moisture which will have condensed inside.

### 3.4 AUTOMATION

In the previous sections there has been lots of discussion on the different and complex facets of MBE growth. Fortunately advancements in computer processing power and automation since the early development of MBE has made operation of these systems less cumbersome. Cell temperatures and shutters can be fully automated allowing for growth recipes to be run for many hours without human intervention. Digital logging of measured fluxes and remote access to desktop computers has even enabled the recording of flux data without an operator even needing to be in the same room as the reactor. Using fibre-optic sensors and servo motors it is even possible, on some reactors, to automate the loading and exchanging of substrates within a vacuum system. However, this final technology is not available on the MBE reactor used in this work.

### 3.5 III-V GROWTH OVERVIEW

Now the engineering and automation aspects of MBE have been covered, a summary on the growth of III-V compounds can be given.

Where the growth temperature is below the congruent sublimation temperature of a III-V compound it is assumed that the group III material has a sticking coefficient of 1 and only enough group V material sticks to satisfy this supply, with excess molecules being desorbed back into the vacuum [40]. In this way the growth of III-V compound semiconductors can be said to be group III limited, where the total flux of group III material dictates the growth rate of the crystal. This makes the alloying of group III metals relatively easy as the solid phase composition of the alloy is almost entirely dictated by the fluxes of the individual metals. Alloying group V metals is harder, however, with the growth of *Bi* containing alloys particularly challenging as previously discussed in Section 2.7.

Prior to its use as a constituent, *Bi* also had applications in MBE as a surfactant. *Bi* has been used as a surfactant for *InGaAs/GaAs* heterostructures [45], where it reduced surface roughness and improved PL intensity, as well as *Ge/Si* growth [46] where it was found to suppress 3D islanding and segregation of *Ge*. Surfactants are materials which do not readily incorporate under typical growth conditions for a material, but which do have a large impact of the way a material grows. In essence, a surfactant acts as an adsorbed species which alters the surface free energy and growth kinetics of a material [47]. They can be categorised as either ‘reactive’ or ‘non-reactive’ depending on if they decrease or increase adatom migration length during growth. Another key difference is that reactive surfactants sit on lattice sites whereas non-reactive surfactants sit interstitially. Therefore *Bi* is a reactive surfactant as it sits on *As* sites during *GaAs* growth and when it is discussed in *GaAsBi* literature that *Bi* is segregated to the surface, it is possible that it will also begin to act as a surfactant during growth.

### 3.6 REFLECTION HIGH-ENERGY ELECTRON DIFFRACTION (RHEED)

The main in-situ tool for monitoring the condition of a substrate during MBE growth is Reflection High-Energy Electron Diffraction (RHEED). This technique uses a collimated beam of electrons which have been accelerated to energies of 10 – 20 keV incident to the substrate at a small grazing angle on the order of 2 – 3 °. Due to the low incident angle the electron beam is diffracted by only the top few monolayers of the substrate [48]. This produces a diffraction pattern of the surface of the sample on a phosphor screen mounted on the opposing side of the electron gun. A diagram depicting the operation of a RHEED system is shown below in Figure 3.4.

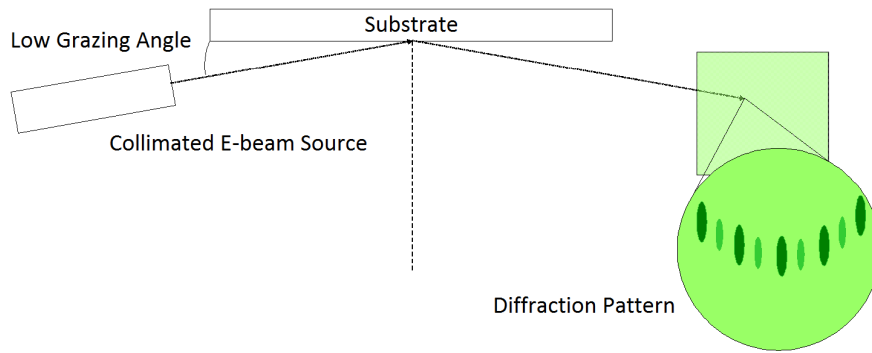


Figure 3.4: RHEED System Diagram. Diffraction pattern (periodic green rods) originates from elastic diffraction collisions. The green background haze is produced by in-elastic collisions and electron scattering within the reactor.

The diffraction pattern produced is dependent on the surface morphology of the substrate and the crystal orientation along which the beam is directed. During growth the surface does not form half unit cells but instead forms periodic structures called reconstructions to minimise surface energy. The two main reconstructions of *GaAs* which are observed in this work are the  $(2 \times 4)$  and  $c(4 \times 4)$  reconstructions.

Inelastic scattering events also occupy an important role in the formation of a RHEED pattern in addition to surface diffraction. These scattering events include phonons or plasmons within the lattice and produce a diffuse cone of electrons which are subsequently diffracted by the crystal lattice planes, depending on the beam angle. This leads to the formation of sharp lines, bands and arcs in the RHEED pattern. These are referred to as Kikuchi lines [48].

The intensity of the Kikuchi lines has several dependencies in addition to beam orientation. These include surface morphology, where steps and terraces lead to line broadening, bulk crystallinity, although due to the exit angle this only covers a range of approximately 10 unit cells, and crystal mass, where heavier materials including *Si* and silicon carbide (*SiC*) display stronger line intensity. Overall these features aid in beam alignment along a crystal azimuth and imply the possibility to monitor thin film quality based on line intensity, however, as they are not employed within this work beyond observation, they will not be discussed further.

There are multiple uses for RHEED measurements the beyond checking the reconstruction and confirming there are no growth issues. These will be discussed in the following subsections.

### 3.6.1 RHEED MEASUREMENTS FOR SUBSTRATE HEATER CALIBRATION

An MBE system may not have a pyrometer or thermocouple to measure the substrate temperature for a variety of reasons. This could be because the former is expensive and requires calibrating with surface parameters including emissivity, and the latter is difficult to get into direct contact with the substrate and therefore has limited accuracy. Or perhaps a fault occurs with the equipment during a growth campaign.

If there is a functioning RHEED system installed it is possible to use a set of calibration points to infer the relationship of substrate temperature to a heating variable (voltage, current or power) although the heater current is the most reliable option. These calibration points should be well-established conditions at which a change in temperature causes a significant change in the surface RHEED pattern. For a *GaAs* (001) surface three unique points are:

- Desorption of an amorphous As cap at  $\sim 300$  °C.
- The transition between the  $c(4\times 4)$  -  $(2\times 4)$  reconstructions at  $\sim 400$  °C.
- Oxide sublimation from the substrate surface at  $\sim 590 - 600$  °C.

When measured, these three points can be fitted with an exponential trendline to estimate the heater current required for any temperature between  $300 - 600$  °C with an accuracy of  $\pm 10$  °C. However, these calibrations are heavily based on the substrate thickness and doping as any change will affect absorption of incident radiation and therefore the surface temperature. As such, each time the substrate type or supplier is changed the calibrations must be repeated. In order to monitor any drift in heater output etc. it is also worthwhile checking these calibrations on a weekly or bi-monthly basis. The experimental procedure for this calibration will be detailed in Section 3.7

### 3.6.2 RHEED MEASUREMENTS FOR FINDING GROWTH RATES

A common use for a RHEED system in MBE is for measuring growth rates [48]. This is done by monitoring the intensity of the diffraction spots for period of time after growth has started. During growth while reconstructions are breaking and forming unit cells the surface will go through a cycle of roughening and smoothing between each monolayer, this is illustrated in Figure 3.5.

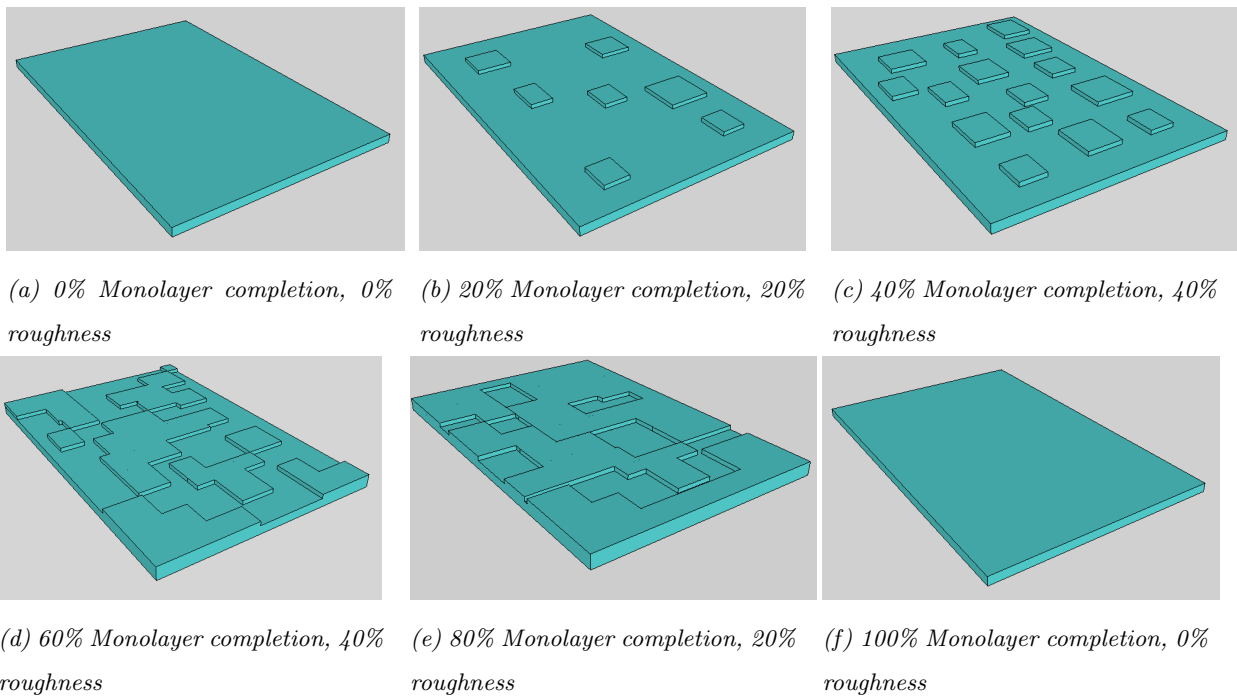


Figure 3.5: Simplified surface profile over growth of a single monolayer

This roughening and smoothing should therefore also be observable as a dimming and brightening of the RHEED pattern as the layer uniformity increases and decreases (e.g. one oscillation would represent one monolayer of growth) [49]. By recording these oscillations over a period of time, using the lattice constant of the semiconductor and finding the mean oscillations per second, the growth rate for a set of growth conditions can be calculated in-situ. These oscillations should be measured at the onset of growth due to eventual damping. For *GaAs* this involves annealing the surface under an *As* flux, setting a data logger to monitor the RHEED intensity and then opening the *Ga* shutter to recommence growth. An example of growth rate oscillation data will be shown in Section 3.8 with a description of the hardware used.

### 3.6.3 RHEED MEASUREMENTS FOR $As_2:Ga$ 1:1 CALIBRATION

Another use for a RHEED system is to calibrate the 1:1 atomic flux ratio between  $As_2$  and *Ga* which is being incorporated into the growing crystal. The 1:1  $As_2$  to *Ga* ratio measures the atomic flux of *As* required to match the deposition rate of *Ga* on the semiconductor surface and the rate of *As* desorption. It is important to this work because whilst there is a wide permissible range for high temperature *GaAs* growth, the *As* overpressure significantly affects *Bi* incorporation as discussed in Section 2.7. This has been shown by Richards *et al.* [22] and others [19], and is shown in Figure 3.6 below.

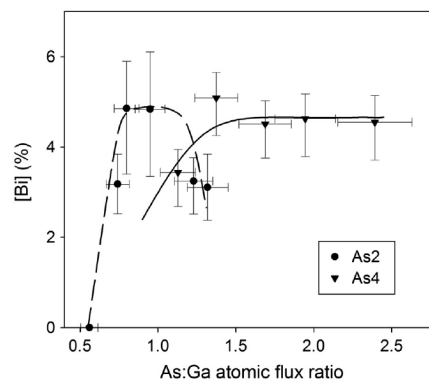


Figure 3.6: Comparison of *Bi* incorporation for various  $As_2$  and  $As_4: Ga$  atomic flux ratios. Reprinted from *Journal of Crystal Growth*, 390, R. D. Richards *et al.*, *Molecular beam epitaxy growth of GaAsBi using  $As_2$  and  $As_4$* , 120-124, Copyright (2014), with permission from Elsevier [22].

The process to find the 1:1 point consists of sequentially reducing the  $As_2$  flux and opening the *Ga* shutter for two minute intervals whilst monitoring the RHEED pattern. Researcher groups which use large amounts of *As* for III-V growth will tend to have valved cracker cells to allow for quicker flux adjustments by the positioning of a needle valve instead of changing the *As* bulk material temperature. Therefore changes to the *As* flux will be considered in terms of increasing or reducing the valve position to increase or decrease the flux, respectively. After each two minute exposure the surface should be annealed for at least thirty seconds to ensure it has settled to the same initial state and left enough time for the chamber pressure to equilibrate under the new *As* valve position.

Before the shutter is opened, the surface should have a static  $(2\times 4)$  reconstruction which forms on a  $GaAs$  buffer grown at the optimum temperature range for MBE around  $\sim 580\text{ }^\circ\text{C}$ . After the shutter is opened the surface reconstruction may change, depending on the  $As : Ga$  ratio and temperature of the substrate, to one of the reconstructions shown in Figure 3.7. If the reconstruction does not change, the  $As_2$  flux is still too high and the valve position should be reduced further.

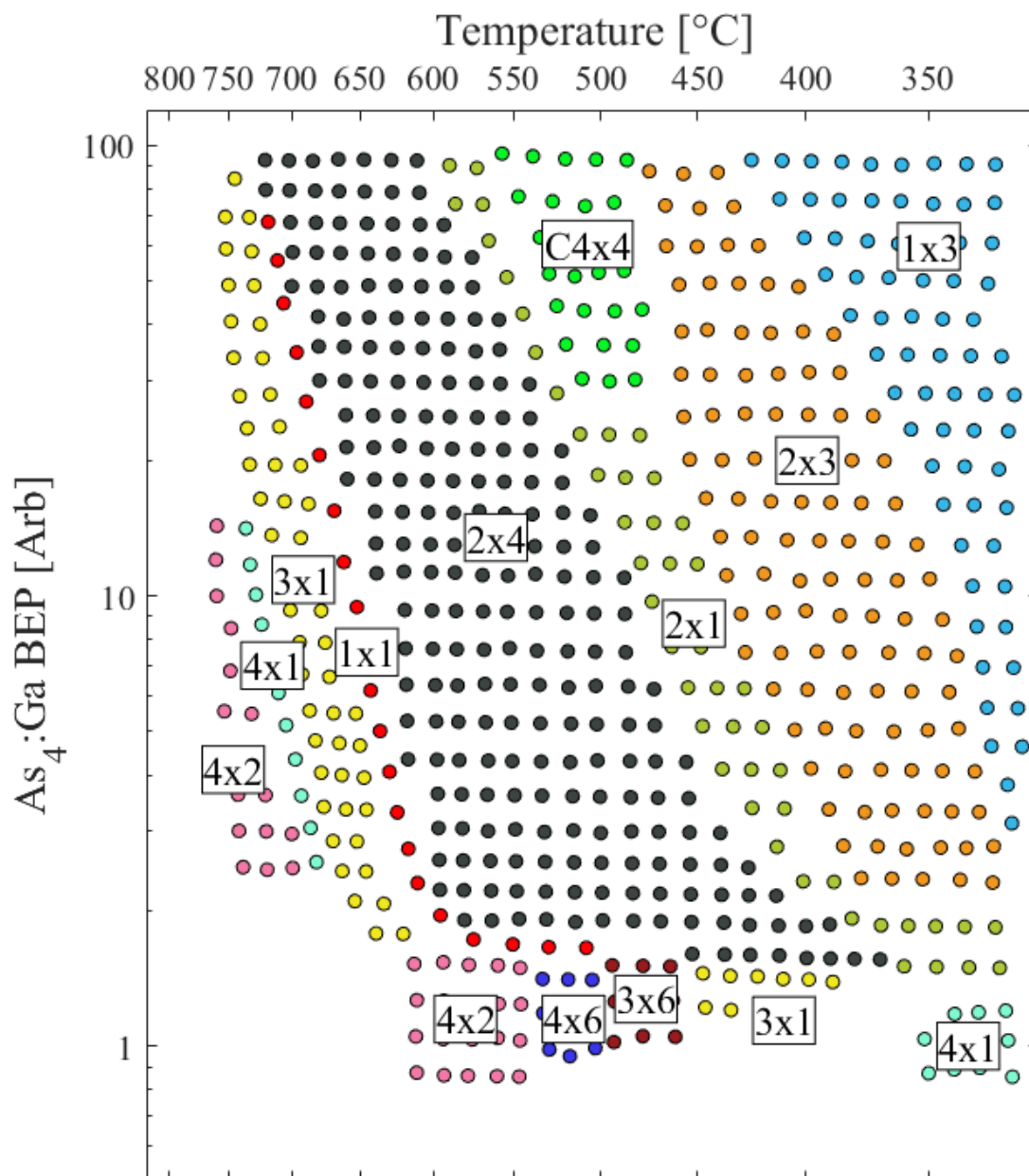


Figure 3.7: Dynamic reconstructions of  $GaAs$  during growth. Adapted from [50].

When close to the 1:1 balance it is therefore expected to see the pattern become  $(1\times 1)$  and potentially  $(4\times 2)$  or  $(4\times 6)$ . The  $(4\times 2)$  and  $(4\times 6)$  reconstructions are  $Ga$ -rich structures and indicate an oversupply of  $Ga$  relative to  $As_2$ . If this happens the valve position is gradually increased in smaller increments and the test repeated until the RHEED pattern turns  $(1\times 1)$  but does not turn  $(4\times 2)$  or  $(4\times 6)$  within the time limit. This is then referred to as the 1:1 point for  $(As_2)$ . To convert the flux value for  $As_2$  to  $As_4$  the calibration value is doubled

as  $As_4$  has a sticking coefficient of  $\sim 0.5$  [23], compared to  $\sim 1$  for  $As_2$  when growth is  $Ga$  flux limited [23, 24]. The assumption this makes is that the  $As$  cracker (which is used to thermally crack  $As_4$  into  $As_2$ ) has no effect on the total atomic flux incident on the sample.

It is important to note that the reconstruction map in Figure 3.7 is only used as a guide. This is because the  $As_4 : Ga$  ratios are quoted as beam equivalent pressures (BEPs) which are dependent on ionisation efficiencies which differ between materials and even fluctuate on identical ion gauges with age and accumulated material. The 1:1 ratio which is being calibrated is instead the atomic flux ratio.

### 3.7 HEATER CALIBRATION PROCESS

As described in Section 3.6.1 the RHEED system can be used in conjunction with a set of well-defined calibration points to calibrate the substrate heater due to the lack of a pyrometer or thermocouple on the MBE reactor used. The calibrations in this work are based on supplied current so voltage drops across the wire connections can be ignored and the heating element will receive consistent input from the power supply.

The first point which is used in calibrating the heater to a new substrate type is the native oxide desorption temperature, which occurs at  $600\text{ }^\circ\text{C}$ . Before this, the RHEED pattern will be a amorphous haze due to the oxide covering the substrate surface. As the oxide sublimates from the surface, a diffraction pattern from the semiconductor surface below will become visible. Oxide removal leaves the surface slightly roughened, however, giving the RHEED pattern 3D-features as seen below in Figure 3.8.

Before any further calibrations are performed, a buffer is needed to smooth the surface and develop a recognisable reconstruction. This buffer is  $200 - 300\text{ nm}$  thick and grown at  $580 - 590\text{ }^\circ\text{C}$  with a  $As_2 : Ga$  of  $\sim 1.6 : 1$ . Under these growth conditions the surface forms a  $(2 \times 4)$  reconstruction. An image of this reconstruction is shown in Figure 3.9.

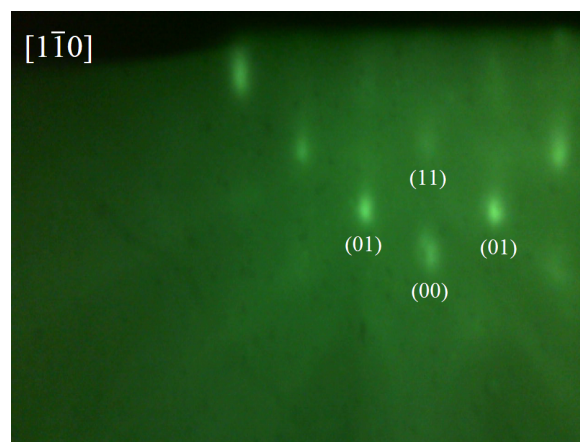


Figure 3.8: Oxide-removed ‘3D’ RHEED pattern. Image taken along the  $[1\bar{1}0]$  azimuth at  $14.5\text{ keV}$ .

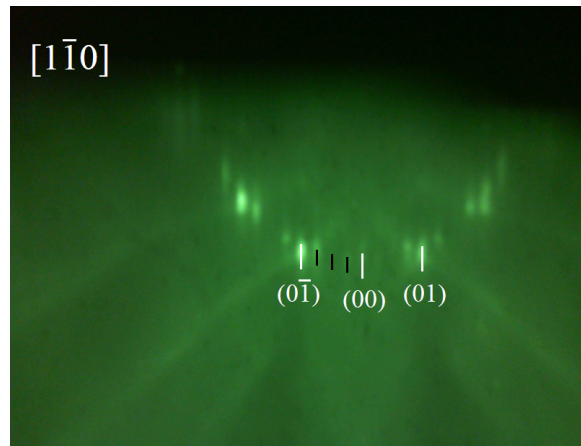


Figure 3.9:  $(2 \times 4)$  RHEED pattern. Annotations have been added to indicate the integer and fractional order diffractions. Image taken along the  $[1\bar{1}0]$  azimuth at 14.5 keV.

The next point to be measured is As cap removal which occurs at 300 °C. First an As cap is deposited on the surface of the buffer which was grown at the end of the previous step. This involves fully opening the As valve and dropping the heater current to 0 A so the As coats the sample surface in a random configuration. This amorphous As cap will scatter electrons randomly and the RHEED pattern observed will become a uniform green haze similar to before the oxide removal. The heater current is then raised from 0 A to a value around 0.55 A (depending on substrate doping) and raised in small increments every 10 min until a  $c(4 \times 4)$  RHEED pattern is observed. This is the point when the As begins to sublime from the surface, revealing the reconstruction below. Figures 3.10 and 3.11 show the RHEED pattern before and after As cap removal.

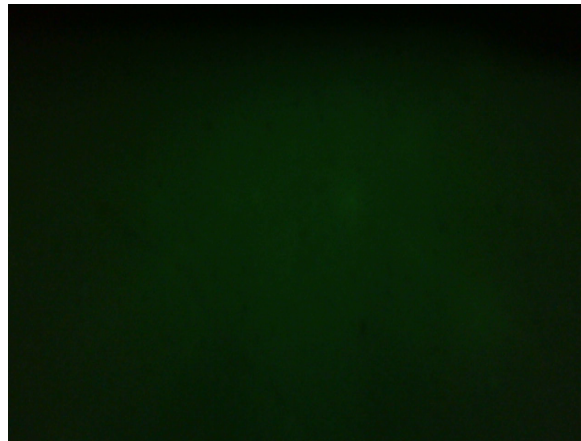


Figure 3.10: Hazy As cap. Incident electron beam is absorbed and scattered on the amorphous As surface. Due to the lack of surface order no diffraction peaks are seen. Image taken along the  $[1\bar{1}0]$  azimuth at 14.5 keV.

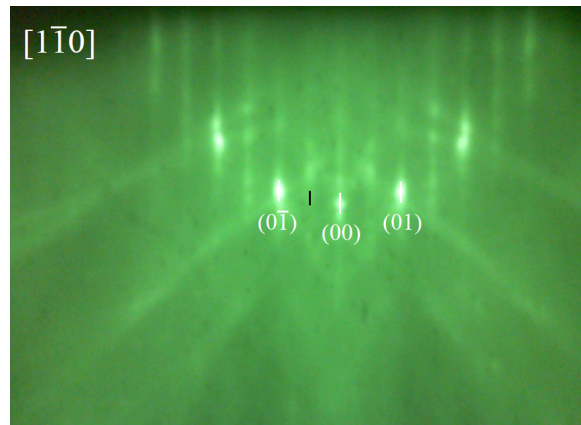


Figure 3.11:  $c(4\times 4)$  Reconstruction after As cap removal. Annotations have been added to indicate the integer and fractional order diffractions. Image taken along the  $[1\bar{1}0]$  azimuth at 14.5 keV.

The final calibration point used is the  $c(4\times 4)$  -  $(2\times 4)$  transition which, with no external As flux, occurs at 400 °C. As with all the other steps the heater current is increased from a point below the expected transition current in 10 min steps. This is done in the absence of an As flux as this would change the temperature at which the transition occurs. As there will be As sublimation from the surface at this temperature, however, it is important to only leave the substrate at each current setting for enough time to check for a change. If left too long the surface would become Ga-rich and could nucleate Ga droplets, irreparably damaging the surface.

When all the points have been found the heater currents and characteristic temperatures are plotted with an exponential trend-line as in Figure 3.12.

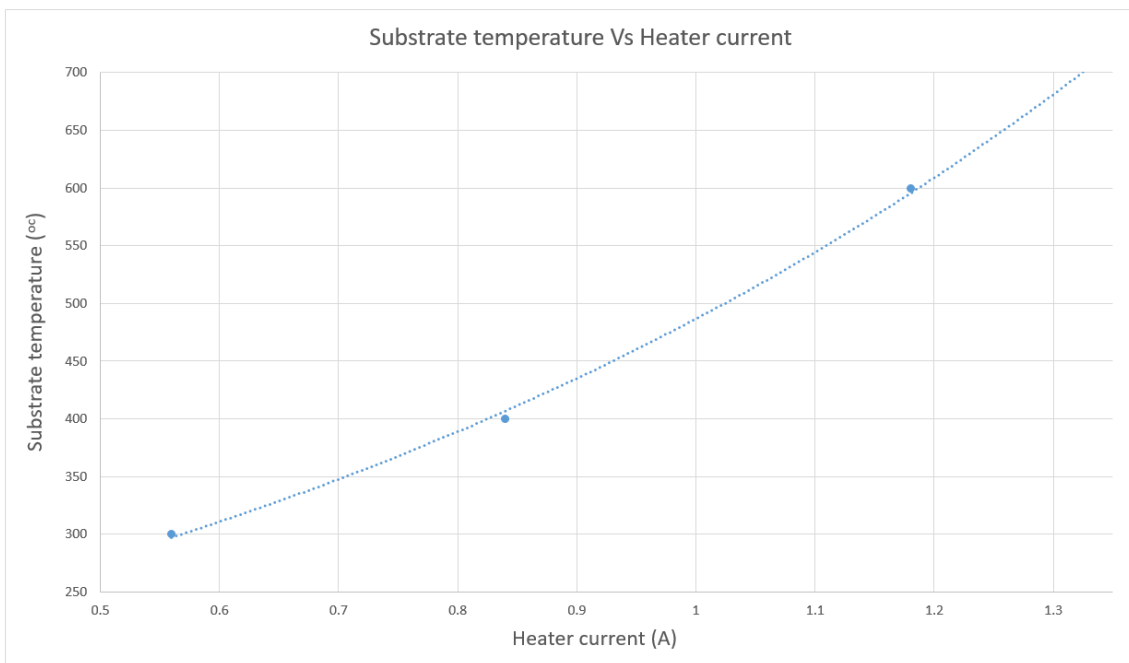


Figure 3.12: Plot of heater calibration points with exponential trend-line.

Using this trend-line an arbitrary point can be mapped onto the curve to estimate the required current for any temperature within the range. These calibrations are done for each substrate type used and checked on a weekly basis to ensure they are still accurate. In order to ensure samples are fully oxide-removed when running fully automated recipes a temperature  $\sim 20\text{ }^\circ\text{C}$  higher than necessary is used.

### 3.8 GROWTH RATE CALIBRATION

As discussed in Section 3.6.2 RHEED measurements can also be used for growth rate calibration. This is impractical to do by eye and instead is performed using a web cam mounted in front of the phosphor screen and image analysis software running in MATLAB. A live feed of the RHEED screen is opened within the software and rectangles drawn over points of interest which the software should measure. The *Ga* shutter is opened, recommencing growth on the surface and causing the intensity of the diffraction pattern to oscillate as monolayers are completed. The average brightness of these areas is plotted with respect to time giving the waveforms shown in Figure 3.13a.

The oscillations in intensity starting after the *Ga* shutter is opened at 7 s are easy for the human eye to recognise, but peak finding algorithms would be confused by the noise present. To remove this the data is passed through a moving average filter until it looks like the waveforms in Figure 3.13b. Now the noise in the data has been removed, the range for which the data appears representative is selected. The software then identifies the number of oscillations within the range and the duration over which they occur and finally outputs a calculated growth rate in monolayers per second ( $MLs^{-1}$ ). This can be converted into micrometers per hour ( $umh^{-1}$ ) by using Equation 3.2 where 'a' is the lattice parameter of the material in meters. As the conversion for *GaAs* comes out with  $1\text{ }MLs^{-1} = 1.018\text{ }umh^{-1}$  the two are assumed to be equivalent.

$$GR(um/h) = \frac{GR(ML/s) \times a \times 10^6 \times 3600}{2} \quad (3.2)$$

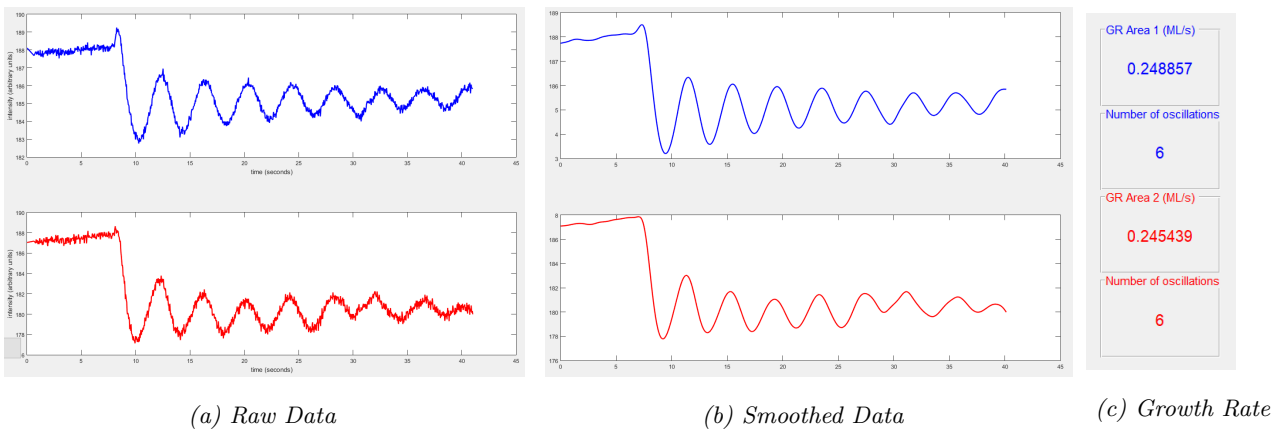


Figure 3.13: Growth Rate Measurements

## 4 MATERIAL CHARACTERISATION

### 4.1 PHOTO-LUMINESCENCE

Photo-luminescence (PL) is a characterisation technique based on photo-excitation of carriers (absorption of a photon to excite an electron-hole, e-h, pair) and radiative recombination of carriers (an electron recombining with a hole by emitting excess energy as a photon). It can be used to assess the optical quality and band gap of a semiconductor. This technique is useful as it doesn't require processing of the layer and can therefore be performed immediately after removal from the growth chamber. Figure 4.1 shows the three basic stages to PL. First an incoming photon with energy,  $E$ , greater than the layer band gap,  $E_g$ , is absorbed and promotes an electron to a state in the conduction band, leaving a hole in the valence band. The electron then 'thermalises' down to the band edge. Finally, the electron and hole recombine, releasing the energy difference in the form of a longer wavelength photon.

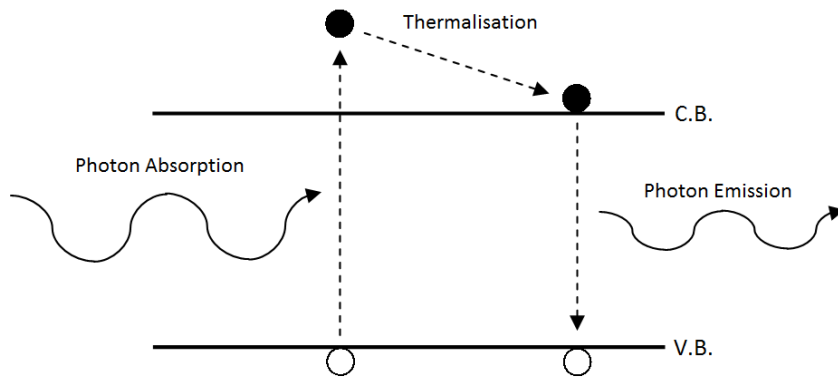


Figure 4.1: Photo-luminescence stages.

Equation 4.1 shows the simple relationship between the wavelength and energy of a photon, where  $h$  is Planck's constant ( $J s^{-1}$ ),  $c$  is the speed of light in a vacuum ( $m s^{-1}$ ) and  $\lambda$  is the wavelength of the photon ( $m$ ). Using this, the peak PL wavelength can be used to calculate the band gap of a bulk sample and estimate the *Bi* content. With quantum confined layers the process is more complicated, as the emission energy is also affected by the level of confinement determined by quantum well layer thickness and barrier height.

$$E(J) = \frac{h \times c}{\lambda} \quad (4.1)$$

The setup used for photo-luminescence characterisation in this work is one of the most important. It consists of several pieces of equipment:

1. A 532 nm diode-pumped laser to stimulate the semiconductor layer and excite carriers.
2. An optical chopper to modulate the laser intensity.
3. An adjustable stage to align samples and optimise the output signal.
4. A Cassegrain telescopic F-matching lens to collect and focus light onto the monochromator entrance slits.

5. A Triax 550 monochromator to filter the input light.
6. An  $LN_2$  cooled  $Ge$  detector to convert the modulated optical signal into an electrical signal.
7. A lock-in amplifier to accurately extract the modulated electrical signal from background noise.

The layout of these is shown in Figure 4.2. The reason for cooling the detector is to reduce dark currents and increase the signal-to-noise ration during operation. This is done by filling a reservoir within the detector with liquid nitrogen ( $LN_2$ ) 30 *min* before use to start the initial cooling process. When most of the nitrogen has boiled-off the reservoir is topped up to ensure it stays at a constant low temperature for the duration of testing.

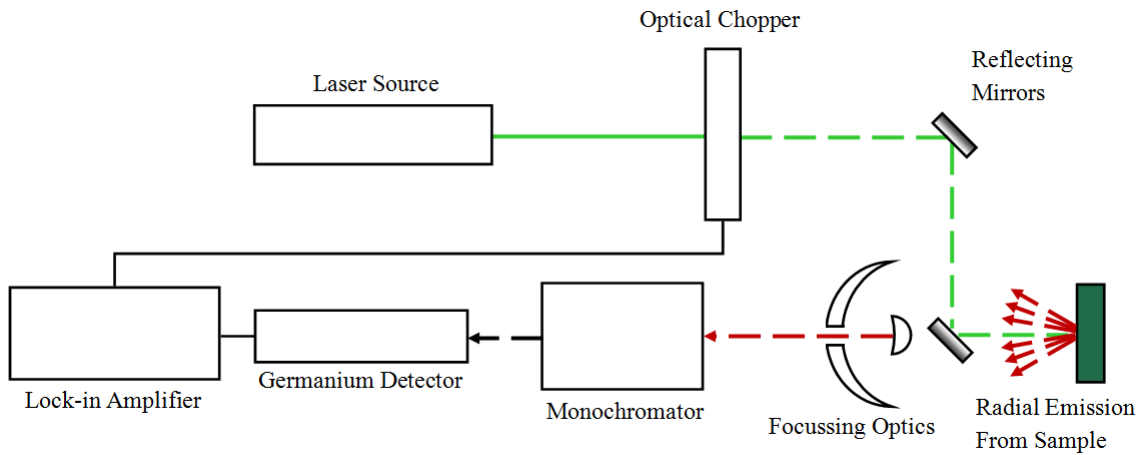


Figure 4.2: Practical layout of the PL setup.

This setup also has a closed-loop helium cryostat system which can take layers down as far as  $\sim 15 K$  for low temperature (LT) PL measurements. This is useful as it improves emission in poorly radiative layers which have a large number of defects. The reduction in ambient thermal energy allows features of the semiconductor bands to be more clearly identified.

#### 4.1.1 THE VARSHNI RELATION

In 1967, Y. P. Varshni presented an equation to fit the change in peak PL energy as a function of semiconductor crystal temperature [51]. This equation was validated for multiple semiconductors including  $Si$ ,  $GaAs$ ,  $InAs$  and  $InP$ . It is shown below in Eq 4.2 along with an example of this temperature dependence in Figure 4.3.

$$E_g = E_0 - \alpha T^2 / (T + \beta) \quad (4.2)$$

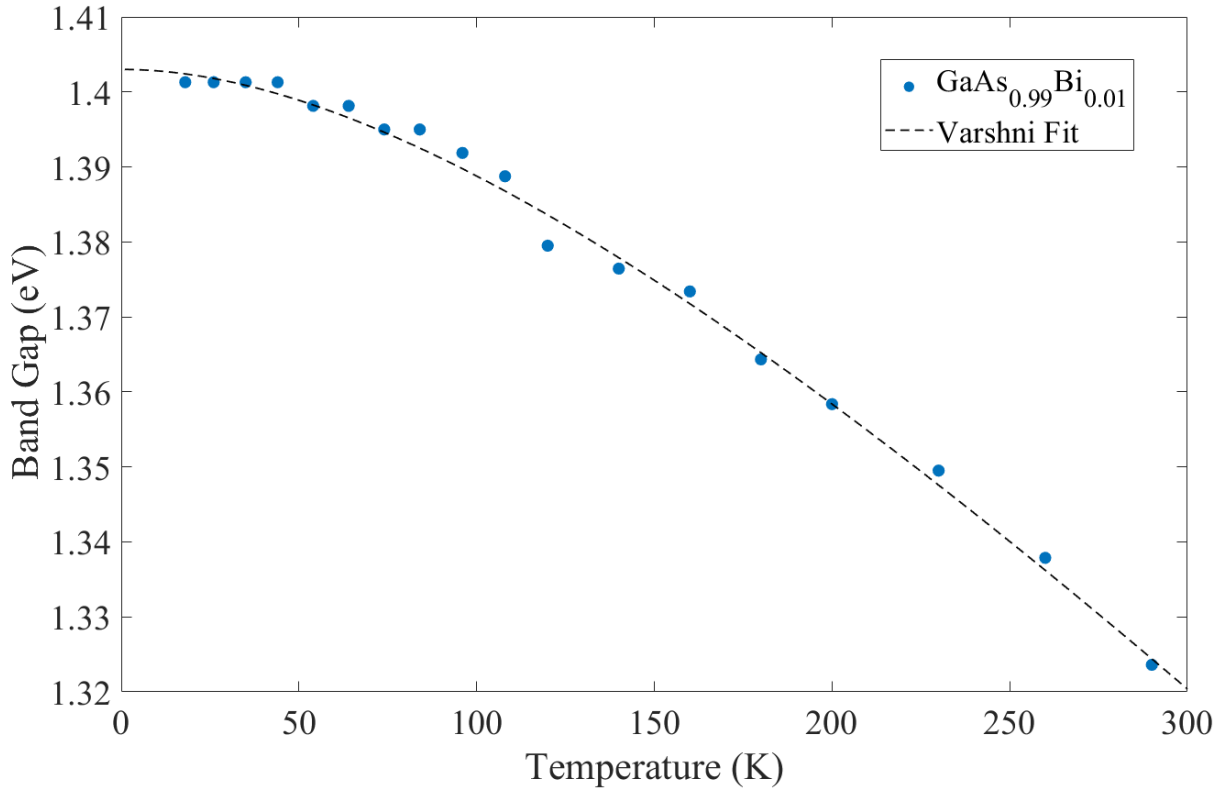


Figure 4.3: Temperature dependence of the band gap of a GaAsBi layer with  $\sim 1\%$  Bi (circles) and fitted using the Varshni equation (dashed line). Fit parameters are  $E_0 = 1.403$ ,  $\alpha = 5.184e - 4$  and  $\beta = 264.7$ . Data measured in Part II results section on layer STG38.

The significance of this plot is that it indicates how much a semiconductor’s band gap and therefore its emission energy depends on temperature. This is an important characteristic to analyse in applications where precise control of emission wavelength is critical, for example in telecoms as discussed in Section 2.7.3.

## 4.2 X-RAY DIFFRACTION

### 4.2.1 DIFFRACTION THEORY

X-ray diffraction (XRD) is a powerful crystallographic technique which allows the non-destructive study on the structural properties of semiconductor layers. X-rays undergo strong diffraction when they pass through planes of ordered atoms within the semiconductor lattice, this is due to the interatomic spacing being on the length scale as the photon wavelength. This diffraction results in intense peaks when the incident angle of the X-rays satisfies Bragg’s law, which is the condition for constructive interference. This is shown in Equation 4.3 and Figure 4.4. It states that for two coherent waves to interfere constructively the path difference between them must be an integer number of wavelengths [52].

$$n\lambda = 2d\sin(\theta) \tag{4.3}$$

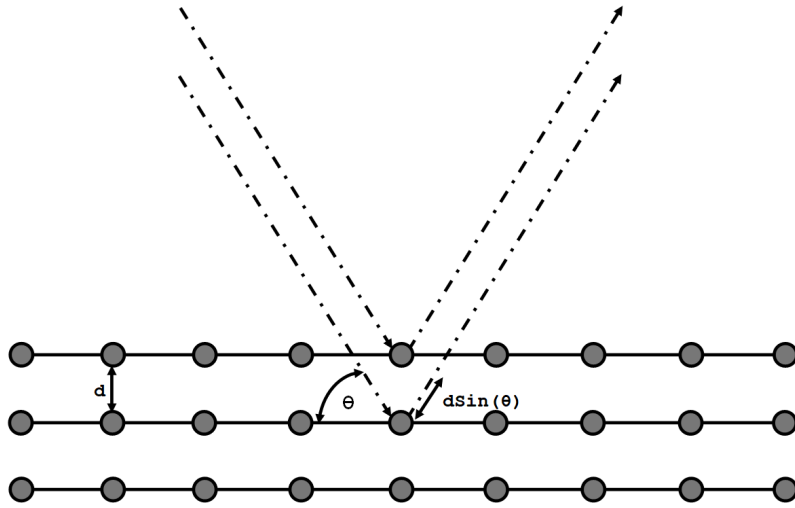


Figure 4.4: Bragg's law for constructive interference of diffracted waves.

The definition of Bragg's law shown in Figure 4.4 is a 2D representation. In reality this diffraction occurs in three dimensions and is better described by the Ewald sphere. This is demonstrated in Figure 4.5 in reciprocal space.

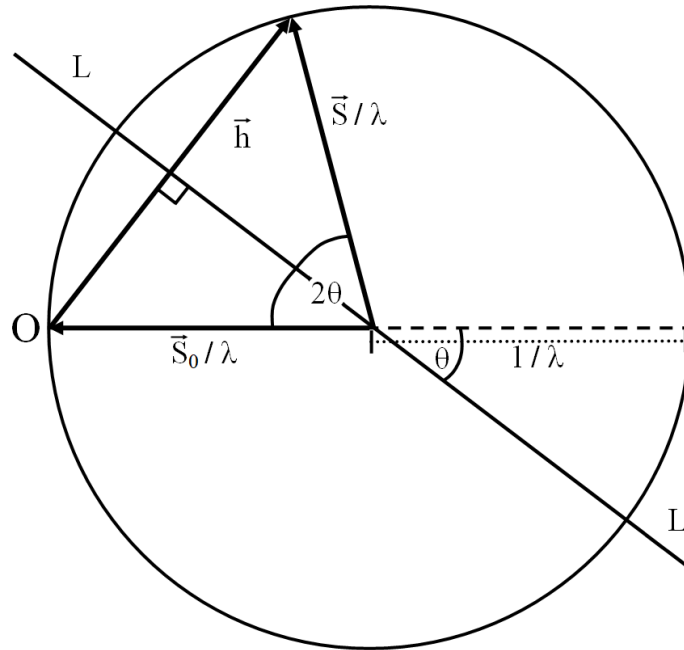


Figure 4.5: The Ewald sphere.

For an X-ray with wavelength  $\lambda$ , it will have a length of  $\frac{1}{\lambda}$  in reciprocal space with an arbitrary vector of  $\vec{S}_0$ . For diffraction to occur between this incident ray and a lattice plane,  $L$ , with normal vector  $\vec{h}$ , then the following condition must be met:  $\vec{h} = \frac{\vec{S} - \vec{S}_0}{\lambda}$  [53].

To test this condition, we can examine the geometry illustrated by the three vectors in Figure 4.5. By splitting

the isosceles triangle they enclose into two right-angled triangles, the following relation can be defined:

$$\frac{\frac{|h|}{2}}{\frac{1}{\lambda}} = \sin(\theta) \quad (4.4)$$

Multiplying through by 2 and  $\lambda$  gives the form:

$$|h|\lambda = 2\sin(\theta) \quad (4.5)$$

Now if we substitute the real space definition of  $|h|$  which is  $\frac{1}{d}$  where  $d$  is the inter-planar spacing:

$$\frac{\lambda}{d} = 2\sin(\theta) \quad (4.6)$$

This can then be simplified to final form shown below in Equation 4.7 which is identical to that given for Bragg's law in Equation 4.3:

$$\lambda = 2d\sin(\theta) \quad (4.7)$$

From these equations, and remembering that  $\sin(\theta) \leq 1$ , we can also understand that number of reflections accessible while satisfying the conditions of the Ewald sphere is limited by the condition that  $|h| \leq \frac{2}{\lambda}$ . This results in a sphere of accessible reflections with radius  $\frac{2}{\lambda}$  which is referred to as the limiting sphere. This is shown in Figure 4.6. There are other factors which further limit the range of accessible reflections within this sphere, however, these are not relevant to this work and will not be discussed further.

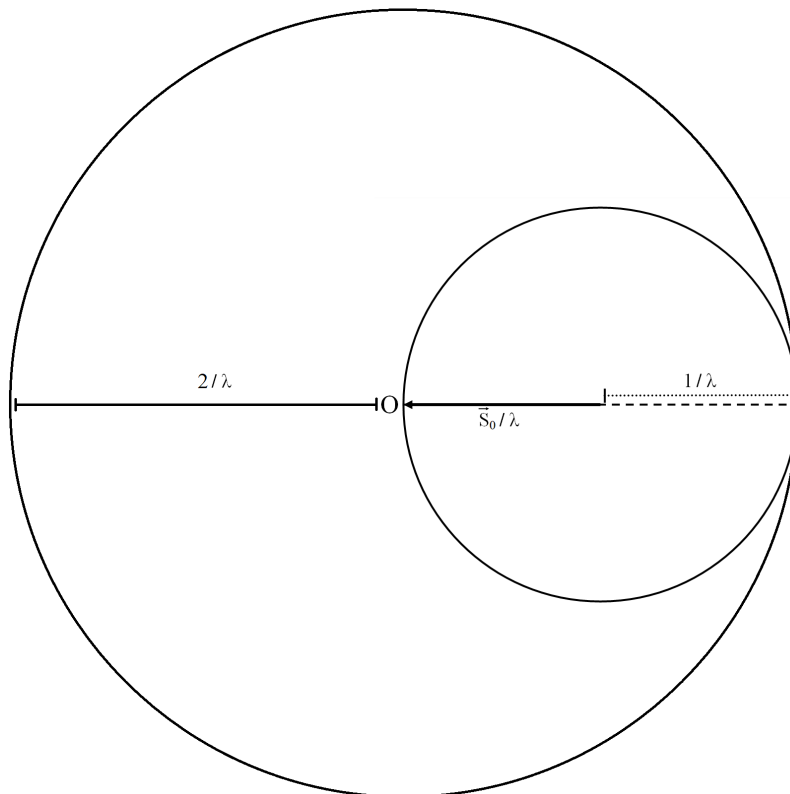


Figure 4.6: The limiting sphere of accessible reflections [53].

During an actual XRD scan, a semiconductor layer is mounted on a motorised stage capable of panning and rotational movements in three dimensions. This allows it to be orientated in the path of an X-ray source such that the diffraction conditions for a given accessible reflection are met. The layer can then be rotated in various styles for different scan types while a detector, which is also mounted on a rotational stage to allow motion relative to the target layer, records the intensity of the diffracted X-ray beam.

The XRD system which was used in this work is a commercial Bruker D8 Diffractometer which has a *Cu* target producing *CuK $\alpha$ <sub>2</sub>* radiation with a wavelength of 154.06 pm. Fitting of the recorded XRD data was done in Bede RADS Mercury software. The types of scans used are discussed in the following subsections.

#### 4.2.2 SYMMETRIC AND ASYMMETRIC SCANS

The primary scan used in this work is a symmetric *GaAs* (004) scan which has a Bragg angle of  $\sim 33.01^\circ$ . An illustration of this scan is shown in Figure 4.7. The definition of symmetric comes from the condition that  $\omega = \theta$  so for an increase in  $\omega$  of  $0.02^\circ$  there will be an increase of  $2\theta$  of  $0.04^\circ$ .

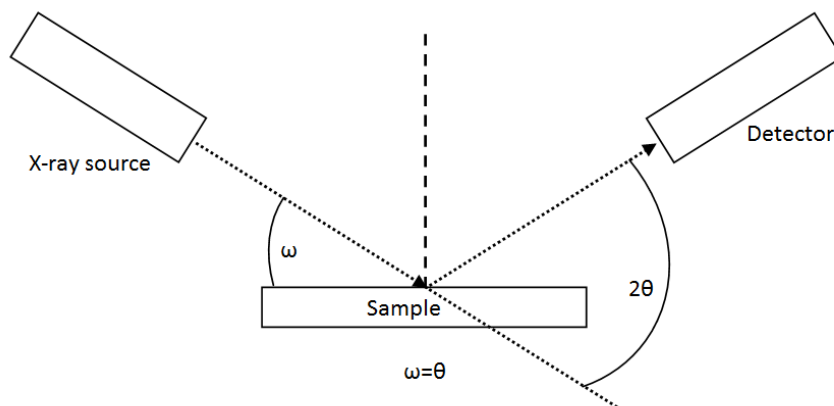


*Figure 4.7:  $\omega - 2\theta$  symmetric diffraction scan.  $\omega$  and  $2\theta$  are stepped simultaneously to maintain  $\omega = \theta$ . This scan is useful in determining composition in hetero-epitaxial layers.*

One of the purposes of this scan is that it can be used to identify the composition and quality of grown material on a *GaAs* substrate. The system is first optimised around the substrate Bragg angle as this will give the strongest diffraction due to its thickness. The reason for this is whilst the Bragg angle for *GaAs* (004) should be  $\sim 33.01^\circ$ , this is unlikely to be the angle measured due to slight stage and substrate offsets. Therefore this is manually calibrated for before starting the scan.

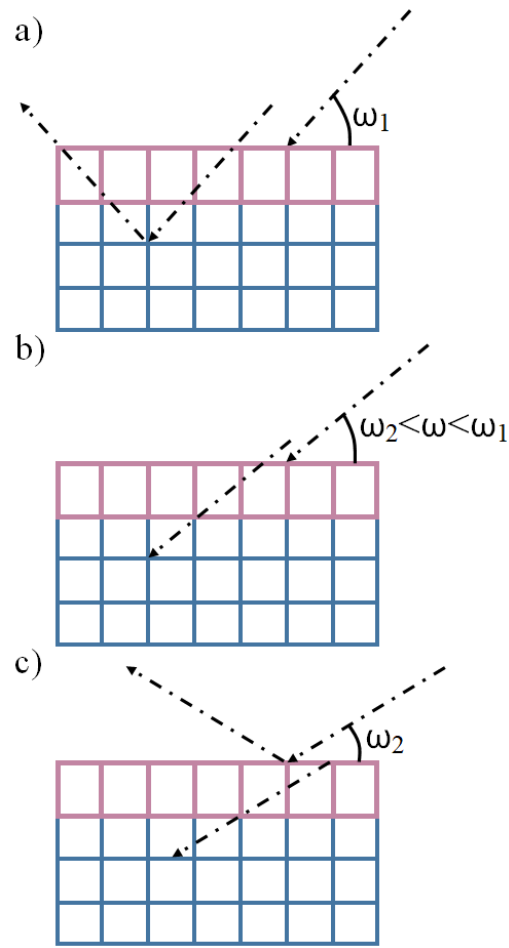


Figure 4.8: Illustration of symmetric  $\omega - 2\theta$  scan on an example epilayer. The epilayer has a larger lattice constant than the substrate and is compressively strained. a)  $\omega$  is set to the Bragg condition for the substrate (blue),  $\omega_1$  and the diffracted X-rays are detected at  $2\theta$ . b)  $\omega$  is reduced while maintaining  $\omega = \theta$  and there are no diffracted X-rays. c)  $\omega$  is coincident with the Bragg condition for the strained layers (pink),  $\omega_2$ , and diffracted X-rays are once again detected. This is only a simplified depiction of this scan as interference between diffraction between the different layers also occurs.

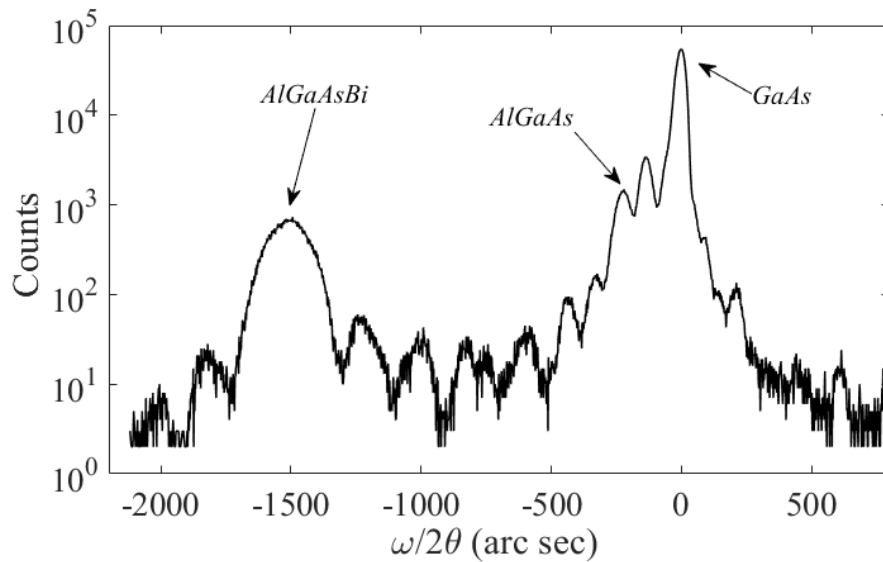


Figure 4.9: Example  $\omega - 2\theta$  scan on layer STL49 which is presented in Part IV. The peaks of the different materials in the structure are labelled. Due to its close proximity to the GaAs substrate peak, the AlGaAs peak is not distinct.

Another scan which is used in this work is an asymmetric  $\omega$ -scan which will be referred to as a rocking curve. This is illustrated in Figure 4.10. In this scan  $2\theta$  is fixed at the Bragg angle for the target reflection whilst the substrate is rotated ( $\omega$ ). This scan is sensitive to only the lattice spacing which  $2\theta$  is set to, therefore, its intensity with respect to  $\omega$  will indicate the level of wafer curvature and miss-orientation for the planes with that spacing. A comparison for an ideal and defected lattice is shown in Figure 4.11.

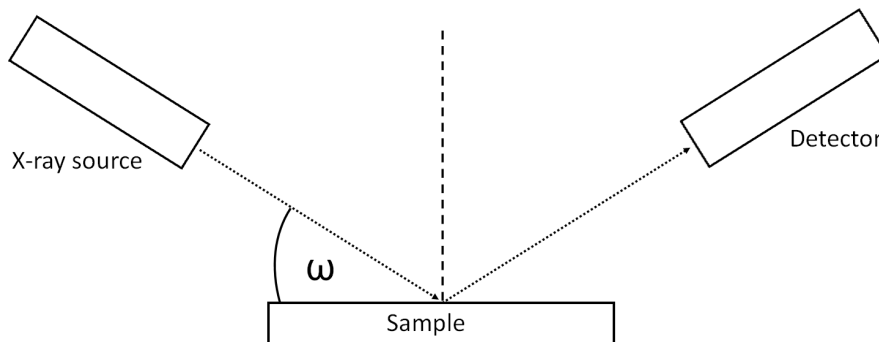


Figure 4.10: Asymmetric  $\omega$ -scan, sometimes referred to as a rocking curve.  $\omega$  is swept around the Bragg angle for an epilayer. The detector is fixed at the  $2\theta$  angle for the Bragg condition. This scan is useful in assessing the level of miss-orientation and curvature in a particular semiconductor layer or plane spacing.

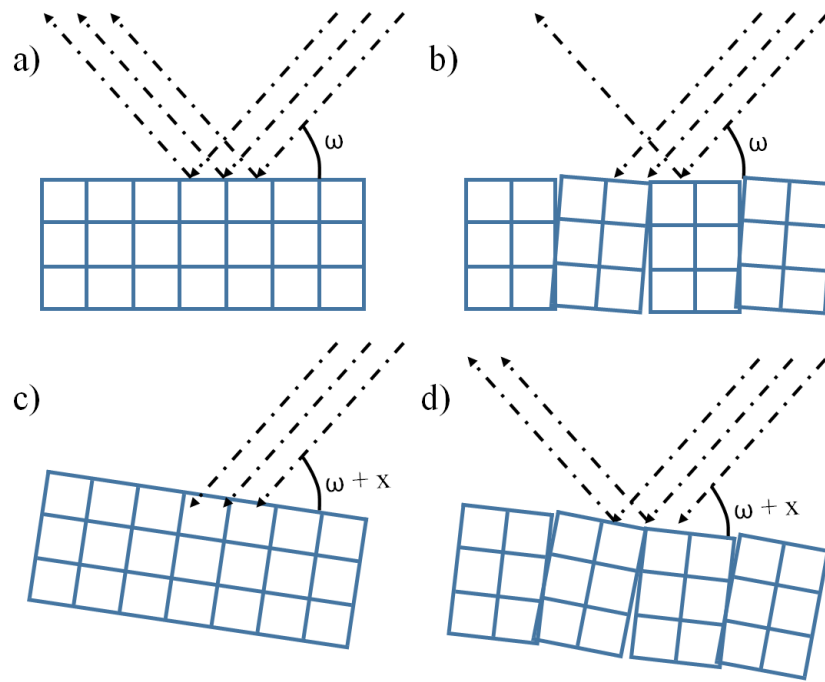


Figure 4.11: Illustration of asymmetric  $\omega$ -scans on a perfect crystal and a crystal with defects. At the Bragg condition for the a) perfect crystal and b) defected crystal there will be some intensity for diffracted X-rays, indicated by the reflected beams. At a different  $\omega$  angle there would be no diffraction from c) the perfect crystal, but for d) the defected crystal, miss-orientated cells can be brought into Bragg alignment and give a non-zero diffraction intensity.

#### 4.2.3 RECIPROCAL SPACE MAPPING

When growing hetero-epitaxial semiconductor structures there will always be some level of strain due to lattice mismatch between the two materials, as seen in Figure 2.3 which displayed common semiconductor band gaps and lattice constants. However, when the build up of strain within a layer passes a critical threshold the epilayer will begin to relax in order to reduce the strain energy. This results in line dislocations where the strained layer relaxes, either ‘pushing out’ or ‘pulling in’ and leaving dangling bonds. A cartoon comparison between a strained and relaxed epilayer is shown in Figure 4.12 for tensile and compressive strain, respectively.

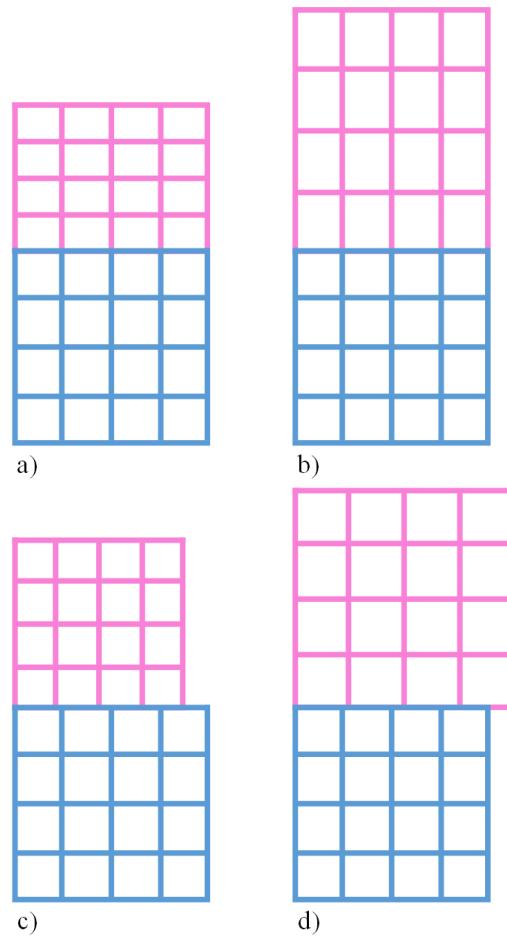


Figure 4.12: Diagram showing a) tensile and b) compressive strained layers and equivalent relaxed layers, c) and d) respectively. Tensile strain leads to a decrease in out-of-plane height and compressive strain leads to an increase in out-of-plane height.

Whilst this can be partially seen and modelled in a symmetric XRD scan, a more thorough way to investigate the amount of strain and relaxation in a structure is to take a reciprocal space map (RSM). At a low level these are a series of stacked 2D scans to build a 3D image, a higher level description of an RSM is that it is a 2D snapshot of the reciprocal space shown of the semiconductor lattice. These scans are particularly useful in complex device structures where there are multiple semiconductor layers or broad peaks which make modelling difficult.

An example RSM of an epilayer is shown in Figure 4.13. This depicts an  $AlGaAsBi$  structure which was grown for the work discussed in Part IV.

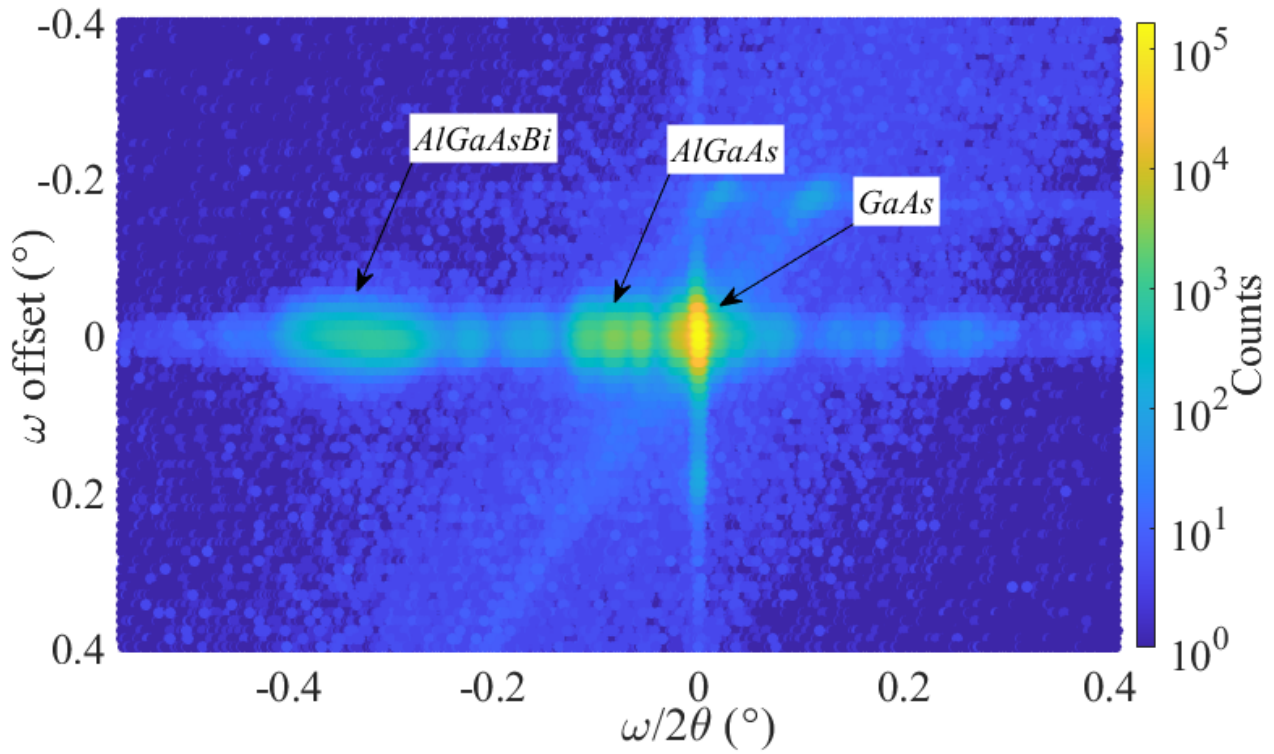


Figure 4.13: RSM of an epilayer containing AlGaAs and AlGaAsBi grown on a GaAs substrate. The diffraction peaks for each material are visible with Pendellösung fringes superimposed.

### 4.3 NOMARSKI MICROSCOPY

A Nomarski microscope is a surface imaging device which can also be referred to as a reflectance differential interference contrast system (DIC) [54]. It was first proposed by Georges Nomarski in 1952 and can be used to image changes in thickness and refractive index across surfaces [55].

As the image intensity modulation is a result of changes in both refractive index and thickness it can be difficult to determine which is changing across a sample. As the materials in this work are semiconductor layers which are nominally flat (to a few *nm*), and should have uniform refractive index from ideal epitaxial growth across the surface, any disruption to a smooth surface image can be interpreted as a defect developed during growth either due to impurities or particulates.

Example Nomarski images of *GaAs* samples are shown in Figure 4.14. Images 4.14a and 4.14b display good epitaxial quality with minimal surface defects. Images 4.14c and 4.14d on the other hand show a rough surface which was produced due to a large increase in *Ga* flux during growth. The oversupply of *Ga* led to droplet formation after which growth continued in a vapour-liquid-solid process where the supplied molecular flux is adsorbed into the droplets and until the droplet reaches saturation and the material is deposited at its base, leading to the volcano-like structures seen in 4.14d.

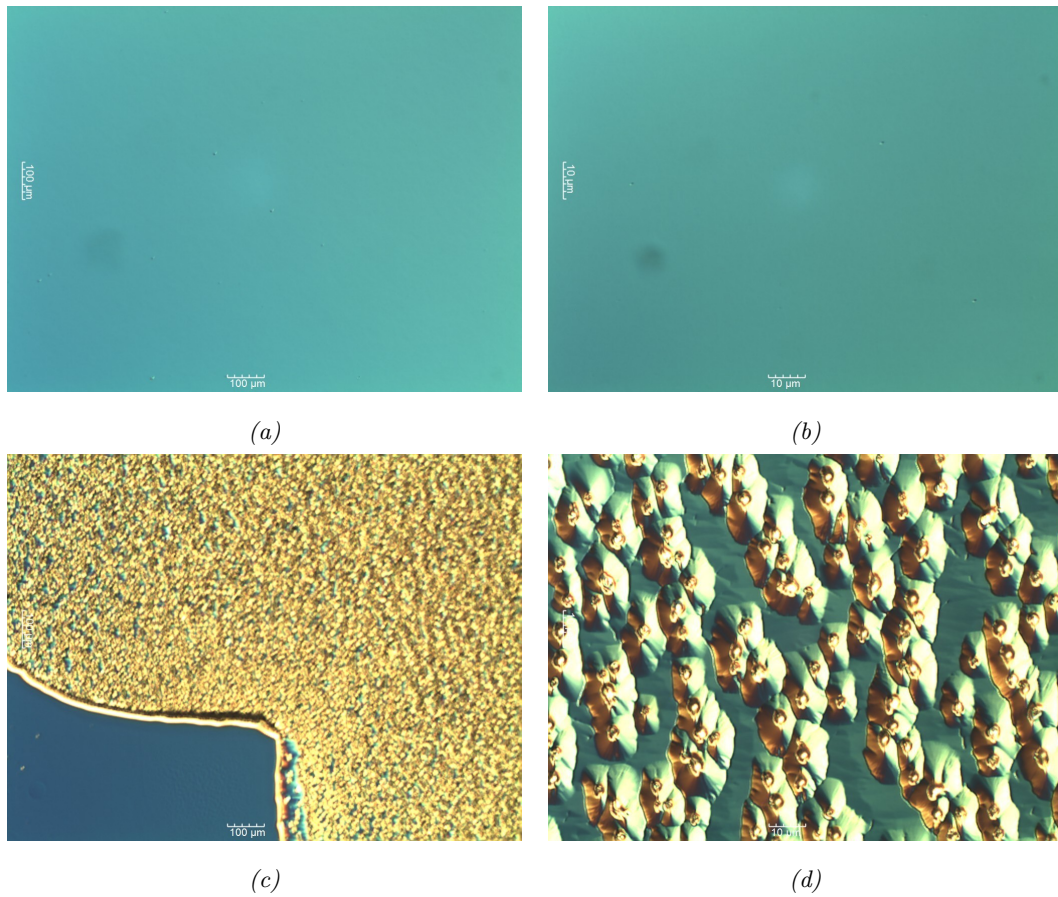


Figure 4.14: Nomarski images of good and bad surfaces. (a) and (b): An un-doped test structure at 5× and 50× magnification respectively. (c) and (d): A poor surface caused by over supply of Ga leading to droplet formation and faceting, at 5× and 50× respectively.

#### 4.4 RUTHERFORD BACKSCATTERING SPECTROSCOPY

Rutherford Back-scattering Spectroscopy (RBS) is an ion beam characterisation technique which provides elemental and thickness sensitive information about semiconductor layers. Ionised helium ( $He$ ) nuclei are focussed into a collimated beam and accelerated to  $MeV$  energies which are directed at a layer [56].

These  $He$  ions are scattered through Coulombic interaction according to classical physics as the de Broglie wavelength of the particles is much smaller than the scattering centres. To demonstrate this, the de Broglie wavelength of a 2  $MeV$   $He$  nucleus is calculated below where  $h = 6.626 \times 10^{-34} J \cdot s$ ,  $M = 4.167 \times 10^{-27} kg$ .

$$\begin{aligned}
 v &= \left[ \frac{2 \times E}{M} \right]^{1/2} \\
 &= 9.79 \times 10^6 m \cdot s^{-1} \\
 \lambda &= \frac{h}{M \times v} \\
 &= 1.01 \times 10^{-4} \text{ \AA}
 \end{aligned}$$

Here we see that the de Broglie wavelength of a  $He$  ion at 2  $MeV$  is  $1.01 \times 10^{-4} \text{ \AA}$ , which is much smaller than the inter-atomic spacing seen in semiconductors of several angstroms.

Figure 4.15 depicts the scattered trajectories of a directed *He* ion beam on a target atom. At direct incidences the ion is backscattered, but as the offset between the ion and target is increased ions are deflected and continue deeper into the layer. The deflection angle is initially large, reducing until distant ions are unaffected. The void left behind the target atom where ions do not travel is referred to as the shadow cone.

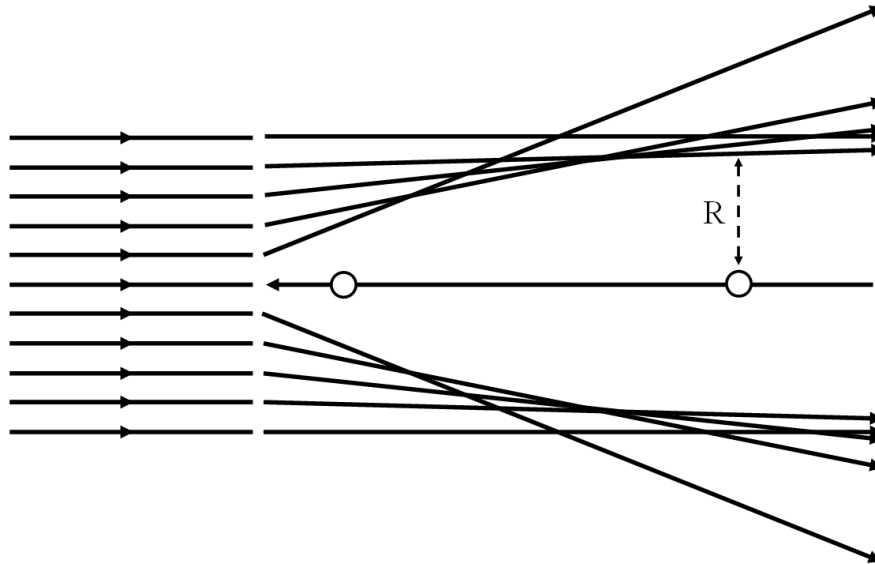


Figure 4.15: Scattering trajectories of *He* ions from a target atom. The shadow cone is defined by the area following the initial target atom in which there ions do not travel.

Given the conservation of energy and momentum in these collisions, the energy and velocity of the scattered *He* ions contain information characteristic of the target atom. Solving the relevant conservation requirements gives the following equation:

$$K = \frac{E_1}{E_0} = \left[ \frac{(M_2^2 - M_1^2 \sin^2 \theta)^{1/2} + M_1 \cos \theta}{M_1 + M_2} \right]^2 \quad (4.8)$$

This yields the kinematic factor where  $E_0$  and  $E_1$  are the incident and scattered ion energies,  $M_1$  and  $M_2$  are the masses of the ion and target atom, respectively and  $\theta$  is the scattering angle.

As the *He* ions travel through the crystal they also continuously lose energy through electron interactions, known as electron stopping [57]. This loss is dependent on both ion energy and target material but can be modelled and is used in calculating the depth profile of a semiconductor layer [56].

For semiconductors there are two general geometries which can be used in RBS characterisation. There first is ‘channelled’. In this configuration the ion beam is directed along one of the crystallographic orientations. Due to the high level of crystal order and the formation of the shadow cone as shown in Figure 4.15; after initial scattering off surface atoms most of the ions travel unimpeded through the interatomic crystal channels, hence the term ‘channelling’. This geometry can therefore be used to measure the crystallinity of a layer as a poor quality layer, with a high density of interstitial atoms, will produce a larger ion count than a purer and more

ordered crystal. There is a limit to the depth for this analysis, however, as ion de-channelling does occur deep in the layer due to successive ion deflections eroding the channelling condition.

The other main RBS geometry is called ‘random alignment’, or ‘blocking’. Here the ion beam is aligned to the layer in order to minimise the symmetry of the viewed crystal and maximise ion scattering. This produces conditions for ions to scatter equally of all target atoms within the layer regardless of whether they occupy crystal lattice sites. From this data the atomic composition of material can be modelled to give a composition and depth profile for a layer.

Following from the use of channelled RBS to characterise the crystallinity of a layer, by combining channelled and random alignment scans, the substitutional percentage of each element can be found. The theory of this is that the channelled data should mostly contain information about interstitial species whereas the random alignment data holds information about all present atoms. This is calculated using Equation 4.9, shown below. However, due to the de-channelling effect mentioned above the accuracy of this measurement decreases with depth.

$$Substitutional\ Percentage\ (E) = \left[ 1 - \left( \frac{Ion\ Yield\ \{Channelled\}}{Ion\ Yield\ \{Random\ alignment\}} \right) \right] \times 100 \quad (4.9)$$

#### 4.5 ATOMIC FORCE MICROSCOPY

Atomic force microscopy (AFM) is a surface imaging technique which can produce nanoscale topographical maps of material surfaces. The application of this technique in the field of semiconductor growth has included analysing the surface roughness of epitaxial layers and in observing the morphology and density of surface QDs.

AFM differs from Nomarski microscopy in that it acquires 3-dimensional surface information by physical interaction with the sample via a sharp probe tip suspended on a cantilever. Using piezoelectric transducers this tip is accurately moved across the sample surface whilst recording the surface height [58]. A basic diagram of an AFM system is shown in Figure 4.16.

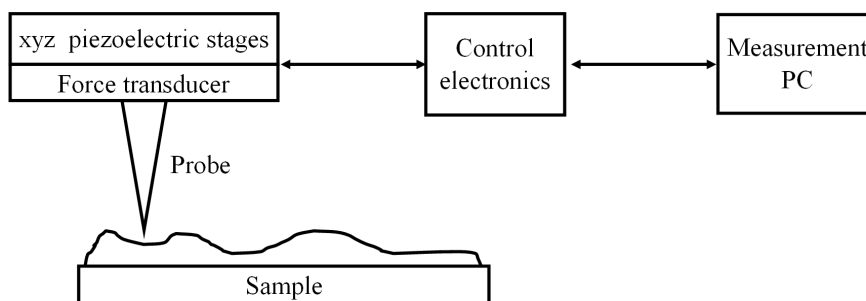


Figure 4.16: Simplified diagram of AFM operation. The sharp probe tip is moved across the sample surface by the xyz piezoelectric transducers whilst the force transducer measures the interaction between the sample and probe tip. The control electronics facilitate this and return topographical data back to the measurement PC.

There are a variety of measurement modes which can be used in AFM. For semiconductor surfaces non-contact, sometimes also known as tapping mode or near-contact, is generally used as the force applied to the surface is reduced which can prevent surface damage [58].

A limiting feature of AFM characterisation is the effect of tip convolution. As the probe tips are susceptible to damage or blunting and are not infinitesimally thin. Deconvolution of tip effects is difficult due to the requirement of having to image the tip itself, however, if the surface features to be imaged are sufficiently large relative to the size of the tip, the impact of tip convolution is limited. This is illustrated in Figure 4.17.

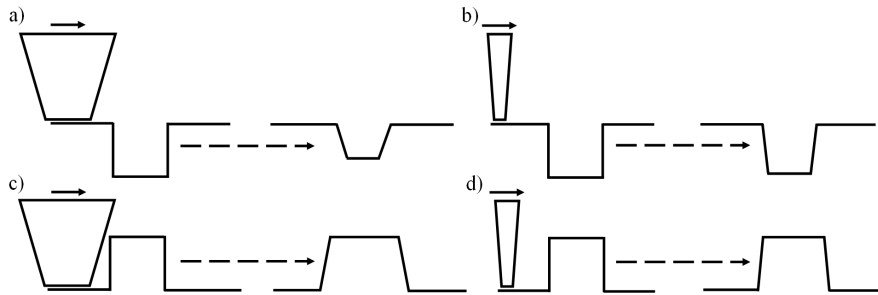


Figure 4.17: Comparison of tip convolution between large and small surface features. When surface features and tips are similar sizes, a) and c), there are significant tip convolution effects and the recorded image of the surface is distorted. When the tip is much smaller than the surface features, however, tip convolution effects are much smaller, as shown in b) and d).

## 4.6 SCANNING ELECTRON MICROSCOPY

Scanning electron microscopy (SEM) is a powerful imaging technique which can image semiconductor surfaces down to the nanometre scale. To acquire an image a electron, or sometimes ion, beam is raster scanned across the surface to be imaged. In the basic mode of operation an SEM detects the secondary electrons which are produced from the interaction of the electron beam and the inspected sample [59].

There are two distinct sections to an SEM system, these are the electron column and the electronic console. A diagram depicting what these sections contain and how they interconnect is shown in Figure 4.18.

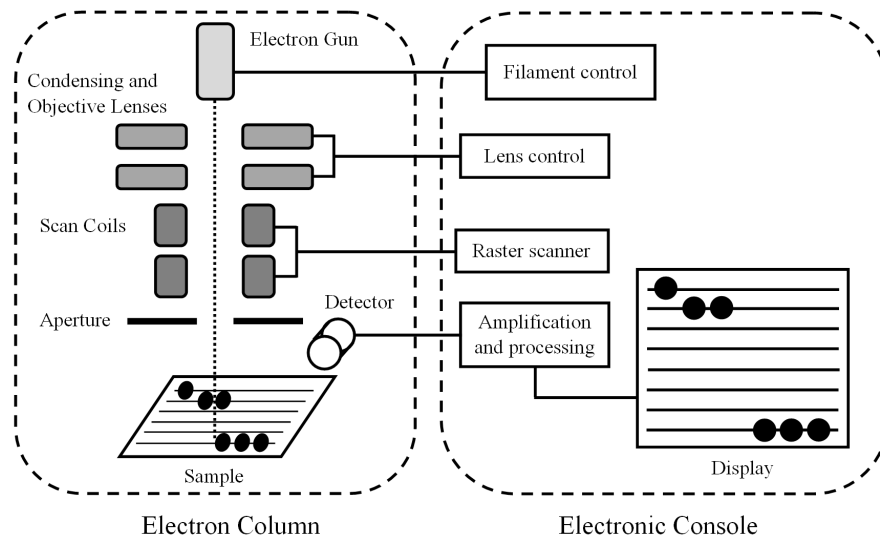


Figure 4.18: Comparison of tip convolution between large and small surface features. When surface features and tips are similar sizes, a) and c), there are significant tip convolution effects and the recorded image of the surface is distorted. When the tip is much smaller than the surface features, however, tip convolution effects are much smaller, as shown in b) and d).

#### 4.6.1 ENERGY DISPERSIVE X-RAY SPECTROSCOPY

Energy dispersive X-ray spectrometry (EDX, or also EDS) is a chemically sensitive technique which can be used with SEM, but also transmission electron microscope systems. This operates through the absorption of X-rays produced from the sample during beam bombardment. A cooled semiconductor detector produces a photo-electron when the x-rays are absorbed, this photo-electron then loses energy through the generation of a number of electron-hole pairs. A reverse bias applied to the detector separates this generated charge which is then converted into a voltage pulse. As the magnitude of the pulse is proportional to the wavelength of the absorbed X-ray it therefore contains characteristic information about the atoms present in the area of the sample being probed. Through post-processing and data modelling this can technique can be used to produce elemental maps of samples [60].

## REFERENCES

- [1] W. Binnie, “The structural crystallography of indium bismuthide,” *Acta Crystallographica*, vol. 9, no. 8, pp. 686–687, 1956.
- [2] K. Hashimoto, “Electrical properties of *SnTe*, *SnSe* and *InBi* at low temperatures,” *Journal of the Physical Society of Japan*, vol. 12, no. 12, pp. 1423–1423, 1957.
- [3] L. Wang, L. Zhang, L. Yue, D. Liang, X. Chen, Y. Li, P. Lu, J. Shao, and S. Wang, “Novel Dilute Bismide, Epitaxy, Physical Properties and Device Application,” *Crystals*, vol. 7, no. 3, p. 63, 2017.
- [4] S. M. Sze and K. K. Ng, *Physics of semiconductor devices: 3rd Ed.* John wiley & sons, 2007.
- [5] A. Bett, F. Dimroth, G. Stollwerck, and O. Sulima, “Iii-v compounds for solar cell applications,” *Applied Physics A*, vol. 69, no. 2, pp. 119–129, 1999.
- [6] A. R. Mohmad, F. Bastiman, C. Hunter, R. Richards, S. Sweeney, J. Ng, J. David, and B. Y. Majlis, “Localization effects and band gap of *GaAsBi* alloys,” *physica status solidi (b)*, vol. 251, no. 6, pp. 1276–1281, 2014.
- [7] N. Hossain, I. Marko, S. Jin, K. Hild, S. Sweeney, R. Lewis, D. Beaton, and T. Tiedje, “Recombination mechanisms and band alignment of *gaas<sub>1-x</sub>bi<sub>x</sub>*/gaas light emitting diodes,” *Applied Physics Letters*, vol. 100, no. 5, p. 051105, 2012.
- [8] Ioffe Institute, “Nsm archive - *algaas* basic parameters, [http : //www.matprop.ru/algaas\\_basic](http://www.matprop.ru/algaas_basic),” 2022.
- [9] Ioffe Institute, “Nsm archive - *algaas* band structure, [http : //www.matprop.ru/algaas\\_bandstr](http://www.matprop.ru/algaas_bandstr),” 2022.
- [10] K. K. Ng, *Complete guide to semiconductor devices 2nd Ed.* Wiley Online Library, 2002.
- [11] M. J. Howes and D. V. Morgan, “Gallium arsenide: materials, devices, and circuits,” *Chichester, England and New York, Wiley-Interscience, 1985, 592 p. No individual items are abstracted in this volume.*, 1985.
- [12] E. Borovitskaya and M. S. Shur, *Quantum dots (Selected Topics in Electronics and Systems)*, vol. 25. World scientific, 2002.
- [13] A. Pimpinelli and J. Villain, *Physics of crystal growth.* Cambridge University Press, 1999.
- [14] B. Joyce, T. Jones, and J. Belk, “Reflection high-energy electron diffraction/scanning tunneling microscopy study of *inas* growth on the three low index orientations of *gaas*: Two-dimensional versus three-dimensional growth and strain relaxation,” *Journal of Vacuum Science & Technology B: Microelectronics and Nanometer Structures Processing, Measurement, and Phenomena*, vol. 16, no. 4, pp. 2373–2380, 1998.
- [15] P. Joyce, T. Krzyzewski, G. Bell, B. Joyce, and T. Jones, “Composition of *inas* quantum dots on *gaas* (001): Direct evidence for (*in, ga*) as alloying,” *Physical Review B*, vol. 58, no. 24, p. R15981, 1998.
- [16] R. B. Lewis, A. Trampert, E. Luna, J. Herranz, C. Pfüller, and L. Geelhaar, “Bismuth-surfactant-induced growth and structure of *InAs/GaAs* (110) quantum dots,” *Semiconductor Science and Technology*, vol. 34, no. 10, p. 105016, 2019.

- [17] D. Wasserman, S. Lyon, M. Hadjipanayi, A. Maciel, and J. Ryan, "Formation of self-assembled *inas* quantum dots on (110) *gaas* substrates," *Applied physics letters*, vol. 83, no. 24, pp. 5050–5052, 2003.
- [18] Y. Arakawa and H. Sakaki, "Multidimensional quantum well laser and temperature dependence of its threshold current," *Applied physics letters*, vol. 40, no. 11, pp. 939–941, 1982.
- [19] R. Lewis, M. Masnadi-Shirazi, and T. Tiedje, "Growth of high *Bi* concentration  $GaAs_{1-x}Bi_x$  by molecular beam epitaxy," *Applied Physics Letters*, vol. 101, no. 8, p. 082112, 2012.
- [20] X. Lu, D. Beaton, R. Lewis, T. Tiedje, and M. Whitwick, "Effect of molecular beam epitaxy growth conditions on the *Bi* content of  $GaAs_{1-x}Bi_x$ ," *Applied Physics Letters*, vol. 92, no. 19, p. 192110, 2008.
- [21] R. D. Richards, N. J. Bailey, Y. Liu, T. B. Rockett, and A. R. Mohmad, "*GaAsBi*: From Molecular Beam Epitaxy Growth to Devices," *physica status solidi (b)*, p. 2100330, 2021.
- [22] R. D. Richards, F. Bastiman, C. J. Hunter, D. F. Mendes, A. R. Mohmad, J. S. Roberts, and J. P. David, "Molecular beam epitaxy growth of *GaAsBi* using  $As_2$  and  $As_4$ ," *Journal of Crystal Growth*, vol. 390, pp. 120–124, 2014.
- [23] C. Foxon and B. Joyce, "Interaction kinetics of  $as_4$  and *ga* on (100) *gaas* surfaces using a modulated molecular beam technique," *Surface Science*, vol. 50, no. 2, pp. 434–450, 1975.
- [24] E. Tok, J. Neave, J. Zhang, B. Joyce, and T. Jones, "Arsenic incorporation kinetics in *gaas* (001) homoepitaxy revisited," *Surface science*, vol. 374, no. 1-3, pp. 397–405, 1997.
- [25] S. Francoeur, M.-J. Seong, A. Mascarenhas, S. Tixier, M. Adamcyk, and T. Tiedje, "Band gap of  $GaAs_{1-x}Bi_x$ ,  $0 < x < 3.6\%$ ," *Applied physics letters*, vol. 82, no. 22, pp. 3874–3876, 2003.
- [26] S. Tixier, M. Adamcyk, T. Tiedje, S. Francoeur, A. Mascarenhas, P. Wei, and F. Schiettekatte, "Molecular beam epitaxy growth of  $GaAs_{1-x}Bi_x$ ," *Applied physics letters*, vol. 82, no. 14, pp. 2245–2247, 2003.
- [27] K. Alberi, J. Wu, W. Walukiewicz, K. Yu, O. Dubon, S. Watkins, C. Wang, X. Liu, Y.-J. Cho, and J. Furdyna, "Valence-band anticrossing in mismatched iii-v semiconductor alloys," *Physical review B*, vol. 75, no. 4, p. 045203, 2007.
- [28] K. Alberi, O. Dubon, W. Walukiewicz, K. Yu, K. Bertulis, and A. Krotkus, "Valence band anticrossing in  $gabi_xas_{1-x}$ ," *Applied Physics Letters*, vol. 91, no. 5, p. 051909, 2007.
- [29] A. Mohmad, F. Bastiman, J. Ng, S. Sweeney, and J. David, "Photoluminescence investigation of high quality  $GaAs_{1-x}Bi_x$  on GaAs," *Applied Physics Letters*, vol. 98, no. 12, p. 122107, 2011.
- [30] M. Yoshimoto, M. Itoh, Y. Tominaga, and K. Oe, "Quantitative estimation of density of *Bi*-induced localized states in  $GaAs_{1-x}Bi_x$  grown by molecular beam epitaxy," *Journal of crystal growth*, vol. 378, pp. 73–76, 2013.
- [31] S. Imhof, A. Thränhardt, A. Chernikov, M. Koch, N. S. Köster, K. Kolata, S. Chatterjee, S. W. Koch, X. Lu, S. R. Johnson, *et al.*, "Clustering effects in  $Ga(AsBi)$ ," *Applied Physics Letters*, vol. 96, no. 13, p. 131115, 2010.

- [32] P. G. Eliseev, P. Perlin, J. Lee, and M. Osiński, ““blue” temperature-induced shift and band-tail emission in *ingan*-based light sources,” *Applied physics letters*, vol. 71, no. 5, pp. 569–571, 1997.
- [33] A. Mohmad, B. Majlis, F. Bastiman, C. Hunter, R. Richards, J. Ng, and J. David, *Photoluminescence from localized states in GaAsBi epilayers*.
- [34] Xiamen Powerway Advanced Material Co., “*gaas* wafer product line, <https://www.powerwaywafer.com/gaas-wafers/gaas-wafer.html>,” 2022.
- [35] Xiamen Powerway Advanced Material Co., “*inp* wafer product line, <https://www.powerwaywafer.com/compound-semiconductor/inp-wafer.html>,” 2022.
- [36] A. F. Phillips, S. J. Sweeney, A. R. Adams, and P. J. Thijs, “The temperature dependence of 1.3- and 1.5- $\mu\text{m}$  compressively strained InGaAs (P) MQW semiconductor lasers,” *IEEE Journal of selected topics in quantum electronics*, vol. 5, no. 3, pp. 401–412, 1999.
- [37] I. P. Marko and S. J. Sweeney, “Progress toward III–V bismide alloys for near-and midinfrared laser diodes,” *IEEE Journal of Selected Topics in Quantum Electronics*, vol. 23, no. 6, pp. 1–12, 2017.
- [38] Y. Liu, X. Yi, N. J. Bailey, Z. Zhou, T. B. Rockett, L. W. Lim, C. H. Tan, R. D. Richards, and J. P. David, “Valence band engineering of *GaAsBi* for low noise avalanche photodiodes,” *Nature Communications*, vol. 12, no. 1, pp. 1–8, 2021.
- [39] B. Ng, J. David, G. Rees, R. Tozer, M. Hopkinson, and R. Airey, “Avalanche multiplication and breakdown in  $\text{Al}_x\text{Ga}_{1-x}\text{As}$  ( $x < 0.9$ ),” *IEEE Transactions on Electron Devices*, vol. 49, no. 12, pp. 2349–2351, 2002.
- [40] E. H. Parker, *The technology and physics of molecular beam epitaxy*. Plenum press New York, 1985.
- [41] B. R. Pamplin, *Molecular beam epitaxy*. Elsevier, 2013.
- [42] B. D. Power, *High vacuum pumping equipment*. Reinhold Publishing Corporation, 1966.
- [43] C. Wang, L. Wang, X. Wu, Y. Zhang, H. Liang, L. Yue, Z. Zhang, X. Ou, and S. Wang, “Molecular beam epitaxy growth of  $\text{AlAs}_{1-x}\text{Bi}_x$ ,” *Semiconductor Science and Technology*, vol. 34, no. 3, p. 034003, 2019.
- [44] R. Farrow, “The stabilization of metastable phases by epitaxy,” *Journal of Vacuum Science & Technology B: Microelectronics Processing and Phenomena*, vol. 1, no. 2, pp. 222–228, 1983.
- [45] M. Pillai, S.-S. Kim, S. Ho, and S. Barnett, “Growth of  $\text{in}_x\text{ga}_{1-x}\text{as/gaas}$  heterostructures using *bi* as a surfactant,” *Journal of Vacuum Science & Technology B: Microelectronics and Nanometer Structures Processing, Measurement, and Phenomena*, vol. 18, no. 3, pp. 1232–1236, 2000.
- [46] K. Sakamoto, K. Kyoya, K. Miki, H. Matsuhata, and T. Sakamoto, “Which surfactant shall we choose for the heteroepitaxy of *ge/si* (001) questionable - *bi* as a surfactant with small self-incorporation,” *Japanese journal of applied physics*, vol. 32, pp. 204–206, 1993.
- [47] E. Tournie, N. Grandjean, A. Trampert, J. Massies, and K. Ploog, “Surfactant-mediated molecular-beam epitaxy of iii–v strained-layer heterostructures,” *Journal of crystal growth*, vol. 150, pp. 460–466, 1995.
- [48] A. Ichimiya and P. I. Cohen, *Reflection high-energy electron diffraction*. Cambridge University Press, 2004.

- [49] R. A. Stradling, *Growth and Characterisation of Semiconductors: Papers Contributing to a Short Course Organised by the Departments of Materials and Physics with... at the Imperial College of Science, Technology and Medicine, University of London...* Hilger, 1991.
- [50] L. Däweritz and R. Hey, "Reconstruction and defect structure of vicinal  $GaAs$  (001) and  $Al_xGa_{1-x}As$  (001) surfaces during MBE growth," *Surface Science*, vol. 236, no. 1-2, pp. 15–22, 1990.
- [51] Y. P. Varshni, "Temperature dependence of the energy gap in semiconductors," *physica*, vol. 34, no. 1, pp. 149–154, 1967.
- [52] R. Jenkins and J. Vries, *Practical X-ray spectrometry*. Springer, 1969.
- [53] P. Luger, *Modern X-Ray Analysis on Single Crystals: A Practical Guide 2nd Ed.* Walter de Gruyter, 2014.
- [54] T. S. Tkaczyk, *Field guide to microscopy*. The Society of Photographic Instrumentation Engineers (SPIE), Bellingham, Washington, 2010.
- [55] D. B. Murphy, *Fundamentals of light microscopy and electronic imaging*. John Wiley & Sons, 2002.
- [56] L. Brillson, *Surfaces and interfaces of electronic materials, first edition, 2010*. Wiley-VCH, Weinheim, 2010.
- [57] M. Mayer, *Rutherford backscattering spectrometry (RBS)*., vol. 34. Workshop on Nuclear Data for Science and Technology Materials Analysis, 2003.
- [58] P. Eaton and P. West, *Atomic force microscopy*. Oxford university press, 2010.
- [59] G. Van Tendeloo, D. Van Dyck, and S. J. Pennycook, *Handbook of Nanoscopy*. John Wiley & Sons, 2012.
- [60] G. Lawes, J. Goldstein, D. E. Newbury, P. Echlin, D. C. Joy, A. D. Romig Jr, C. E. Lyman, C. Fiori, E. Lifshin, *et al.*, *Scanning Electron Microscopy and X-Ray Microanalysis: A Text for Biologists, Materials Scientists, and Geologists*. Springer, 1992.

## PART II

# PHOTO-LUMINESCENCE MODELLING OF LOCALISED STATES IN *GaAsBi*

## 5 LITERATURE REVIEW

It has been widely observed that the incorporation of *Bi* into *GaAsBi* leads to the formation of a localised density of states (LDOS) above the valence band [1, 2], as mentioned in Section 2.7.2. These states have been directly discussed, as in [1, 2], but their fingerprints can be seen in other reports which discuss the broad luminescence which is commonly seen in this material [3, 4]. Using temperature dependent photo-luminescence (PL) measurements, the effect of these states can also be observed in an 's' shaped deviation from the standard Varshni trend which classical semiconductors follow [2, 5]. Yoshimoto *et al.* [6] have demonstrated suppression of this effect using p-doping and were able to estimate that approximately 0.2 % of incorporated *Bi* atoms contribute to these localised states. Temperature dependent PL studies have also indicated that the depth to which these states exist is up to around 90 *meV* above the valence band [6, 7].

There has been much investigation into the nature of these states across various literature reports with varying agreement on how they are distributed in *GaAsBi*. Imhof *et al.* [8] used a Monte Carlo model where a Gaussian and an exponential distribution represented alloy fluctuation and *Bi* clustering, respectively. A two-scale modelling approach has also been used by Valkovskii *et al.* [9], here they suggested the existence of two distinct types of localised states with different temperature dependent non-radiative rates. This was applied through Monte Carlo modelling to replicate fits to FWHM and Stokes shift data for a gallium nitride arsenide phosphide layer which, due to the manifestation of similar localised state effects, was considered representative of *GaAsBi*. Gogineni *et al.* [10] found that two exponential functions well approximated the low energy emission tail of a *GaAsBi* quantum well layer and identified two characteristic energies in the tail states which were attributed to alloy fluctuations and *Bi* clustering. Another model which has looked at two distinct components to the LDOS is by Shakfa *et al.* [11]. This work looked at the thermal quenching behaviour of several thin *GaAsBi* layers with *Bi* contents varying from 2.9 up to 4.5 % and found that any combination of Gaussian and exponential profiles could fit a plateau seen in the experimental data although it was noted that the use of an exponential truncated by a Heaviside step function to represent the deeper states was not physically realistic.

A separate modelling method to those mentioned above was employed by Wilson *et al.* [12]. They assumed in their model that recombination from the localised states was entirely radiative and therefore, at low temperature (LT), the PL would give a good approximation to the distribution of states. This model functioned as a convolution between a Gaussian distribution representing inherent exciton broadening associated with material defects and a profile for the localised density of states above the valence band. This model was applied to the LT power-dependent (PD) PL of a bulk *GaAs<sub>0.947</sub>Bi<sub>0.053</sub>* layer at 30 *K* with either a Gaussian or exponential distribution profile for the LDOS. By comparison of the best fit quality across the range of excitation powers it was deemed that a Gaussian distribution best described the localised state distribution with a characteristic

energy of 100 *meV*.

It is clear from reports in the literature that the growth conditions of *GaAsBi* have a significant impact on its PL properties [13] and it can be expected from this that there is a similarly significant impact on the localised states. There has not, however, been an in-depth study looking at the separate effects of growth temperature and *Bi* flux on the localised states apart from recent work by Kakuyama *et al.* [14]. In their work two sets of three *GaAsBi* layers were studied where each set was grown 20 °C apart, 360 or 380 °C, using one of three *Bi* fluxes. This growth produced a set of layers covering a similar range of *Bi* contents but with differing growth temperatures. Evidenced by a reduction in the Urbach energy, the exponential trend in the low-energy absorption tail seen in multiple materials [15], they found that the higher growth temperature reduced localised state formation.

In this chapter a more in-depth study of the effect of the growth conditions on localised state formation is undertaken. The model presented by Wilson *et al.* in [12] will be augmented and applied to a wider range of growth temperatures and *Bi* fluxes than implemented by Kakuyama *et al.* [14] in order to develop a more comprehensive understanding of the growth parameter space. The aim of this work is to develop the established model such that it can be used to consistently fit a range of *GaAsBi* layers and then compare the fitting parameters in order to investigate the independent effects of both growth temperature and *Bi* flux on localised state formation. LT PD PL measurements were taken for this work, with supporting EDX images and data provided by D. Reyes from IMEYMAT at the University of Cadiz.

## 6 EXPERIMENTAL SETUP

### 6.1 GROWTH CONDITION LAYERS

The growth of the layers used here has been previously reported in [13] where it was found through room-temperature material and device characterisation that both the growth temperature and *Bi* flux impact material quality and device dark currents although the growth temperature produced the strongest impact. One of the key interesting features of this series are two pairs of devices (STG3A/STG35 and STG3D/STG38) which have similar *Bi* contents despite a large difference in their growth conditions. By comparing the results of the model applied to these pairs and the rest of these layers the independent effects of the growth conditions can be easily examined. A summary of these layers is shown in Table 6.1 below.

The data which was collected and modelled for these layers was power-dependent PL at 30 *K* using the setup described in Section 4.1. To reduce sample heating the laser was operated in pulsed mode with a 1 *ms* on-period and 2 *ms* off-period resulting in a 33 % duty cycle. Dopant luminescence (from the *Si* donor states in the *GaAs* substrates) which was visible and overlapping for some of the layers was removed using a scaled PL spectrum taken on a raw substrate at the same temperature, this is illustrated for layer STG3C in Figure 6.1. Fits to both the raw and corrected data will be given in Section 7.

Layer	Growth Temperature ( $^{\circ}\text{C}$ )	Bi BEP ( $10^{-7}\text{mbar}$ )	Bi content (%) (PL/XRD)
STG3C	355	1.06	3.6/3.51
STG34	375	1.06	3.2/3.25
STG36	385	1.06	2.7/2.82
STG35	395	1.06	2.2/2.19
STG38	405	1.06	1.3/1.37
STG3D	375	0.5	1.2/1.31
STG3A	375	0.76	2.2/2.25
STG3B	375	1.5	4.0/4.12
STG39	375	2.12	5.3/5.37

Table 6.1: STG3 growth conditions [13]. This consists of two series, one where the growth temperature varies from 355 – 405  $^{\circ}\text{C}$  and another where the Bi BEP increases from 0.5 – 2.12  $\times 10^{-7}$  mbar

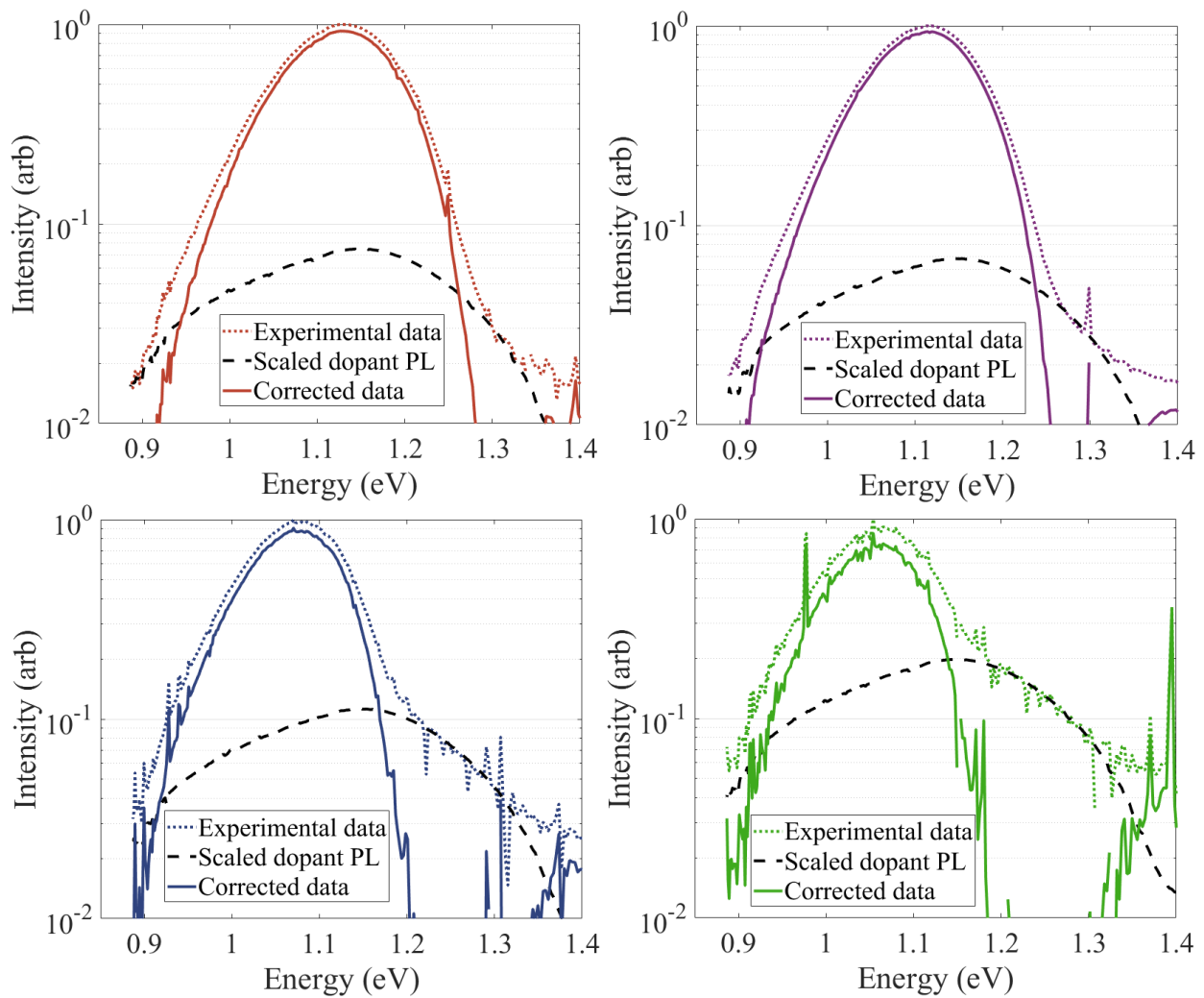


Figure 6.1: Raw experimental and corrected spectra for layer STG3C at a) 900, b) 300, c) 90 and d) 30 mW excitation power.

## 6.2 PL MODEL

As mentioned in the literature review this chapter involves modelling of LT PL from *GaAsBi* layers. The workings of these models is difficult to grasp from only a written description, however, so before delving into the equations discussing their behaviour a series of diagrams will be presented to give a general understanding of what they represent. This is done with Figure 6.2 which starts with a familiar cartoon of the density of states diagram for *GaAs* in 6.2a.

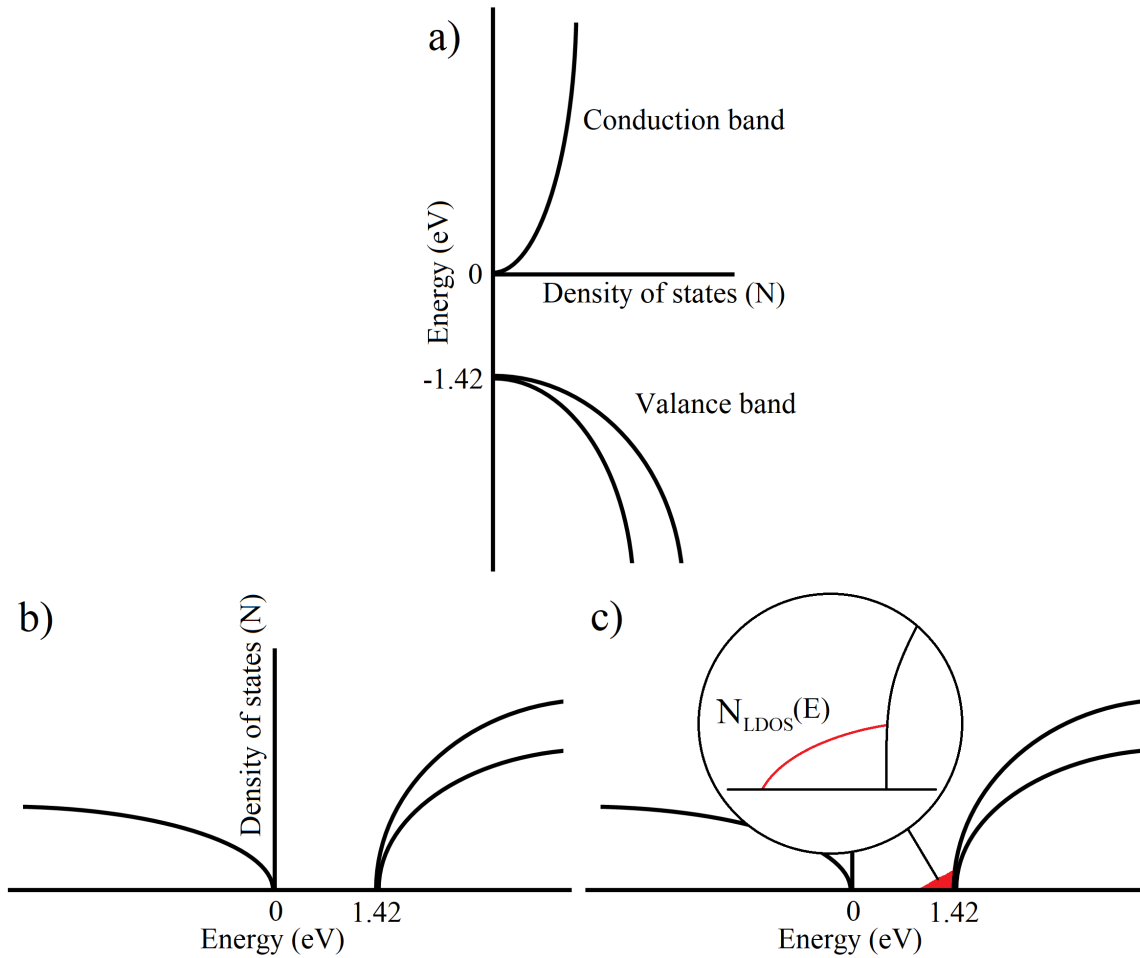


Figure 6.2: a) A density of states band diagram based on *GaAs*, offset to 0 eV at the start of the conduction band. b) The previous graph with the axes flipped. The energy axis has also been inverted to indicate the energy of holes in the valence band. c) If we now add a small distribution of localised states trailing into the band gap below the valence band (in terms of hole energy), we can label it with a density equation  $N_{LDOS}(E)$ . Due to the low LDOS density relative to the conduction band states, any hole recombination is assumed to happen with an electron at 0 eV so the energy released is equal to the hole energy defined by the localised state.

The form of  $N_{LDOS}(E)$  in 6.2c is what was discussed in the literature review to be either exponential or Gaussian. It is the crux of novel development in this chapter and will be presented after an overview of the model reported by Wilson *et al.* [12].

The original model equation presented by Wilson *et al.* is shown in Equation 6.1.  $E$  is the energy at which the

modelled PL intensity is being evaluated,  $E_0$  is a parameter for performing the integration,  $\sigma_{Gauss}$  is the shape parameter for the Gaussian emission profile for the localised states,  $E_{Mob}$  is the material band gap and  $\sigma_{LDOS}$  is the shape parameter for the distribution of localised states. The form of  $N_{LDOS}$  was taken as either a Gaussian (Eq. 6.2) or an exponential (Eq. 6.3) function which centred or started, respectively, on the band edge,  $E_{Mob}$ .

$$I_{eff}(E) = \int_{-\infty}^{E_{Max}} g_{Gauss}(E, E_0, \sigma_{Gauss}) \times N_{LDOS}(E_0, E_{Mob}, \sigma_{LDOS}) \cdot dE_0 \quad (6.1)$$

$$N_{LDOS}(E, E_0, \sigma) = \frac{1}{\sqrt{2\pi\sigma^2}} \exp^{-\frac{(E-E_0)^2}{2\sigma^2}} \quad (6.2)$$

$$N_{LDOS}(E, E_0, \sigma) = \frac{1}{\sqrt{\sigma}} \exp^{-\frac{(E-E_0)}{\sigma}} \quad (6.3)$$

Figure 6.3 shows the results presented in the original implementation of the model. The layer which was modelled in this Figure was a bulk 130 nm GaAsBi layer with 5.3 % Bi grown at 340 °C. Whilst both distribution types were able to fit this layer at low excitation power, it can be clearly seen that the Gaussian distribution produced a better fit throughout the full excitation power range. In the preliminary results on the STG3 layers, however, neither a single Gaussian or exponential distribution produced an adequate fit to most of the layers. Only STG3C which was grown at the lowest temperature, and closest to that used by Wilson *et al.*, resulted in a good fit when using a Gaussian distribution. Considering there are significant line-shape changes which were seen in the LT PD PL from the STG3 layers, shown in Figures 6.4 and 6.5, and also the significant literature discussion of a non-monotonous LDOS [8, 9, 10, 11], it was decided to adapt the model to use a two component profile for the LDOS. It is this adapted version which was used to produce the results in Section 7 and will now be presented.

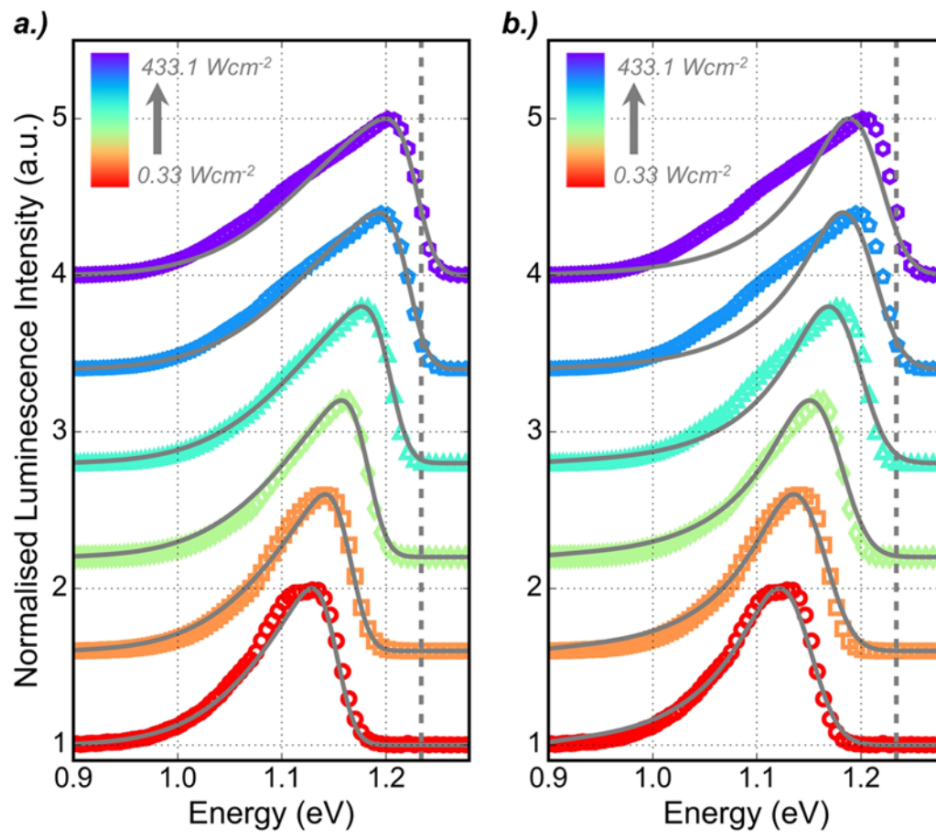


Figure 6.3: Results from [12] using a) Gaussian and b) exponential functions to represent the localised state distribution. Of the model parameters, only  $E_{Max}$  which represents state filling was varied between different excitation powers. Material from: T. Wilson et al., *Assessing the Nature of the Distribution of Localised States in Bulk GaAsBi*, *Scientific Reports*, published 2018, Springer Nature. License available at: (<http://creativecommons.org/licenses/by/4.0/>). Part c) of this Figure was removed due to irrelevant content.

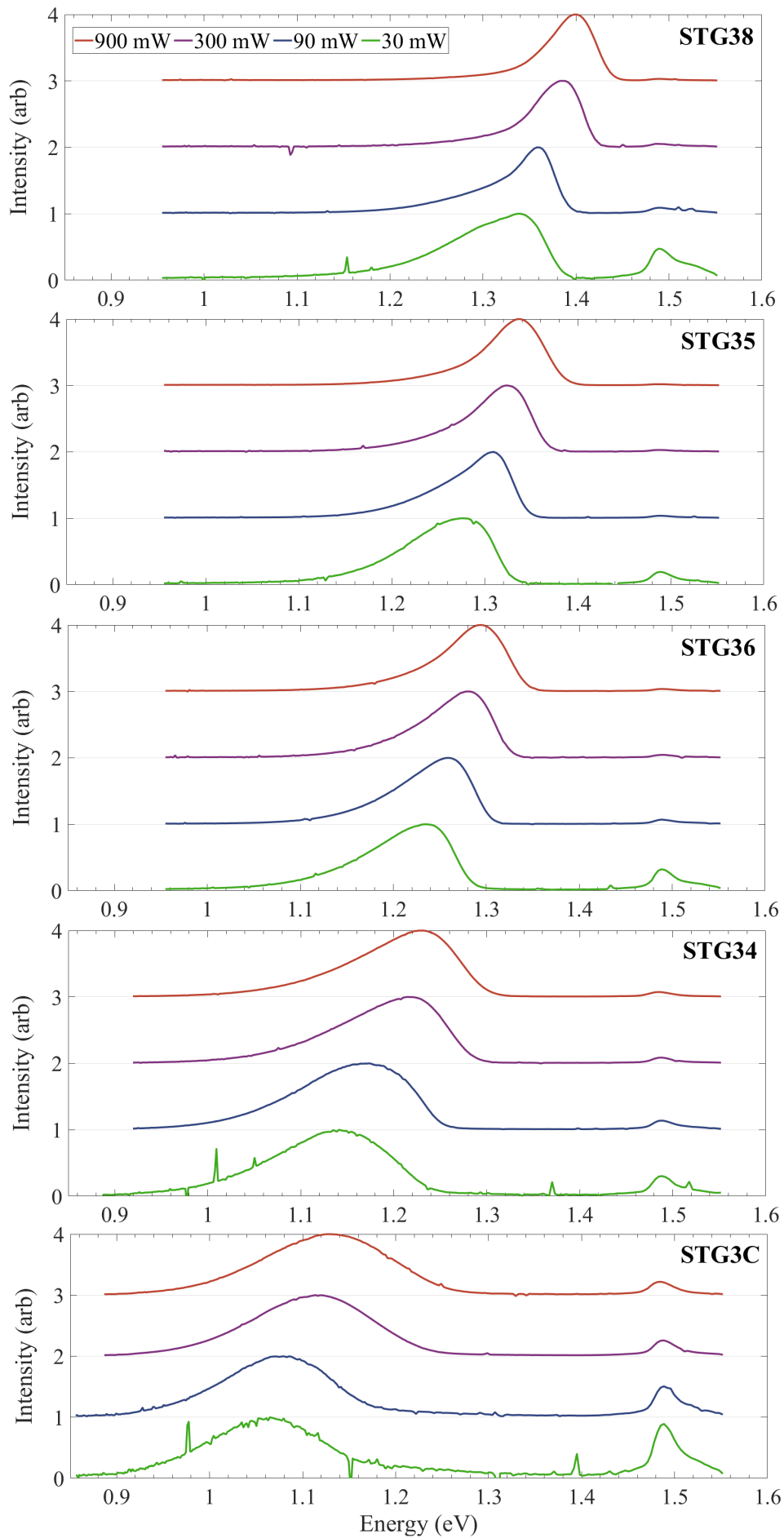


Figure 6.4: Raw PL for the growth temperature series. Different excitation powers have been offset for clarity.



The primary assumptions of this model is that at low temperatures (10 - 40 K) all photo-excited carriers will have sufficient energy to hop/drop to the deepest localised states [16] and that the thermal broadening of the PL due to carriers following a fermi-dirac distribution will be negligible compared to the other broadening effects in this material. Accepting these assumptions means that the PL within this temperature range should, therefore, give an accurate representation of the distribution of localised states. This leads to the formation of the model shown in Equation 6.4 and the illustration in Figure 6.6.

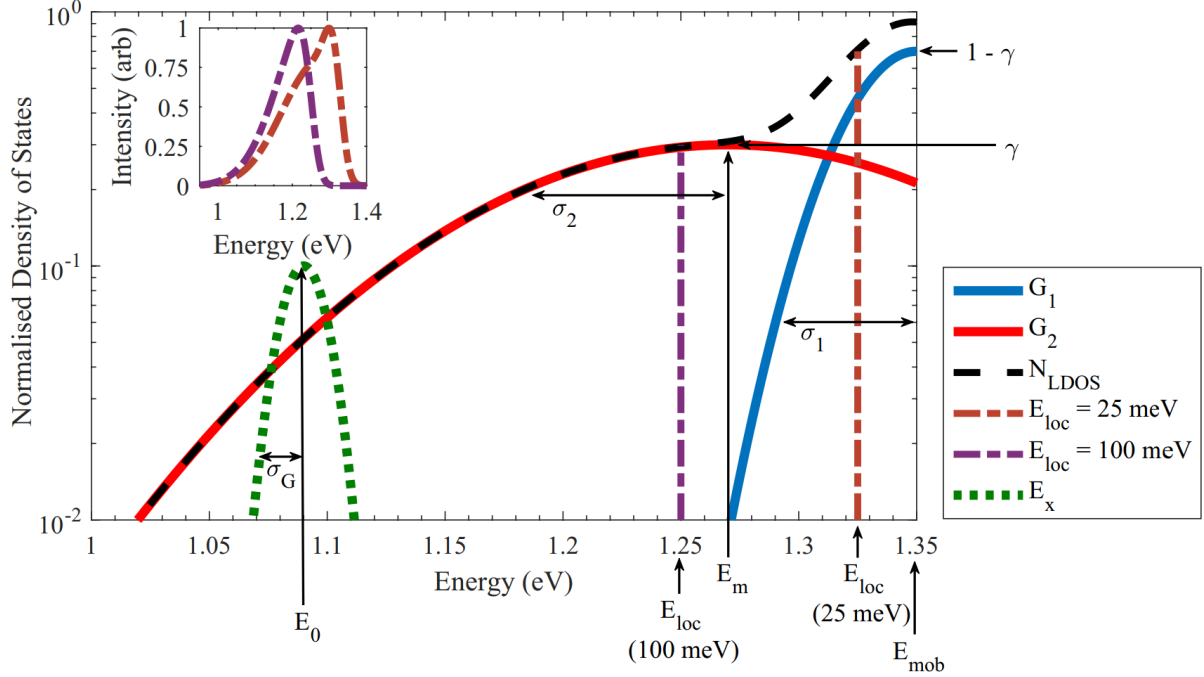


Figure 6.6: Illustration of the adapted Wilson et al. model. This is essentially a more detailed, skeleton version of the general localised state distribution sketched in Figure 6.2c. Each parameter from Equation 6.4 has been labelled to indicate its meaning. The inset shows the equivalent modelled PL line-shape for the two different localisation energies which are labelled in the Figure.

$$I_{eff}(E) = \int_{-\infty}^{E_{Max}} E_x(E, E_0, \sigma_G) \times N_{LDOS}(E, E_{Mob}, E_m, \sigma_1, \sigma_2, \gamma) \cdot dE_0 \quad (6.4)$$

$$N_{LDOS}(E) = [(1 - \gamma) \times G_1(E, E_{Mob}, \sigma_1)] + [\gamma \times G_2(E, E_m, \sigma_2)] \quad (6.5)$$

Equation 6.4 shows the overall form of the adapted model. Apart from the renaming of some parameters, the main changes to note are the addition of three new variables,  $E_m$ ,  $\sigma_2$  and  $\gamma$  which are used to define the second profile added to ( $N_{LDOS}$ ).  $E_m$  is the centre energy for the second distribution,  $\sigma_2$  is its shape parameter and  $\gamma$  is used to set the relative magnitude of the two distributions. The process of calculating and combining the two components of this new  $N_{LDOS}$  is shown in Equation 6.5. It is important to note that in order to maintain consistency in the summation of  $G_1$  and  $G_2$ , when the broadening parameters ( $\sigma_{1/2}$ ) were changed, the individual distributions were normalised to 1 before Equation 6.5 was evaluated. Given the results of [8, 11, 12] it was also decided to restrict both distributions to Gaussian functions as they were found to be the best for the

primary distribution ( $G_1$ ), or the only distribution in [12], and are the most physically realistic for the offset distribution ( $G_2$ ).  $G_1$  and  $G_2$  were calculated in the same way as  $E_x$ , all of which follow Equation 6.2.

It can be seen in Figure 6.6 how the profile for the localised density of states,  $N_{LDOS}$  (dashed black line), is formed from the two component Gaussian distributions (blue and red lines). Now let us imagine that under some arbitrary optical excitation this LDOS profile is filled up to a certain energy, 1.25 eV for instance (dot-dashed purple line). If we now convolve this filled LDOS profile with  $E_x$  (green dotted line) which represents broadening of the exciton emission due to crystalline defects the result is the modelled PL spectrum (purple dot-dashed inset). If the same process were repeated at a higher laser power which excites more carriers, fills the LDOS higher and reduces the localisation energy (orange dot-dashed line) then we can see how the modelled PL begins to show a distinct shoulder at low energy (orange dot-dashed inset). It is this feature, which occurs when the value of  $G_2$  becomes larger than  $G_1$ , that the original model was unable to reproduce using a single distribution and is key to fitting some of the trends seen in Figures 6.4 and 6.5. The list below summarises the various model parameters with a description of their function in the model and their physical significance.

- $E_{mob}$ : The band edge of the *GaAsBi* layer. In the model this positions the centre of of the  $G_1$  distribution (representing alloy fluctuations).
- $E_m$ : The centre energy of  $G_2$ . This indicates the energy at which the density of localised states (originating from *Bi* clusters for this distribution) is highest.
- $E_{max}$ : Calculated as  $E_{Mob} - E_{loc}$ . Physically this represents the energy level to which the states are filled with carriers and above which all states are empty. In the model this filling variable sets the stopping point for the convolution of  $E_x$  and  $N_{LDOS}$ . It is this variable which allows the model to account for multiple spectra taken under different excitation powers for a layer whilst keeping all other parameters fixed.
- $\sigma_G$ : The exciton broadening standard deviation. This dictates the range of energies of which a given exciton (a bound electron-hole pair) can emit at.
- $\sigma_{LDOS_1}$ : Shape parameter for localised state distribution centred on the band edge. This indicates the energy range which the alloy fluctuation within the material covers.
- $\sigma_{LDOS_2}$ : Shape parameter for localised state distribution offset from the band edge. Physically this is the energy range covered by cluster states within the material.
- $\gamma$ :  $G_1$  and  $G_2$  weighting parameter. Sets the relative peak densities of the two distributions in  $N_{LDOS}$ . Physically this would represent the relative densities of the two LDOS distributions within the material.

### 6.3 MODEL IMPLEMENTATION

Implementation of the model was performed using a *MATLAB* script which was personally written from scratch for this work. This script consisted of a basic front-end User Interface (UI) and back-end brute-force algorithm. The final design of the UI is displayed in Figure 6.7. It is initialised here with default parameter values and

without a model fit. Whilst running, the fitting program changes the model parameters to improve the model fit compared to the experimental PL data. The fit quality was evaluated as a Root Mean Square Error (RMSE) between the experimental data and the model fit over an appropriate wavelength range which was taken as either the experimental PL dropping below 1 % of its maximum intensity, or hitting the noise floor. This is shown in Equation 6.6.

$$RMSE = \sqrt{(Experimental - Model)^2} \quad (6.6)$$

Starting at the bottom left of Figure 6.7 is the model parameters panel. This has multiple sections which are briefly summarised below:

- A group of six text boxes, one for each of the model input parameters.
- Two drop-down selection menus for distribution type.
- Ten output boxes grouped into six and four for model parameters and localisation energies, respectively.
- Four pairs of input-output boxes for varying localisation energy and viewing the RMSE value for each spectra. Accompanying checkboxes allow the localisation energy values to be fixed during fit trialling.
- A push button ‘Run Auto’ to run the model algorithm and find the best fit to the data.

The four panels on the right-hand side of Figure 6.7 display the normalised experimental PL for one of layer STG3A in order of descending excitation power. Each of these panels contains two text boxes for setting the wavelength range over which the program will compare the experimental and modelled PL values.

The top left panel of Figure 6.7 displays the profile for the LDOS relative to the valance band edge at 0 eV. This updates as the variables which dictate its shape in the parameter panel are changed. At the bottom of this panel are two output boxes displaying the overall model mean RMSE and standard deviation of the individual RMSE’s. To their left are two buttons, one to switch between logarithmic and linear scaling on the right hand side spectra plots and the other to generate a summary figure of the experimental data and model fits.

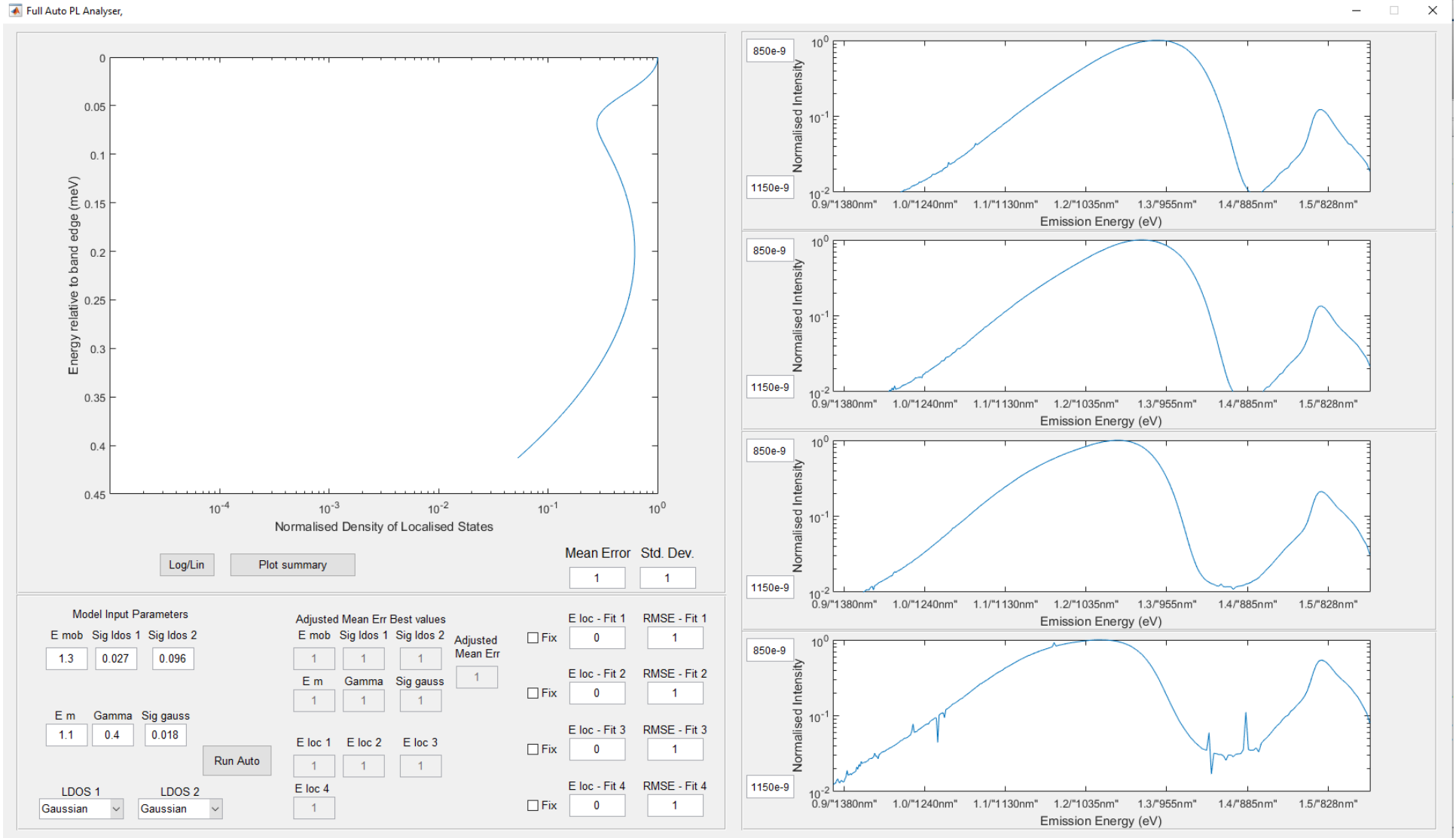


Figure 6.7: PL Model UI

## 6.4 MODEL CONSTRAINTS, FINDING THE BEST FIT AND CALCULATING ERROR BARS

With six different variables for each layer plus an extra variable specific to each spectrum, ( $E_{loc}$ ), and a wide area of parameter space to cover it was unfeasible to consider running the model as a purely brute force method at a suitably fine resolution as it would take weeks or possibly even months to finish.

The first technique used to decrease the time required to find the best fit was to apply a series of suitable constraints to the model. Several of these were easily defined as the model must obey the basic laws of physics, i.e all the energies must be a positive real value (minimum set to 1  $meV$ ) and  $0 \leq \gamma \leq 1$ . The two further constraints which were applied, however, required more justification. In unconstrained testing of the adapted model it was found that the values of  $\sigma_{LDOS_1}$  and  $\sigma_{LDOS_2}$  tended to similar values for all the layers so it was decided to fix these parameters at their mean values of 27 and 96  $meV$  for  $\sigma_{LDOS_1}$  and  $\sigma_{LDOS_2}$  respectively.

This value of 27  $meV$  is close to experimental values seen in the standard deviation of  $Bi$  content. This is seen in EDX measurements of other  $GaAsBi$  layers which are shown in Figure . Converting the standard deviation into an equivalent energy range using the relationship between  $Bi$  content and band gap [5] produces energy deviation values of 15.5 - 21  $meV$  [17] which are in reasonable agreement with the value found by this model. The standard deviation value for the secondary distribution, 96  $meV$ , is also almost identical to that found in the original model paper [12] and is in broad agreement with the reports of the depth to which localised states exist [6, 7].

The final parameter which was constrained was  $E_{Mob}$ . This constriction was required as the model was tending to use unfeasibly high values of  $E_{Mob}$  (above the  $GaAs$  band gap) in order to produce negligibly small improvements in the RMSE of the fits. This parameter was therefore set at the equivalent band gap for  $GaAsBi$  ( $\pm 25 meV$ ). The band gap was calculated using the  $Bi$  content extracted from XRD measurements [13] and the relationship between  $Bi$  content and band gap modelled by Mohmad *et al.* [5]. As the relationship in [5] gives a room temperature band gap this was also blue-shifted for a 30  $K$  equivalent using the Varshni data for layer STG38 which was presented earlier in Section 4.1.1.

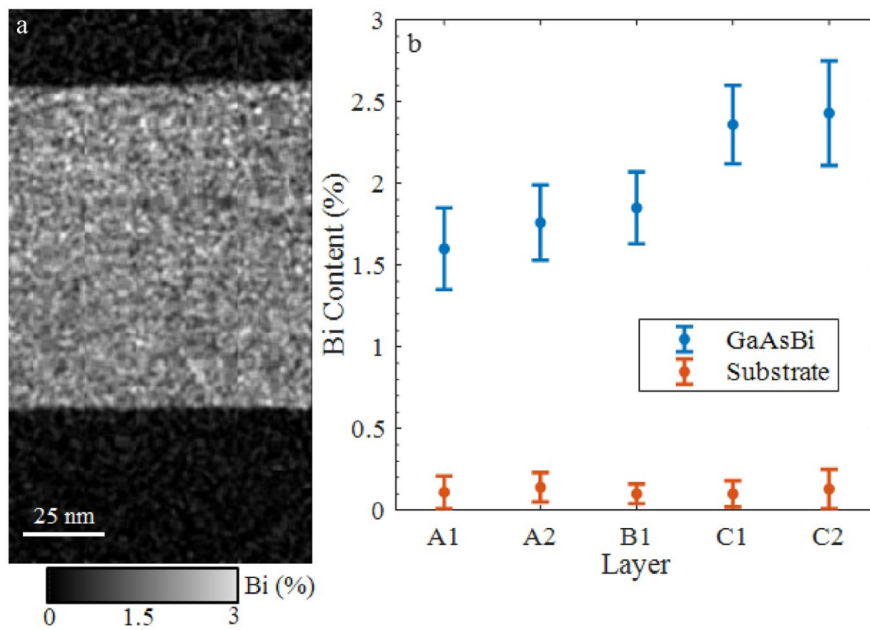


Figure 6.8: a) EDX image of a GaAsBi layer and b) Bi content in the substrate and GaAsBi layer with standard deviation (error bars) for a series of GaAsBi structures.

To cover the remaining wide area of parameter space efficiently, a process of gradually reducing the step size of the model was devised. This was performed as depicted in Figure 6.9 which refers to the operation of the model version displayed in Figure 6.7. First the program takes the initial variables input with the model as a baseline with an accompanying RMSE value. It then iterates all the variables with a large step size checking the RMSE for all possible combinations of the model variables in the range of  $-2\times$  to  $+2\times$  the step size given. If there has been any improvement in the RMSE then this step is repeated with the best parameters now being set as the starting conditions. This continues until no improvement is found after which the iteration loop sequence is repeated but with a smaller step size in the model variables. When no further improvement is found at the smallest step size the model is finished and the best fit parameters are returned. This whole process appears very basic in Figure 6.9 but practically in the code this consists of four nested loop functions with many if/else decisions to control the flow of the program. To avoid the visual complexity of displaying all these choices here, a green dashed border has been added around the equivalent sequence over which this repetition and nesting takes place.

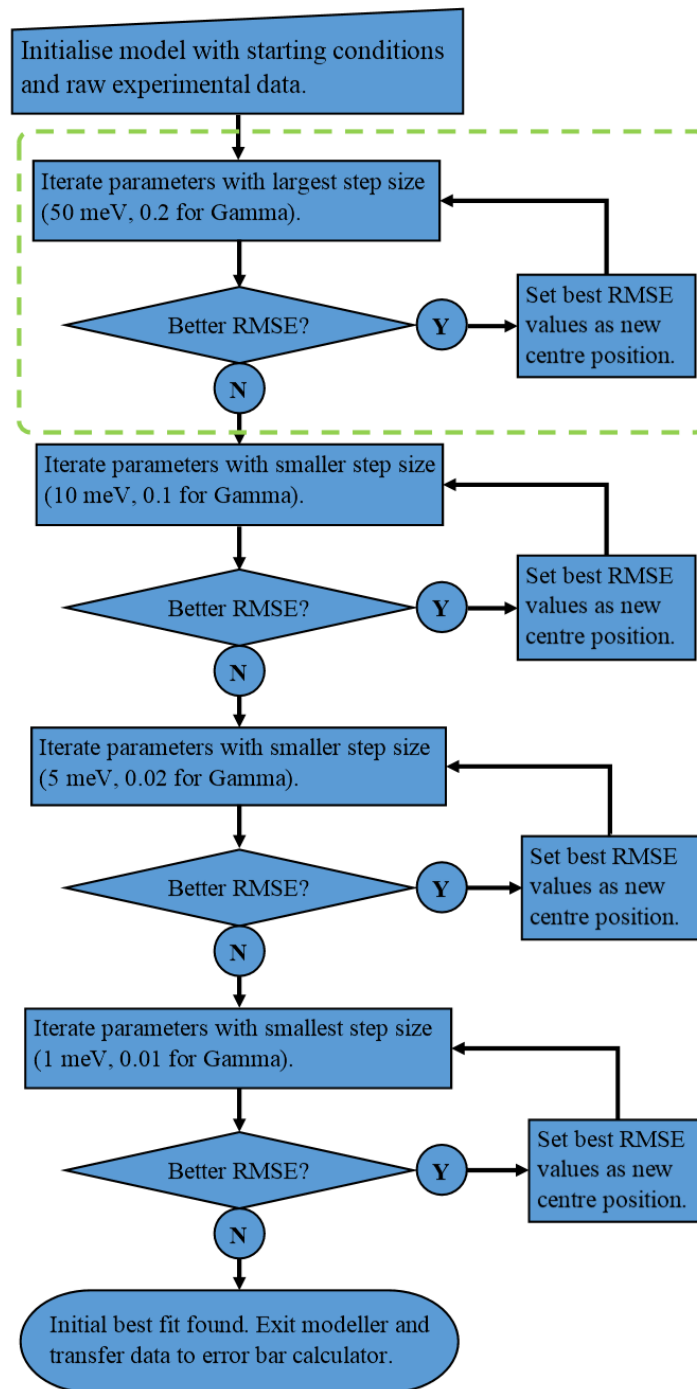


Figure 6.9: Flowchart of the primary modeller showing the high level steps and decisions made during operation. The multidimensionality of the code which simultaneously runs for each parameter is highlighted in a green dashed box.

The logical flow described in Figure 6.9 assumes that all the model variables have an associated error trend which closely follows an ideal curve similar to that shown in Figure 6.10a. The reality, however, is more likely to be similar to Figure 6.10b where there are multiple local minima which pose a risk of incorrectly being identified as the best fit. In order to reduce the likelihood of this occurring each layer was fit four times, using four different starting parameter combinations. This would be the equivalent of starting on the left or right sides of the curves. The resultant best fits were then compared to see if they were all similar or if one had a

significantly lower RMSE. The lowest RMSE conditions were then fed into the next analysis stage.

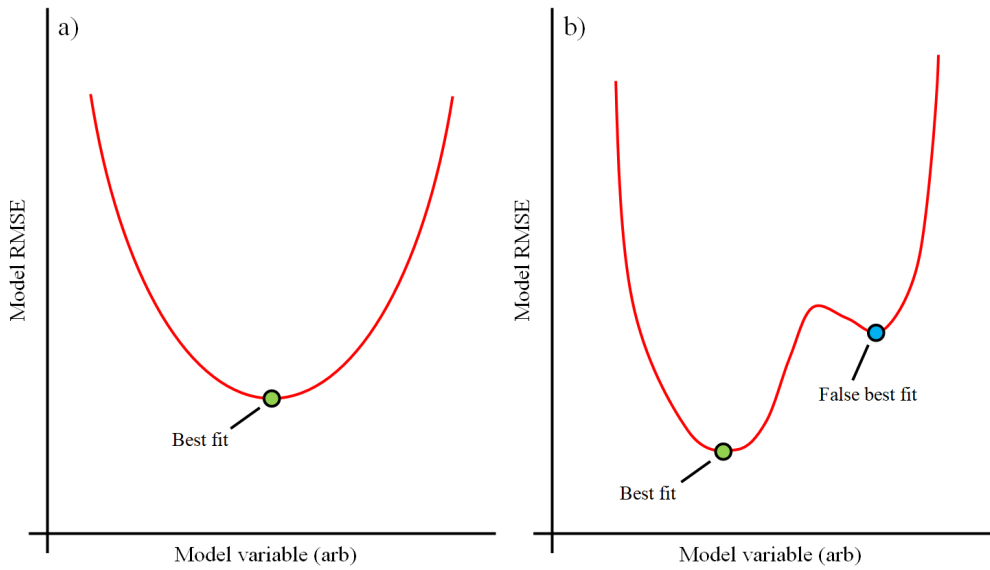


Figure 6.10: Illustration of a) ideal and b) realistic model errors.

In order to establish the reliability of the fits produced by the model another algorithm was used to assess the extent to which each model parameter could be changed whilst keeping the RMSE of the fit within 20% of the best value. This started with the best fit output from Figure 6.9 and used the same model equation (Eq. 6.4) but applied a different, more rigorous, logical flow to varying the model parameters. The flow of this algorithm is shown in Figure 6.12 and the accompanying UI shown in Figure 6.11. Broadly speaking the UI for this version is the same as the one shown in Figure 6.7 except that in Figure 6.11 the model output parameter boxes have been replaced with 15 different output boxes. These are 7 pairs of boxes which indicate the upper and lower limits for each variable (7<sup>th</sup> variable here being  $E_{off}$ , the difference between  $E_{Mob}$  and  $E_m$ ) and a box showing the minimum error found during the operation of the program. Two extra input boxes have also been added to the  $E_{Mob}$  parameter to indicate the full 50 meV range which this parameter can cover, as mentioned as part of the model constraints above.

The way this fitter works, shown in Figure 6.12, is that it takes a target error (exclusively set to 20% above the best fit in this work) and tests the limits of the model variables where the overall RMSE remains in the given range. This begins with the upper limit of a variable where each increase which produces a fit which remains below the target error causes the script to update the maximum passable variable for each variable. When the algorithm has found the boundary between passable and failed values it then switches to finding the minimum passable value for the variable. It was common for this algorithm to find even better fits than the previous model algorithm as, despite best efforts, the issue of local minima highlighted in Figure 6.10 still persisted. In this event these new best fits were tested manually and the model restarted with an updated starting point and target error. When this model finished for each layer, the final best fit with upper and lower limits for each model parameter were recorded for comparison across the series of layers which is discussed next in Section 7.



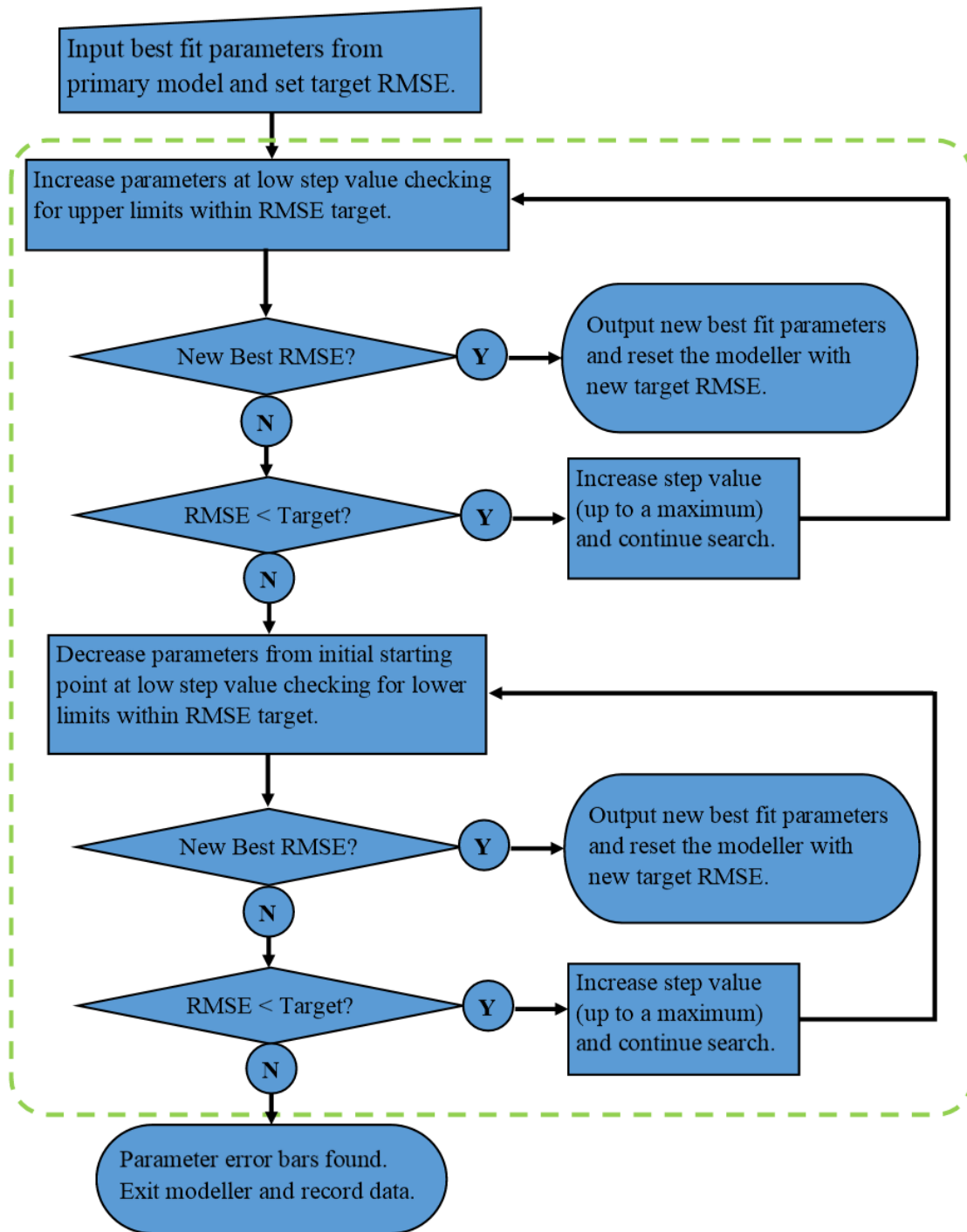


Figure 6.12: General flowchart of the error bar modeller. The multidimensionality of the code which simultaneously runs for each parameter is highlighted in a green dashed box, in the same way as in Figure 6.9.

## 7 RESULTS AND DISCUSSION

Figures 7.1 and 7.2 display the final fits for the growth temperature series and  $Bi$  flux series, respectively. The parameters used for these fits are shown in Table 7.1. Due to the low signal-to-noise ratio in several of the layers at 30  $mW$  excitation the fitting was only based on the data from 90 - 900  $mW$  for all the layers. Despite this, the resultant best fit has also been applied to the 30  $mW$  data here to further indicate the accuracy of the model.

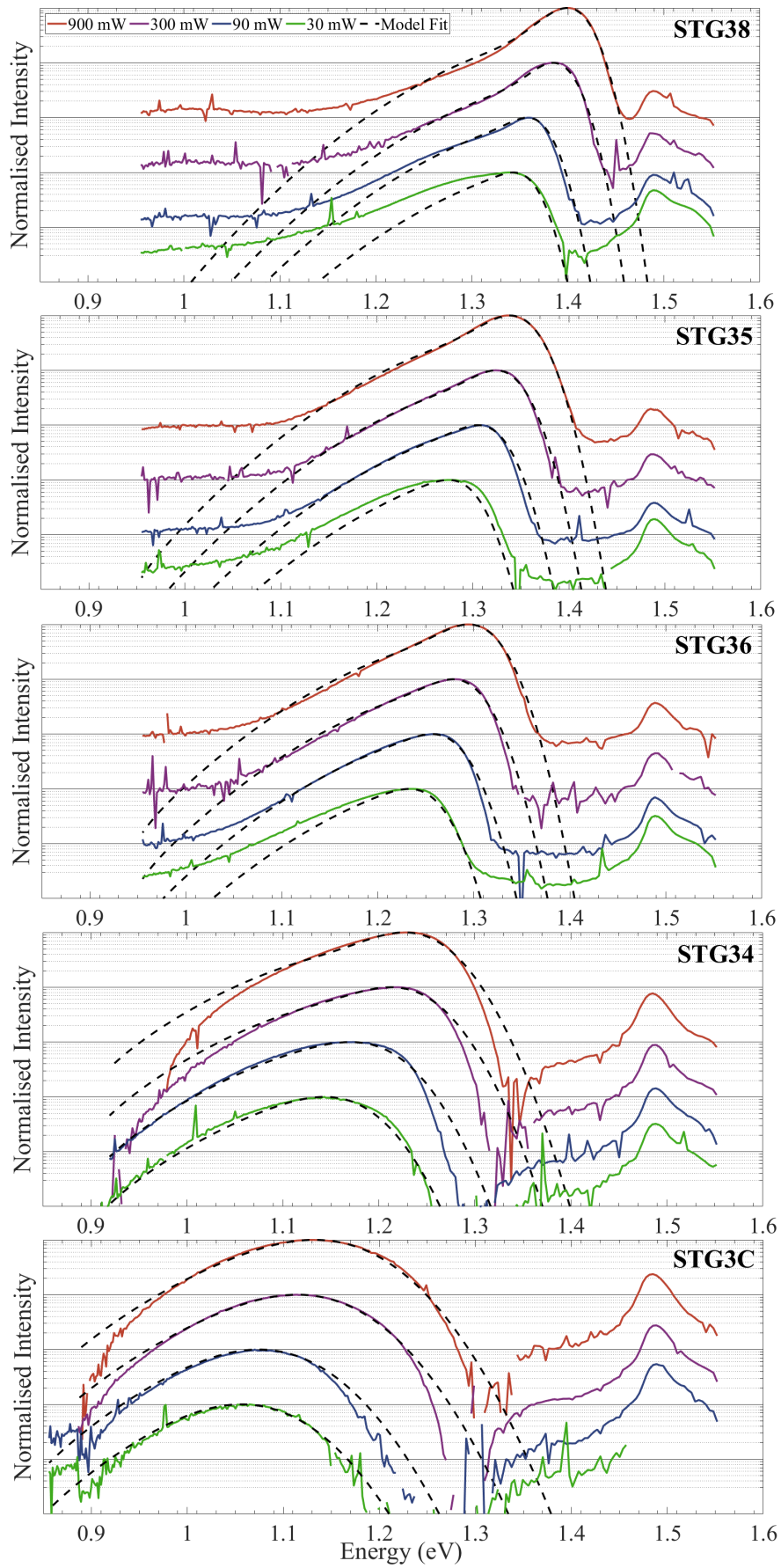


Figure 7.1: Model fits to PL for the growth temperature series.

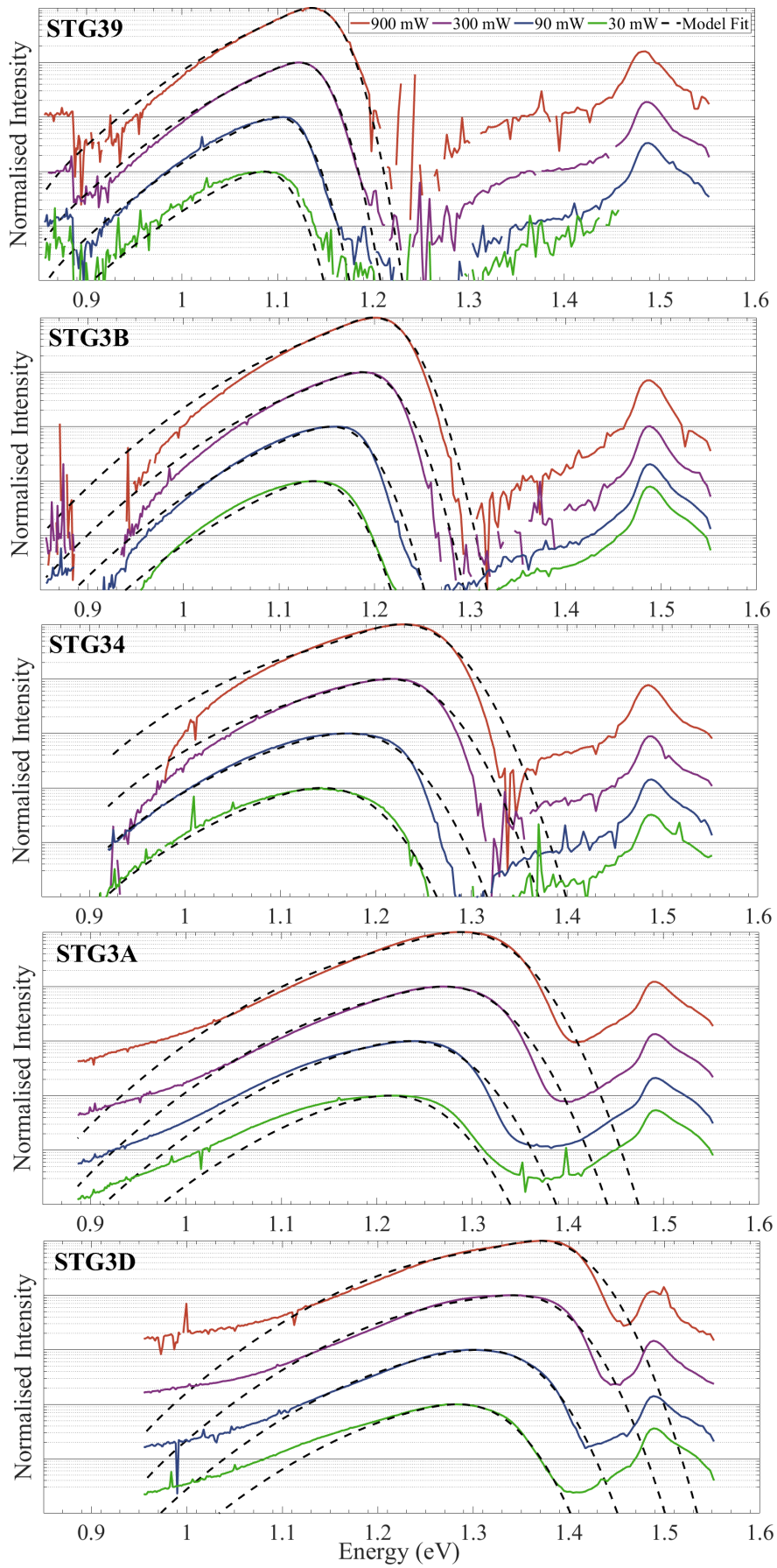


Figure 7.2: Model fits to PL for the Bi flux series.

Looking at Figures 7.1 and 7.2 it can be seen that the layers grown under the highest temperatures and  $Bi$  fluxes have the sharpest PL fall-off at high energy whereas the layers grown at lower temperatures/fluxes have broader emission. Of all the layers, STG3C had the highest localisation energies,  $E_{loc}$ , at all excitation powers. This is commensurate with low state filling and a short non-radiative lifetime which is expected to be due to a larger density of crystalline defects induced by the low growth temperature. This is supported by the large  $E_x$  value for this layer. The impact on the modelling from this low state filling is that even at the highest excitation power the localisation energy did not pass the crossover point between  $G_1$  and  $G_2$  (equivalent to energies  $\geq 1.27$  eV in Figure 6.6) and therefore the values for  $E_m$  and  $\gamma$  cannot be trusted. For this reason they have been enclosed in parentheses in Table 7.1.

It is noted that for STG38 there is a significant disparity between the experimental data and the model at 30 mW. It is believed that this difference originates from two distinct  $Bi$  compositions within this layer. This has already been discussed and highlighted in the original growth paper for these layers where it was shown that a two layer XRD model perfectly described both STG38 and STG35 [13].

Layer	$E_{Mob}$ (eV)	$E_m$ (eV)	$E_{offset}$ (eV)	$\sigma_1$ (eV)	$\sigma_2$ (eV)	$E_x$ (eV)	$\gamma$	$E_{Loc1}$ (eV)	$E_{Loc2}$ (eV)	$E_{Loc3}$ (eV)	$E_{Loc4}$ (eV)	RMSE
STG3C	1.276	(1.234)	0.042			0.046	(1)	0.099	0.12	0.166	0.185	0.0229
STG3C*	1.277	(1.215)	0.062			0.047	(0.11)	0.093	0.114	0.16	0.179	0.013
STG34	1.271	1.242	0.029			0.033	0.17	0.018	0.029	0.06	0.088	0.0343
STG34*	1.265	1.228	0.037	0.027	0.096	0.033	0.21	0.011	0.022	0.053	0.079	0.027
STG36	1.319	1.353	-0.034			0.02	0.43	0.001	0.018	0.039	0.061	0.0181
STG35	1.361	1.401	-0.040			0.018	0.4	0	0.017	0.035	0.062	0.0172
STG38	1.419	1.456	-0.037			0.015	0.26	0.001	0.018	0.044	0.056	0.0255
STG3D	1.422	1.351	0.071			0.031	0.18	0.024	0.041	0.068	0.096	0.0298
STG3A	1.330	1.303	0.027			0.035	0.28	0.011	0.025	0.055	0.077	0.0272
STG3B	1.242	1.274	-0.032			0.022	0.37	0.021	0.033	0.06	0.078	0.0273
STG3B*	1.242	1.266	-0.024	0.027	0.096	0.022	0.34	0.021	0.032	0.059	0.08	0.0259
STG39	1.172	1.25	-0.078			0.017	0.7	0.015	0.028	0.05	0.065	0.0209
STG39*	1.161	1.219	-0.058			0.019	0.52	0.004	0.018	0.039	0.056	0.0192

Table 7.1: Model parameters for the best fits to each of the STG3 series layers. Layers which had substrate PL removed (as shown in Figure 6.1) have been modelled twice with the fit to the uncorrected data being marked with an asterisk (\*). Values which are not considered trustworthy for layer STG3C due to limitations of the experimental data are enclosed in parentheses. Shaded columns indicate which parameters were fixed (red), restricted (orange) and which were unconstrained (green).

Figure 7.3 below shows the values for  $E_x$ ,  $\gamma$  and  $E_{offset}$  from Table 7.1 plotted against the  $Bi$  content extracted from XRD modelling for each layer. In Figure 7.3a it can be seen that increasing the growth temperature, and thereby reducing the  $Bi$  content, causes a significant reduction in  $E_x$ . In part this can be considered to be due

to the higher growth temperature reducing the defect density within the structure, but in comparison to the *Bi* flux series which was grown at a constant growth temperature it is clear that *Bi* also plays a role here. A similar trend is seen in Figure 7.3c although the relationship with *Bi* flux is linear and the impact of growth temperature saturates for temperatures  $\geq 385$  °C. In Figure 7.3b, however, where  $\gamma$  has been converted to an LDOS ratio ( $\frac{1-\gamma}{\gamma}$ ) there is no distinct trend.

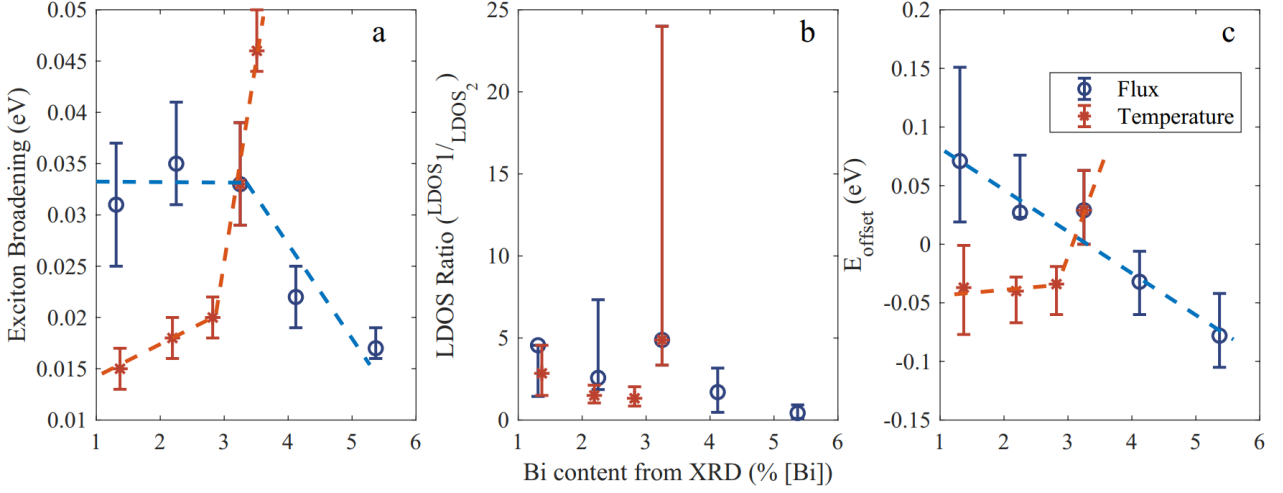


Figure 7.3: Trends in the a) exciton broadening, b) LDOS ratio and c)  $E_{offset}$  plotted against the *Bi* content from XRD for each layer. Note data for STG3C is omitted from b) and c) as the relevant parameters are not considered reliable.

In the current format the variables displayed in Figure 7.3 do not really provide a definitive conclusion on the effect of these growth conditions on the localised states. It is already generally known that growth at higher substrate temperatures are favourable [13, 14] and *Bi* had much use as a surfactant in III-V growth before its application to dilute bismide semiconductors. Therefore, in order to map these two series to a different, shared growth parameter other than the *Bi* content a new value was based on their growth conditions.

This value is referred to as the '*Bi* coverage' but it should be promptly noted that this is only a rough analogue for the true *Bi* surface coverage as the value calculated here comes from the division of the *Bi* BEP supplied by the *Bi* content extracted from XRD modelling (Eq 7.1) and does not attempt to take into account the actual impinging *Bi* flux (measured in  $atoms\,cm^{-2}\,s^{-1}$ ) or the surface desorption of *Bi* adatoms or other important factors. This value is **not** analogous to the *Bi* coverages used in the growth models discussed in Section 2.7.1. Nevertheless, this value does give a good first order approximation of the relative proportion of supplied *Bi* not incorporated into the semiconductor lattice and which is likely to be accumulated on the crystal surface.

$$Bi\,coverage = \frac{Bi\,BEP (\times 10^{-7}\,mbar)}{Bi\,content (\%)} \quad (7.1)$$

The *Bi* coverage could be considered to be controlled by one of two means in the context of the STG3 series. The first is by increasing the growth temperature which would in turn reduce the solubility of *Bi* in *GaAs* thereby reducing the *Bi* content of the layer and increasing the proportion of *Bi* on the surface. The other possibility is to increase the *Bi* flux, this will increase the *Bi* content of the layer, coming closer to the solubility

limit and also increase the proportion of  $Bi$  which is segregated on the surface. Using the  $Bi$  coverage values to replot the parameters from Figure 7.3 results in Figure 7.4.

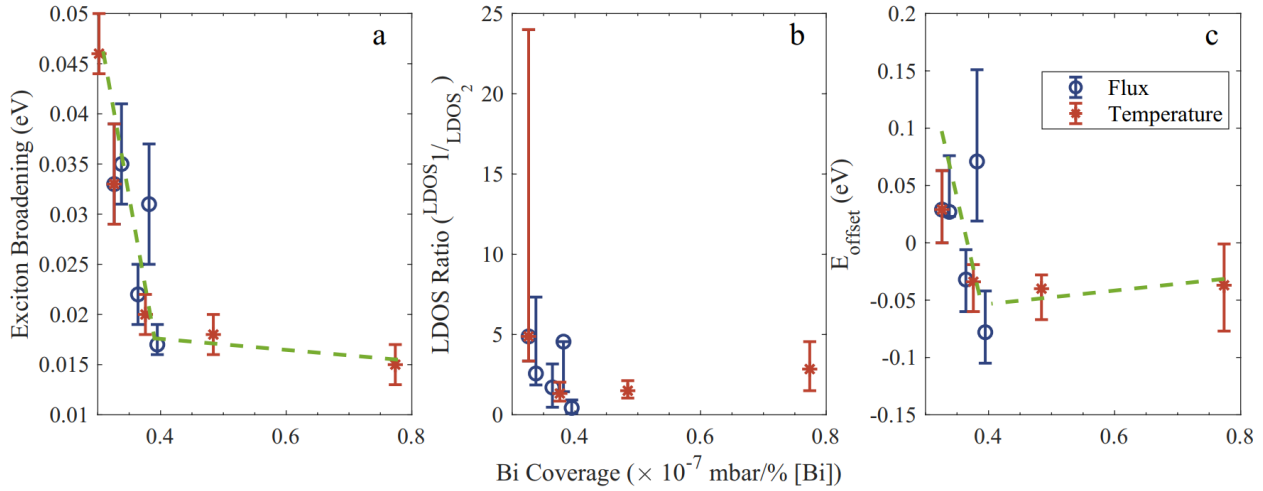


Figure 7.4: Trends in the a) exciton broadening, b) LDOS ratio and c)  $E_{offset}$  plotted against the estimated  $Bi$  coverage for each layer. It can immediately be seen that the disparate trends seen in Figure 7.3a and 7.3b are now completely complementary.

It is clear to see that the previously disparate trends from Figure 7.3 are almost completely reconciled in Figure 7.4. At the lowest  $Bi$  coverages, which indicates a high proportion of the supplied  $Bi$  is incorporated (often referred to as the  $Bi$  flux limited regime), the layers have large  $E_x$  values and  $E_{offset}$  is positive which places the peak of  $G_2$ , the distribution representing cluster states, within the band gap. As the  $Bi$  coverage increases  $E_x$  and  $E_{offset}$  rapidly decrease which results in sharper PL and the majority of the  $Bi$  cluster states,  $G_2$ , being located within the valance band, effectively suppressing them. Whilst this implies that a high  $Bi$  coverage is desirable, it should not be forgotten that this parameter still indicates the volume of  $Bi$  present on the surface and if this exceeds a critical point  $Bi$  droplets will nucleate which will then negatively impact the material quality. It is expected that the reason for this not occurring in these layers is that the grown thickness is very thin (100 nm). Therefore for thicker  $GaAsBi$  depositions one would be better advised to aim for a  $Bi$  coverage equivalent to the ‘knee’ in Figure 7.4 ( $\sim 0.4$ ) where the effect of increasing  $Bi$  coverage begins to saturate.

The importance of this final Figure is that, despite being produced from varied growth conditions, this model reconciled these layers into one of two growth regimes. It has been generally noted that better, device-quality  $GaAsBi$  material comes from growth at higher temperatures [13, 14] which can be referred to as the temperature limited regime. On Figure 7.4 this would be the low gradient lines at higher  $Bi$  coverages. The other common regime,  $Bi$  flux limited, would therefore be the sharp gradient at low  $Bi$  coverages. By being able to estimate which regime one is growing with by performing this modelling technique, two things are apparent. The first is that  $GaAsBi$  device growth could be optimised without the need to fabricate many different wafers and measure dark currents etc. and the second is, for a target  $Bi$  content, the output of this model will direct the direction of growth optimisation. For example, if the  $Bi$  content is too high and the model outputs values suggesting growth is at the far end of the temperature limited regime, then the growth temperature should

come down slightly to segregate less *Bi* and incorporate more.

## 8 CONCLUSIONS

In summary a previous literature model for low-temperature photo-luminescence of gallium arsenide bismide has been adapted through the modification of the localised state profile. The efficient implementation of this model along with reasoned argument for several parameter constraints has also been discussed. Its functionality over a wide range of growth condition has been demonstrated through reliable fitting to spectra from a series of gallium arsenide bismide layers. From the best fit parameters it has been shown that both higher growth temperatures and bismuth fluxes reduce the exciton broadening parameter. This reduction in the exciton broadening implies an improvement in the crystal quality under these conditions. By comparing the two sub-series using a parameter which estimates the amount of bismuth segregated to the surface, the trends between them show significant convergence. When the bismuth coverage value is large the exciton broadening is reduced and the peak density of the broad localised distribution,  $g_2$ , is shifted within the valence band. This improvement in material quality and suppression of localised states is attributed to the surfactant effect of the bismuth occupying the surface. As discussed earlier, in order to optimise the quality of grown material and prevent bismuth droplets forming during thick epilayer growth, the excess bismuth should be tuned to the pivotal ‘knee’ point in Figure 7.4 after which no significant improvement is seen.

## REFERENCES

- [1] A. Mohmad, F. Bastiman, J. Ng, S. Sweeney, and J. David, “Photoluminescence investigation of high quality  $GaAs_{1-x}Bi_x$  on GaAs,” *Applied Physics Letters*, vol. 98, no. 12, p. 122107, 2011.
- [2] R. Kudrawiec, M. Syperek, P. Poloczek, J. Misiewicz, R. Mari, M. Shafi, M. Henini, Y. G. Gobato, S. Novikov, J. Ibanez, *et al.*, “Carrier localization in GaBiAs probed by photomodulated transmittance and photoluminescence,” *Journal of Applied Physics*, vol. 106, no. 2, p. 023518, 2009.
- [3] S. Tixier, M. Adamcyk, T. Tiedje, S. Francoeur, A. Mascarenhas, P. Wei, and F. Schiettekatte, “Molecular beam epitaxy growth of  $GaAs_{1-x}Bi_x$ ,” *Applied physics letters*, vol. 82, no. 14, pp. 2245–2247, 2003.
- [4] F. Bastiman, A. Mohmad, J. Ng, J. David, and S. Sweeney, “Non-stoichiometric  $GaAsBi/GaAs$  (100) molecular beam epitaxy growth,” *Journal of crystal growth*, vol. 338, no. 1, pp. 57–61, 2012.
- [5] A. R. Mohmad, F. Bastiman, C. Hunter, R. Richards, S. Sweeney, J. Ng, J. David, and B. Y. Majlis, “Localization effects and band gap of  $GaAsBi$  alloys,” *physica status solidi (b)*, vol. 251, no. 6, pp. 1276–1281, 2014.
- [6] M. Yoshimoto, M. Itoh, Y. Tominaga, and K. Oe, “Quantitative estimation of density of  $Bi$ -induced localized states in  $GaAs_{1-x}Bi_x$  grown by molecular beam epitaxy,” *Journal of crystal growth*, vol. 378, pp. 73–76, 2013.
- [7] R. D. Richards, C. J. Hunter, F. Bastiman, A. R. Mohmad, and J. P. R. David, “Telecommunication wavelength  $GaAsBi$  light emitting diodes,” *IET Optoelectronics*, vol. 10, no. 2, pp. 34–38, 2016.
- [8] S. Imhof, A. Thränhardt, A. Chernikov, M. Koch, N. S. Köster, K. Kolata, S. Chatterjee, S. W. Koch, X. Lu, S. R. Johnson, *et al.*, “Clustering effects in  $Ga(AsBi)$ ,” *Applied Physics Letters*, vol. 96, no. 13, p. 131115, 2010.
- [9] V. Valkovskii, K. Jandieri, F. Gebhard, and S. Baranovskii, “Rethinking the theoretical description of photoluminescence in compound semiconductors,” *Journal of Applied Physics*, vol. 123, no. 5, p. 055703, 2018.
- [10] C. Gogineni, N. A. Riordan, S. R. Johnson, X. Lu, and T. Tiedje, “Disorder and the Urbach edge in dilute bismide  $GaAsBi$ ,” *Applied Physics Letters*, vol. 103, no. 4, p. 041110, 2013.
- [11] M. Shakfa, M. Wiemer, P. Ludewig, K. Jandieri, K. Volz, W. Stolz, S. Baranovskii, and M. Koch, “Thermal quenching of photoluminescence in  $Ga(AsBi)$ ,” *Journal of Applied Physics*, vol. 117, no. 2, p. 025709, 2015.
- [12] T. Wilson, N. P. Hylton, Y. Harada, P. Pearce, D. Alonso-Álvarez, A. Mellor, R. D. Richards, J. P. David, and N. J. Ekins-Daukes, “Assessing the nature of the distribution of localised states in bulk  $GaAsBi$ ,” *Scientific reports*, vol. 8, no. 1, pp. 1–10, 2018.
- [13] T. Rockett, R. Richards, Y. Gu, F. Harun, Y. Liu, Z. Zhou, and J. David, “Influence of growth conditions on the structural and opto-electronic quality of  $GaAsBi$ ,” *Journal of Crystal Growth*, vol. 477, pp. 139–143, 2017.

- [14] K. Kakuyama, S. Hasegawa, H. Nishinaka, and M. Yoshimoto, “Impact of a small change in growth temperature on the tail states of *GaAsBi*,” *Journal of Applied Physics*, vol. 126, no. 4, p. 045702, 2019.
- [15] F. Urbach, “The long-wavelength edge of photographic sensitivity and of the electronic absorption of solids,” *Physical Review*, vol. 92, no. 5, p. 1324, 1953.
- [16] A. Mohmad, B. Majlis, F. Bastiman, C. Hunter, R. Richards, J. Ng, and J. David, *Photoluminescence from localized states in GaAsBi epilayers*.
- [17] N. Bailey, T. Rockett, S. Flores, D. Reyes, J. David, and R. Richards, “Effect of MBE growth conditions on *GaAsBi* photoluminescence lineshape and localised state filling,” *Scientific reports*, vol. 12, no. 1, pp. 1–8, 2022.

## PART III

# *InAs*(*Bi*) QUANTUM DOT GROWTH

## 9 LITERATURE REVIEW

Quantum dots (QDs) were first proposed in 1982 in a literature report by Yasuhiko Arakawa and Hiroyuki Sakaki [1]. The discussed benefits of such a band structure were the complete removal of temperature dependence of the threshold current in lasing devices.

Since this early discussion of three-dimensional confinement there has been much research undertaken to synthesise QDs, characterise them and exploit their properties in electronic devices. The primary material in this research field is *InAs*. This is due to the ease of which it they can be induced to self-nucleate via SK growth on a mismatched substrate as discussed in Section 2.5.1. Another useful property is their low band gap which sits in an ideal range for near-infrared (NIR) and mid-infrared (MIR) applications depending on the substrate used. In Section 2.5.1 it was also mentioned that there have been various growth techniques studied in order to develop well understood methods to reliably control the shape and size of *InAs* QDs so their unique properties can be exploited in electronic devices. This chapter will focus on one particular method, the use of *Bi* during QD growth on *GaAs* substrates.

Before discussing reports of *Bi* use in regard to QD growth, it is prudent to first give an overview of the literature coverage on the use of *Sb*. *Sb* can be used as a surfactant or also be alloyed into semiconductors in the same way as *Bi*. There are multiple reports covering its use as a surfactant during different stages of QD growth [2, 3, 4] and also as a QD capping layer material (*GaAsSb*) [5, 6, 7]. In *GaAsSb* capping experiments, large red shifts in QD emission have been identified [5, 6]. When deposited in a pre-growth layer *Sb* increases the QD density [8], but when used as a surfactant during QD growth, *Sb* induces a blue shift in emission which was attributed to reduced QD size [2] and an increase in the Stranski-Krastinov critical thickness [3].

Reports of the use of *Bi* as a surfactant during *InAs* QD growth present a reduction in the QD density [9, 10, 11] and, in contrast to *Sb*, has been shown to increase QD height [9, 10, 11, 12]. However, the effects of *Bi* are not straightforward. In a report by Dasika et al. [12] it was found that for *InAs* depositions of  $\leq 2.3$  ML *Bi* lead to a reduction in QD density but for depositions of  $\geq 2.6$  ML the use of *Bi* increased QD density as well as reducing the density of dislocated *InAs* islands. In a study looking at the effect of varying the growth temperature Chen et al. [13] found that in the growth temperature range of 475 – 492 °C *Bi* reduced the density of QDs but for temperatures of 492 – 500 °C it increased QD density. It was also noted that the QD uniformity improved and the island density was reduced.

Returning to the consideration of capping materials, *GaAsBi* exhibits a large reduction in band gap per % *Bi* in *GaAs* [14], making it a promising material for QD capping layers. Wang et al. [15] studied the effect of *Bi* as a surfactant and constituent in the barrier and capping layers. They found that a 5 % *GaAsBi* buffer reduced both the height and density of subsequent QDs when compared to *GaAs*. This was interpreted to indicate a

delay in *InAs* QD nucleation caused by *Bi* segregation at the increased substrate temperature of 500 °C for QD growth. When used in a capping layer grown at 280 °C, 3 % *Bi* induced a significant red-shift of 163 *meV* in the emission wavelength. When the capping layer was grown at 500 °C, thereby segregating all the supplied *Bi*, it was found to mitigate density loss during capping and improve QD uniformity.

From all the literature coverage, one of the effects of *Bi* on QD nucleation which remains contested is its impact on *In* surface diffusion. There has been evidence to support a *Bi* induced increase [9, 10, 16] but also a decrease [12, 13, 15, 17].

The aim of this chapter was to push the boundaries of *Bi* flux, which had only been lightly compared in the literature, and further explore the fundamental impact of *Bi* on *InAs*. This was done through the study of two QD series grown at temperatures of 380 or 580 °C using one of four *Bi* fluxes. The experimental analysis covers PL and AFM characterisation of the layers personally grown for this work. It should be acknowledged here, along with thanks, that the recording of the AFM data was performed by the Sheffield Surface Analysis Centre (SSAC).

## 10 GROWTH AND ANALYSIS

### 10.1 LAYER GROWTH

The structure of the QD layers is shown in Figure 10.1 and a summary of the growth conditions which were varied throughout the series is shown in Table 10.1. These layers were grown in the MBE-STM system detailed in Section 3 on semi-insulating *GaAs* (001) substrates, in random order to prevent any chronological reactor variation affecting the results. After thermally desorbing the native oxide at 620 °C under an *As<sub>2</sub>* flux a 300 *nm GaAs* buffer was deposited at 580 °C. Next the substrate was cooled to either 380 or 510 °C and the first set of QDs were produced by depositing 2.2 *ML* of *InAs* under an *As<sub>4</sub>* flux. An additional *Bi* flux was also supplied during QD nucleation, the equivalent BEP of this flux varied between growths and is detailed in Table 10.1. After this a 60 *nm* thick *GaAs* buffer was deposited, to allow for optical studies on the buried layer and an identical layer of QDs deposited for surface studies. The thickness of the *GaAs* buffer was chosen such that there would be no strain coupling between the two QD layers [18]. The *InAs* growth rate was calibrated by RHEED observation of the critical thickness for QD formation ( $\sim 1.6$  *ML*) [19] and the *GaAs* growth rate was calibrated through the observation of RHEED oscillations for the first minute of growth. Unfortunately, due to poor RHEED screen condition no conclusive images or observations could be recorded during this growth campaign beyond these calibrations. The *As:III* ratios quoted in Figure 10.1 are atomic flux ratios and were calibrated at the *GaAs* growth rate.

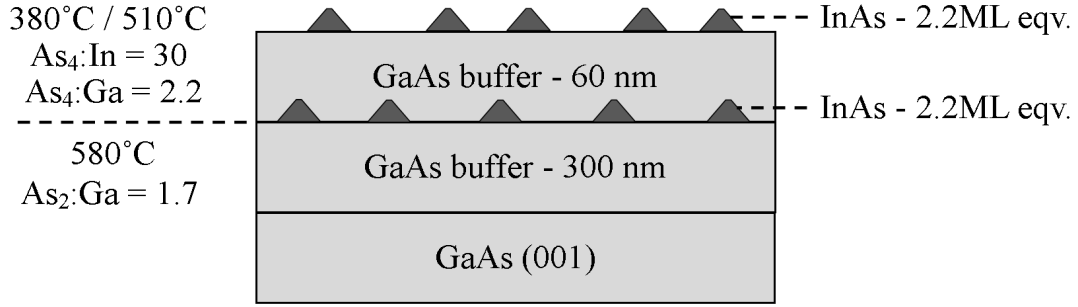


Figure 10.1: Structure of the QD layers. The buried QD layer was produced for optical analysis and the surface layer grown for QD surface morphology study. The cap layer was grown to be sufficiently thick to prevent strain coupling between the two QD layers [18].

Layer	Growth Temperature (°C)	Bismuth BEP ( $10^{-7} mbar$ )
L0	380	0
L1	380	1.2 (L)
L2	380	2 (M)
L3	380	2.7 (H)
H0	510	0
H1	510	1.2 (L)
H2	510	2 (M)
H3	510	2.7 (H)

Table 10.1: QD series growth conditions. The varied Bi BEPs were applied at one of two growth temperatures to allow independent comparisons between growth temperature and Bi BEP.

The recipe used here to produce these QDs is acknowledged to not be state-of-the-art. There are numerous literature reports on the use of various techniques including low As fluxes [20], growth interrupts [21] and strain effects [22] to achieve QDs with narrow line-widths and high/low densities for specific applications. This was not considered useful for a fundamental study such as this for two reasons.

The first is that before the main growth campaign there will have been a lengthy optimisation period, the conditions for which would be thrown off calibration by the addition of a Bi flux, obscuring the isolated effects of the Bi flux. It would therefore be expected that the growth conditions would need to be re-optimised around each Bi BEP which would complicate the analysis of the series.

The second reason is that if the various QD properties (emission line-width, QD density etc.) are already close to record, or indeed even the physical, limits of what is possible, then the impact of the Bi flux will be muted

when it should be regarded as an alternative technique and not solely one which must be used in conjunction with others. With this rationale laid out, it is expected the less than optimal properties of the control layers, L0 and H0 which were grown without a *Bi* flux, can be viewed with an open mind.

## 10.2 AFM ANALYSIS

Samples of each of the QD layers were analysed by AFM at multiple points. This yielded high quality images for each layer covering an area of 3 - 4  $\mu\text{m}^2$ . The tip used for these measurements was nominally 7 nm wide and was used to measure all the layers. As mentioned in Section 4.5, due to the finite width of the tip the images recorded are actually a convolution of the surface with the tip. This can be corrected for but it was decided to analyse the raw AFM data instead as the morphology statistics of surface QDs already differs from the buried QDs due to intermixing processes which occur during overgrowth. Given the large width of the QDs relative to the tip, the effects of tip convolution were not expected to the analysis performed here. The overall purpose of the AFM analysis was not only to extract traditional QD metrics including height, surface density and size distribution, but also examine more subtle changes which may be introduced through the use of *Bi*. These include the shape and total volume of the QDs.

Initially analysis of these images was attempted using Bruker Nanoscope Analysis. This software offered a variety of tools including particle detection, plane fitting and 3D imaging of the surface. It was found, however, to be lacking in some finer functions required to reliably compare the characteristics of quantum dots from the different layers. Two of the main issues are highlighted in Figure 10.2. The first is the omission of small QDs ( $< 3\text{ nm}$ ) which formed as part of a bimodal distribution in some of the layers. These particles have been confirmed to be QDs from their consistent formation and matching morphology compared to the larger dots, and their omission would significantly impact dot density and height distribution comparisons of the layers and therefore could not be ignored. The other issue occurs when trying to add these dots to the detected selection by adjusting the scan settings for the minimum dot height, here two or more of the larger QDs which were in close proximity to each other were assumed to be a single particle. Whilst this would have a minimal impact on the dot density which could be manually accounted for it does introduce significant and false outliers to area/volume distributions which were calculated by the software. Most importantly it can be seen in Figure 10.2b that even after reducing the peak height settings the background dots are still not correctly identified.

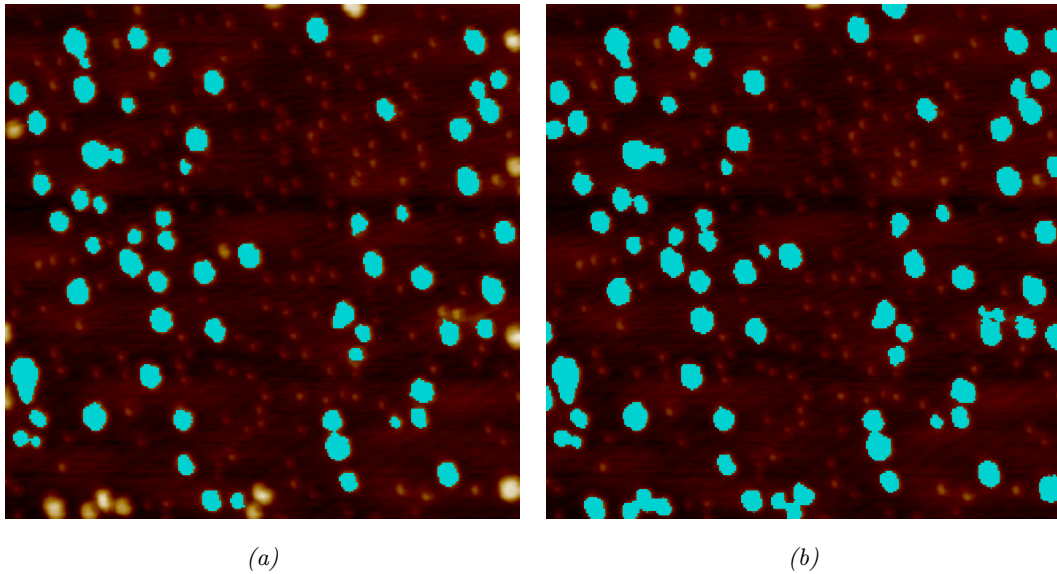


*Figure 10.2: Map of detected particles for layer L3 a) without and b) with boundary particles included. In both images it can be seen that small QDs ( $< 3\text{ nm}$ ) are not detected.*

Another failure of the software which may not be an issue for other AFM applications, but is of key interest for QD analysis, is how the morphology data is presented. Height, area and volume distributions etc. could only be exported as anonymous x-y sequences of the bins and probabilities. This meant it was not possible to investigate linked trends of QD height and area etc. as no single QD could be individually inspected. As there was no way to circumvent these issues within the Nanoscope software, it was decided to export the surface data in an ASCII format and perform all post processing of particle characteristics using a custom-made software suite in MATLAB. The aim of this software was to record the surface statistics in a more specialised way which was appropriate to QD layers. For example, by maintaining the association of various characteristics to individual dots, relationships between different traits such as height and width could be investigated rather than simply producing histograms of each.

The production of this software involved writing a user interface to aid in identifying and extracting the QD populations and writing several background functions for processing the AFM images. These are listed below with a description of their functionality:

1. Peak identification - A brute force checker which finds the highest point in the image and compares it to minimum height supplied for a QD. If the highest point in the image passes this check it is passed to the 'Peak contouring' function.
2. Peak contouring - This takes a peak value, near the centre of the QD from a birds-eye perspective. It then navigates to the QD base boundary as dictated by user input and then maps out peak area as a contour. It does this by deliberately crossing the boundary condition as it progressively moves clockwise around the dot area. After identifying an outline for the QD it is then filled in column by column with the morphology data of the QD.
3. Peak removal - Using the filled QD contour data the peak is removed from the starting array. This means this current QD will not be identified in the next 'Peak identification' step.

4. Particle loop - This function runs the previous three in order to log QDs in descending height order from the initial data array. It stores important QD characteristics within an ordered matrix for later surface analysis and plots an overlaid contour of all the identified QDs with the leftover array which enables the user to identify if any dots have been missed by the software.
5. Particle Correction - Here the MATLAB software that was written in this work moves beyond the Nanoscope software and allows the user to inspect each identified QD in order and perform various corrections for noise, QD amalgamation and any errors introduced by the software. It also offers quick 3D viewing of QDs. In order to automatically remove particles which are entirely noise based, the user can set the tip size (relative to the units of the scan) and any identified particles which are smaller than the tip are removed as they are detected.

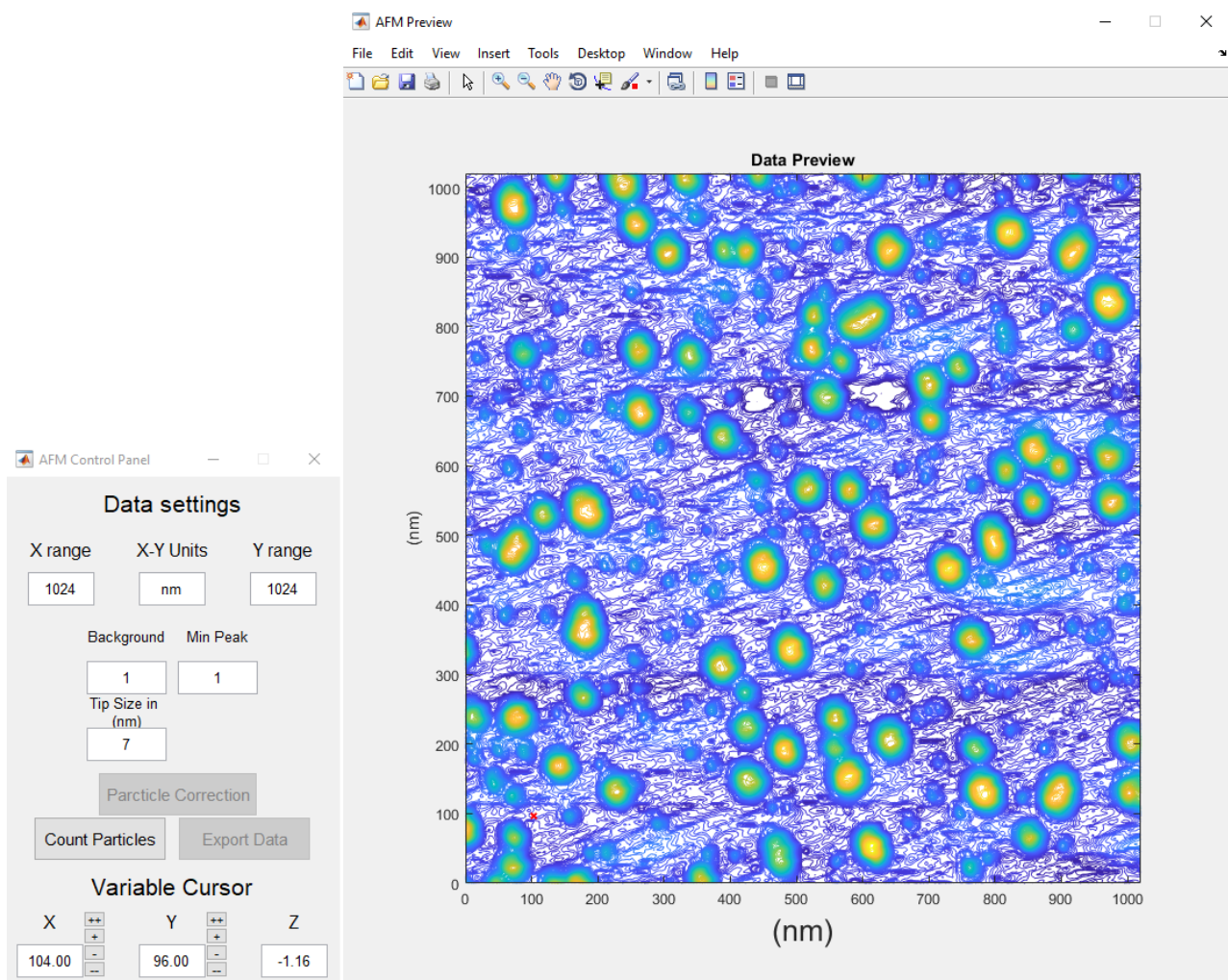
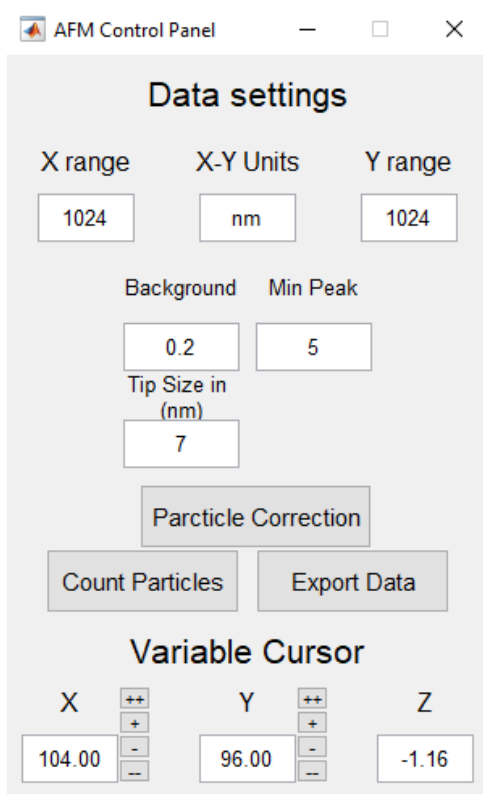


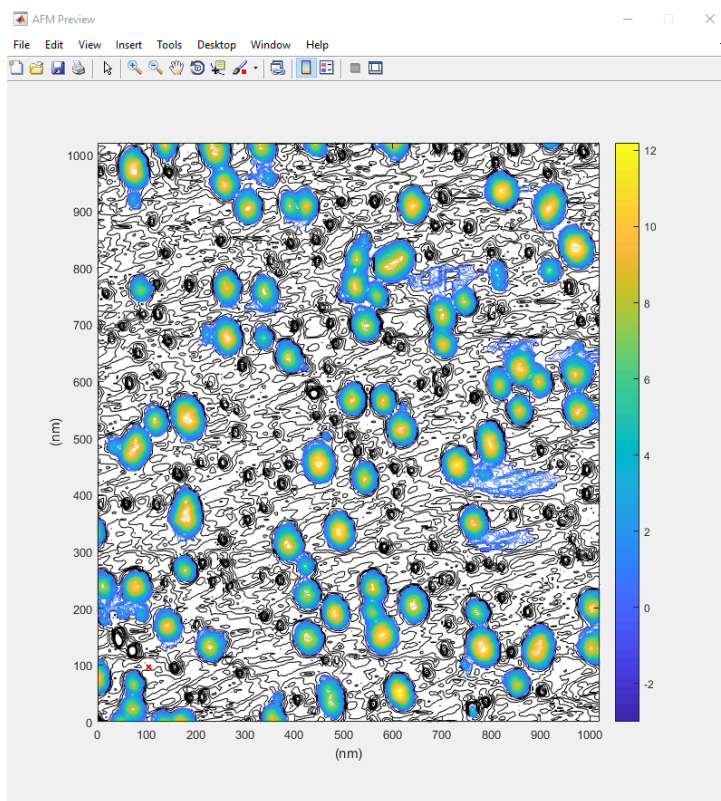
Figure 10.3: User interface for MATLAB particle detection software. This shows the initial state of the software before any processing has been run. In the 'Data settings' window, the boxes at the top labelled X/Y range and X-Y units are used to set the area covered by the image, this is used for the volume and area calculations. The background, min peak and tip size boxes are used to other conditions which are used in QD particle detection. The 'Variable cursor' boxes at the bottom are used to move the cursor, a red 'X' seen in the bottom left of the 'AFM preview' window, and provide feedback on the image height at the current location for choosing appropriate settings for each image.

Figure 10.3 shows the start page displayed upon first running the software with an AFM data set. The control panel on the left allows the user to set the values for background noise and the minimum height for a peak to be identified. To aid with this the 'Variable Cursor' boxes allow the inspection of the height at different points in the image by moving the red cross, bottom left of preview window on the right side, to user defined coordinates and outputting the corresponding height. Once a user is happy with the provided settings, clicking 'Count Particles' will start the detection function which will sequentially identify and separate the QDs in the image. When this is complete, the 'Particle Correction' and 'Export Data' boxes are enabled for further processing or saving of data.

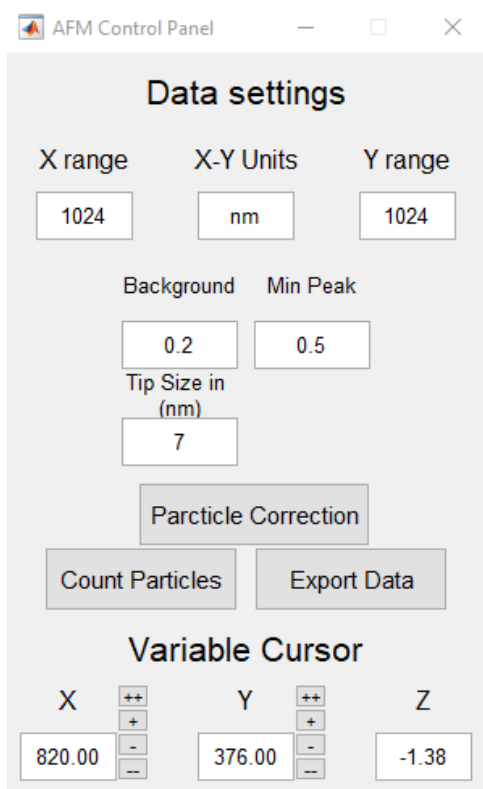
The effect on the way the background and minimum peak settings effect the automatic detection of the QDs is shown in Figure 10.4. It can be seen in Figure 10.4b that a large number of the smaller QDs, visible due to their tight concentric shape on the contour plot, have been omitted in the initial search and are not coloured. By reducing the minimum peak height nearly all of these short QDs are now identified. Where there are any remaining undetected dots the cursor can me moved to their position in order to check their peak height and fine tune the settings.



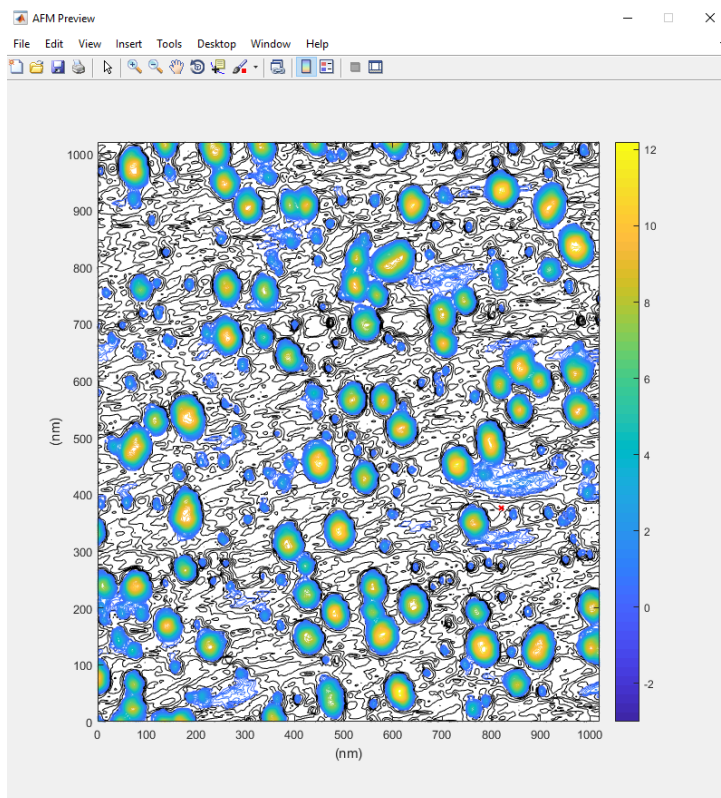
(a)



(b)



(c)



(d)

Figure 10.4: Comparison of detection settings on map of detected particles. The settings, a), and associated preview, b), which only detects most of the quantum dots. c) and d) show the settings and preview, respectively, of a scan which detects all of the quantum dots from an AFM scan. Areas of the image identified to include QDs are coloured, and the background of the image is black.

It can be seen in both Figures 10.4b and 10.4d that there for some identified QDs a considerable area of the background has also been included. This is corrected in the particle correction window which is opened from the control panel. The particle correction window, shown in Figure 10.5 displays a single particle at a time in descending height order. From this window, specific values calculated for each particle can be seen and there are options to view the particle in 3D, shown in Figure 10.6, remove it from the series in the case of noise artefacts or split a particle in two, as is needed for QDs in close proximity to each other, which have been identified as a single particle.

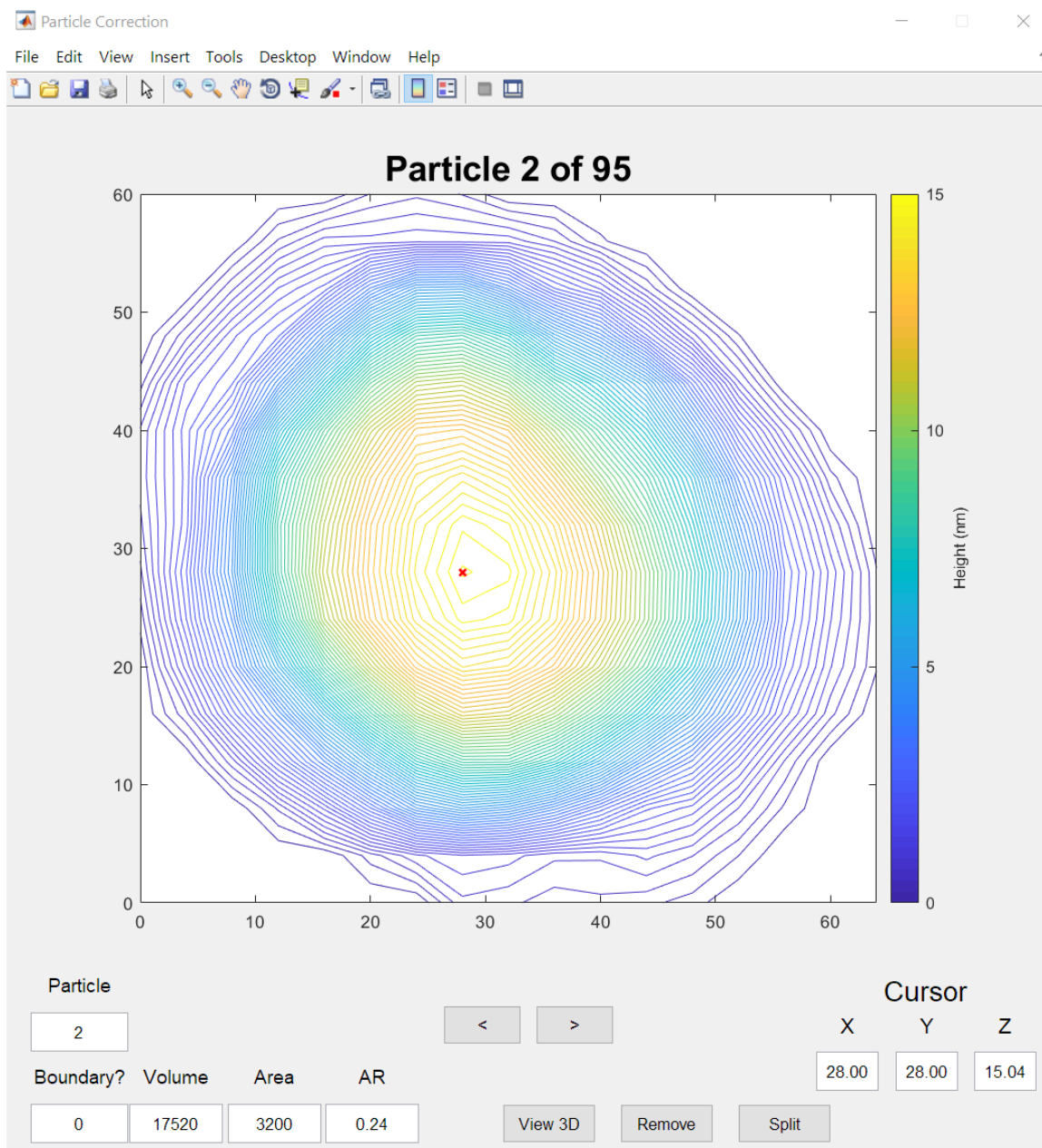
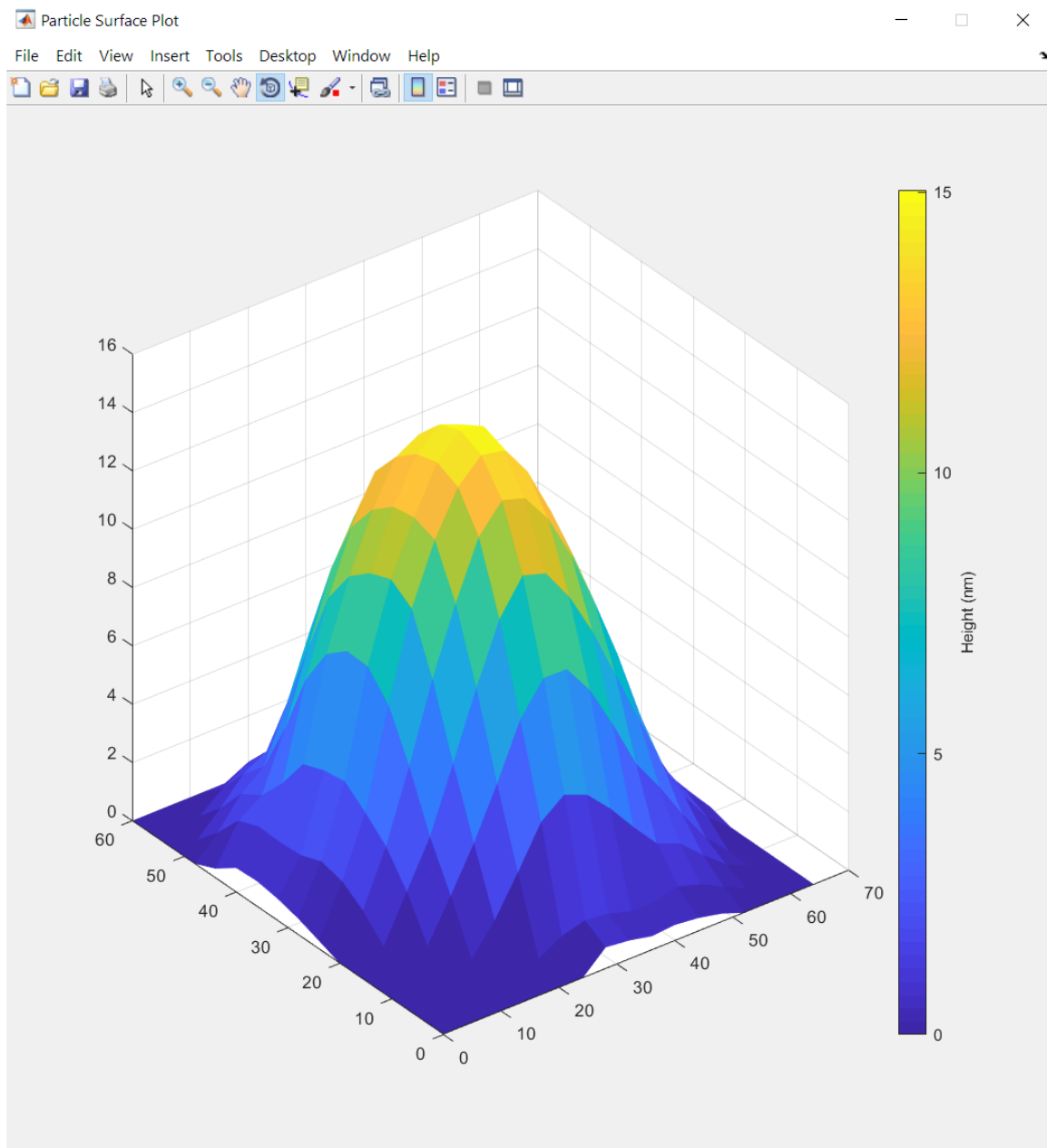


Figure 10.5: AFM UI particle correction window. Allows closer inspection of all identified QDs with options to split or discard particles.



*Figure 10.6: AFM UI particle correction 3D viewer for inspecting particles.*

An example of these twinned QDs is shown in Figure 10.7. By selecting an appropriate contour height to split these two particles as evenly as possible they can then be replaced in the the result file. It can be seen that there is still leftover data in particle 2 which can be removed in another round of particle splitting where only particle 1 is kept and the background is discarded.

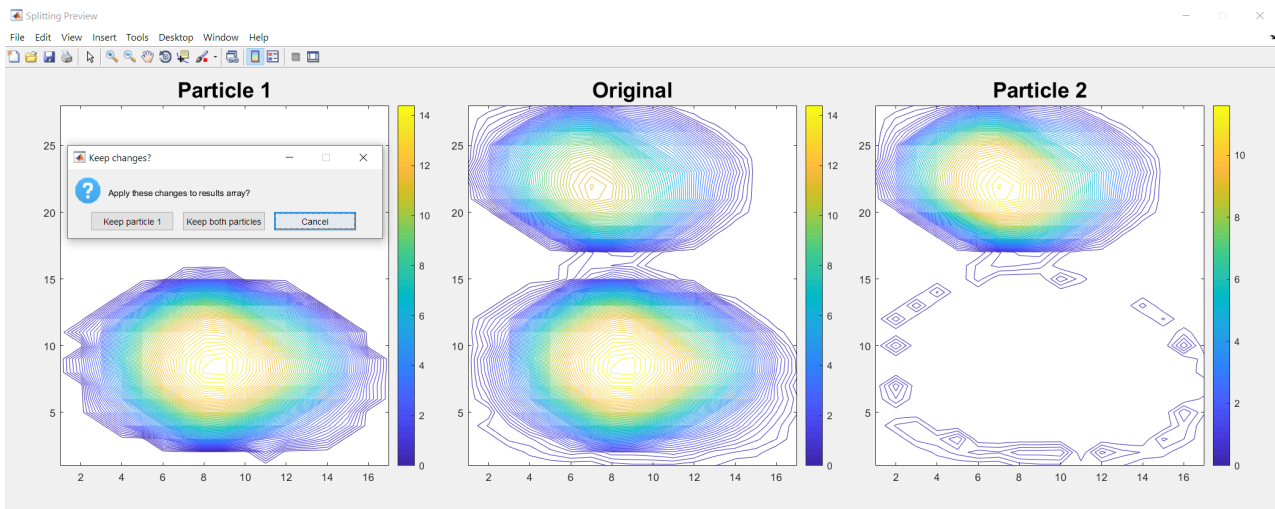


Figure 10.7: Particle splitting confirmation screen. Allows the inspection of the two split particles before any data is written to the result file. There are options to keep only particle 1, keep both particles or cancel the operation, which is useful for optimising the splitting process through trial and error.

In summary, whilst the various processes performed by this script appear complex with many variables, most of this is actually automatic without much need for user input. The few steps which require user calibration are as follows:

1. Load the data into the script and set the **X-range**, **Y-range**, **Units** and **Tip size**.
2. Choose a **Min Peak** for which a QD will need to be taller than to be processed.
3. Run the script using the **Count Particles** button and check to see that all visible QDs are highlighted. If not, repeat the previous step with a lower **Min Peak**.
4. Once all the QDs have been identified, check through the data in the **Particle Correction** window.
5. If in this window any QDs need splitting or separating from the background, select an appropriate height by which to split them and discard any background noise.
6. Export the data to a .csv file when finished.

Following these steps the AFM scans for each of the layers were processed and summed into a single QD population for each layer.

### 10.3 PL ANALYSIS

Optical characterisation of the layers was performed at room temperature using the PL setup at laser excitation powers of 90 - 900 *mW*.

## 11 RESULTS AND DISCUSSION

### 11.1 AFM RESULTS

A raw AFM image for each layer is shown in Figure 11.1. First of note is the lack of significant QD formation in layer L0 where only a few short precursor QDs can be seen within the rough wetting layer. A similar result has been observed by Lewis *et al.* on *GaAs* (110) substrates [11] and is not unexpected due to the low growth temperature. Upon the addition of low *Bi* flux it can be seen that a large number of QDs are formed in layer L1 and these QDs get progressively taller as the *Bi* flux is increased for L2 and L3. Present in all of the layers grown at 380 °C where a *Bi* flux was supplied is a background of short QDs. These are most evident in the image for L3 in Figure 11.1. The QD layers grown at 510 °C all displayed QD formation and are visibly more uniform and taller than their low growth temperature equivalents.

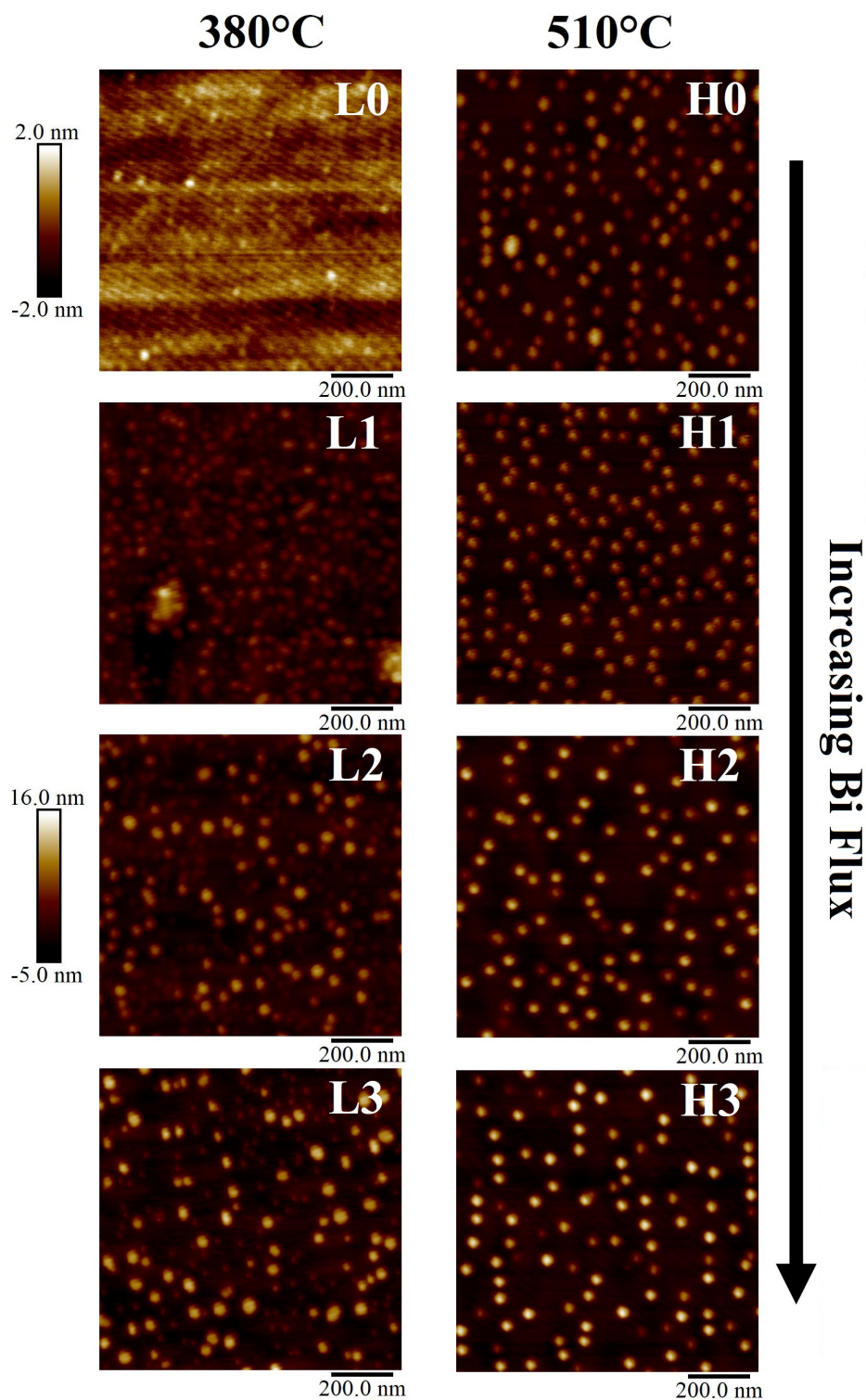


*Figure 11.1: AFM images of the QD layers.*

Figure 11.2 displays height histograms for all the layers using the QD population data extracted using the MATLAB software. Gaussian fits have been added to estimate the mean QD height and calculate the QD surface density using the number of AFM scans processed for each layer. These values are shown in Table 11.1. A bimodal distribution for QD height is seen in the 380 °C layers grown with a *Bi* flux, as mentioned above for the raw AFM images. These short QDs are between 1 – 4 nm tall and are clearly distinct from the taller QDs

Layer	QD Density	Mean Height
	(Short/Tall) ( $10^8/cm^2$ )	(Short/Tall) ( $nm$ )
L0	2.4 / 0	1.656 / 0
L1	13.4 / 110.2	1.367 / 3.329
L2	21.6 / 61.4	1.186 / 6.407
L3	90.0 / 42.4	2.009 / 9.712
H0	0/114.3	0 / 6.171
H1	0/129.4	0 / 8.464
H2	0/52.8	0 / 10
H3	0/57.6	0 / 12.998

*Table 11.1: Summary of STK7 AFM characterisation.*

for layer L1-L3. The origin of these short QDs is believed to originate from nucleation transitions which occur below 1.6  $ML$  which have been observed elsewhere at low growth temperatures [19, 23, 24]. At both growth temperatures, higher  $Bi$  fluxes produced taller QDs although the QDs grown at 510 °C are consistently taller than those grown at 380 °C, again, as seen in Figure 11.1.

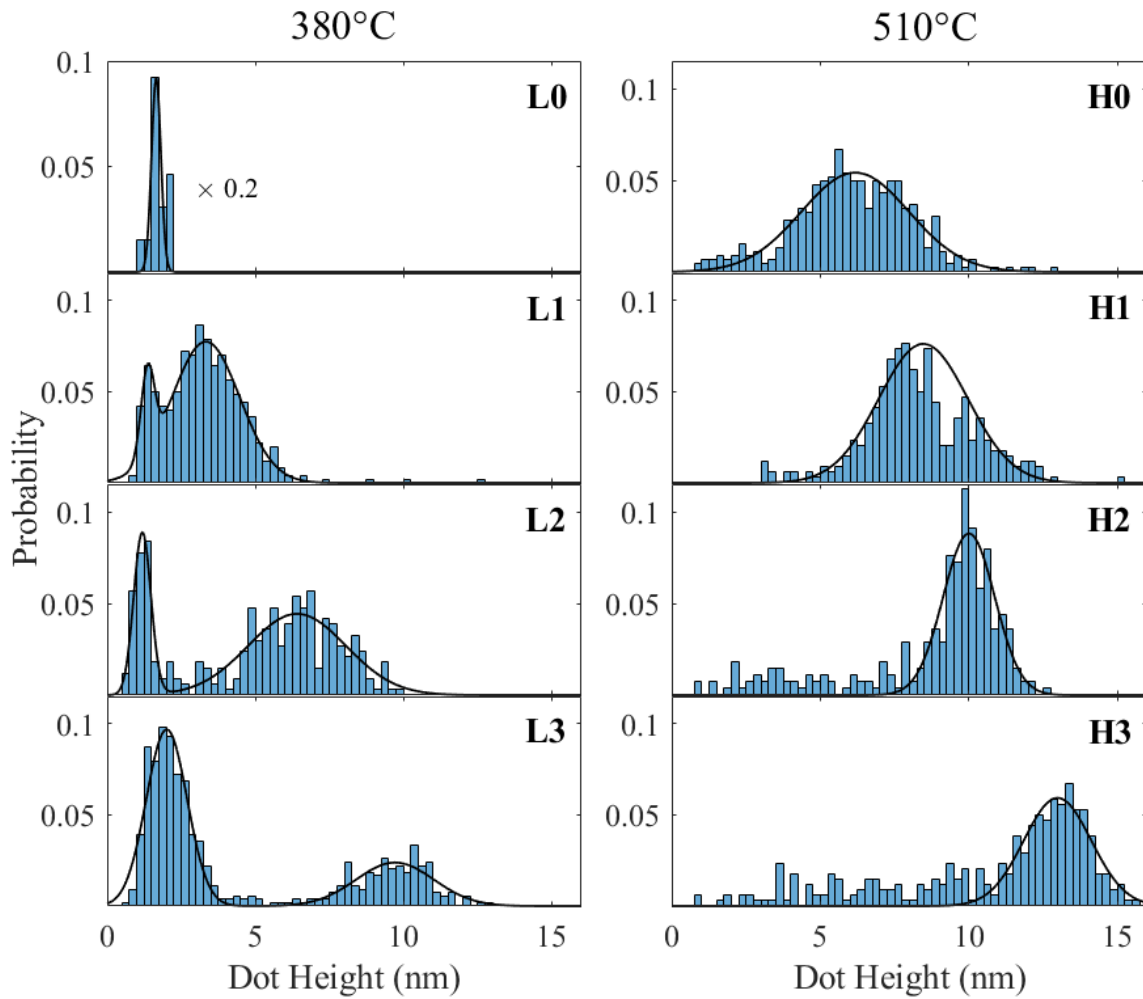


Figure 11.2: Height histograms for all the QD layers. Gaussian fits have been added.

Figure 11.3 displays the QD surface densities calculated using the Gaussian fits to the layers displayed in Figure 11.2. There is only a single entry for the QDs grown at 510 °C as the layers were not bimodal whereas the layers grown at 380 °C which were bimodal have entries for both the short and tall QDs. Looking at the trend in the 510 °C layers the QD density is approximately constant for the growths without a *Bi* flux and with a low *Bi* flux, as the flux is increased further, however, the density drops to  $\sim 60 - 70\%$  of the density calculated for H1. This closely follows the results seen by Fan *et al.* who observed a 50 % decrease in QD density while using a *Bi* surfactant [9]. As for the layers grown at 380 °C, throughout the series as the *Bi* flux is increased the density of short QD increases, with a large increase for L3. In contrast to this, after the initial increase where large QDs are formed for L1, the density of tall QDs drops in a linear trend with increasing *Bi* flux.

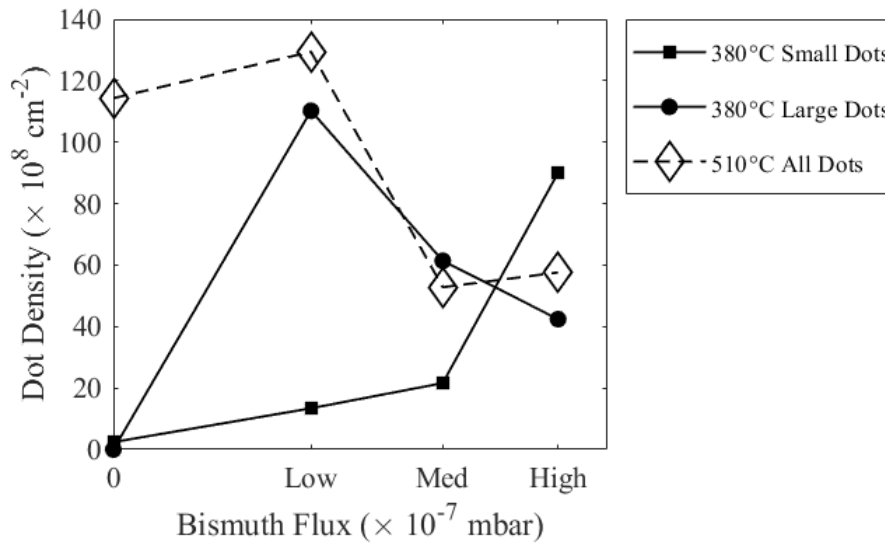


Figure 11.3: Plot of QD density versus Bi flux. Values are calculated using the Gaussian fits displayed in Figure 11.2.

As mentioned in Section 10.2 one of the benefits of using the custom designed MATLAB software is that it allows the QD population to be inspected as a comprehensive list of characteristics tied to individual QDs. Therefore with the values for height and area of each QD it was possible to calculate an approximate aspect ratio for each QD. This is only approximate for several reasons, the first is that the AFM data was not corrected for tip size, meaning the QDs will appear wider and flatter than they actually are. The second reason is that these QDs are uncapped and not perfectly representative of the capped QDs which will have undergone some intermixing during the capping process. Finally, the aspect ratio was calculated using a circular assumption for the QD base which is known to not be the case and varies depending on the growth conditions. Nevertheless, the values for aspect ratio are still of interest for comparing across this series.

A scatter plot of the aspect ratio versus QD height for each layer is shown in Figure 11.4. Layer L0 has been omitted from this figure as the difficulty with separating the small number of QDs from the wetting layer made any values calculated unreliable. For the low growth temperature layers Figure 11.4 provides an alternative illustration of the bimodal distribution splitting which was seen in Figure 11.2. Generally all the layers follow the same evolution in aspect ratio as H0 which had the narrowest distribution of values, the trendline for which was used as a guide for the other layers. The only layer with any significant deviation from the H0 trend was H1 which, despite not displaying a clear bimodal distribution in Figure 11.2, has two distinct QD distributions in Figure 11.4. This is not seen at higher *Bi* fluxes or in the layers growth at 380 °C. The mean aspect ratio for this new distribution is  $\bar{0}.31$ . This phenomenon is similar to a change in aspect ratio seen by Saito *et al.* [25] who reported a change in aspect ratio from 0.22 to 0.33. This change was attributed to the higher aspect ratio becoming more energetically favourable once the QD volume passed a critical volume. As the taller, and therefore larger due to the reduced aspect ratio, QDs in the layers grown at higher *Bi* fluxes do not display this change it is expected to not be purely driven by volume and the *Bi* is also changing conditions on the surface to make this transition favourable.

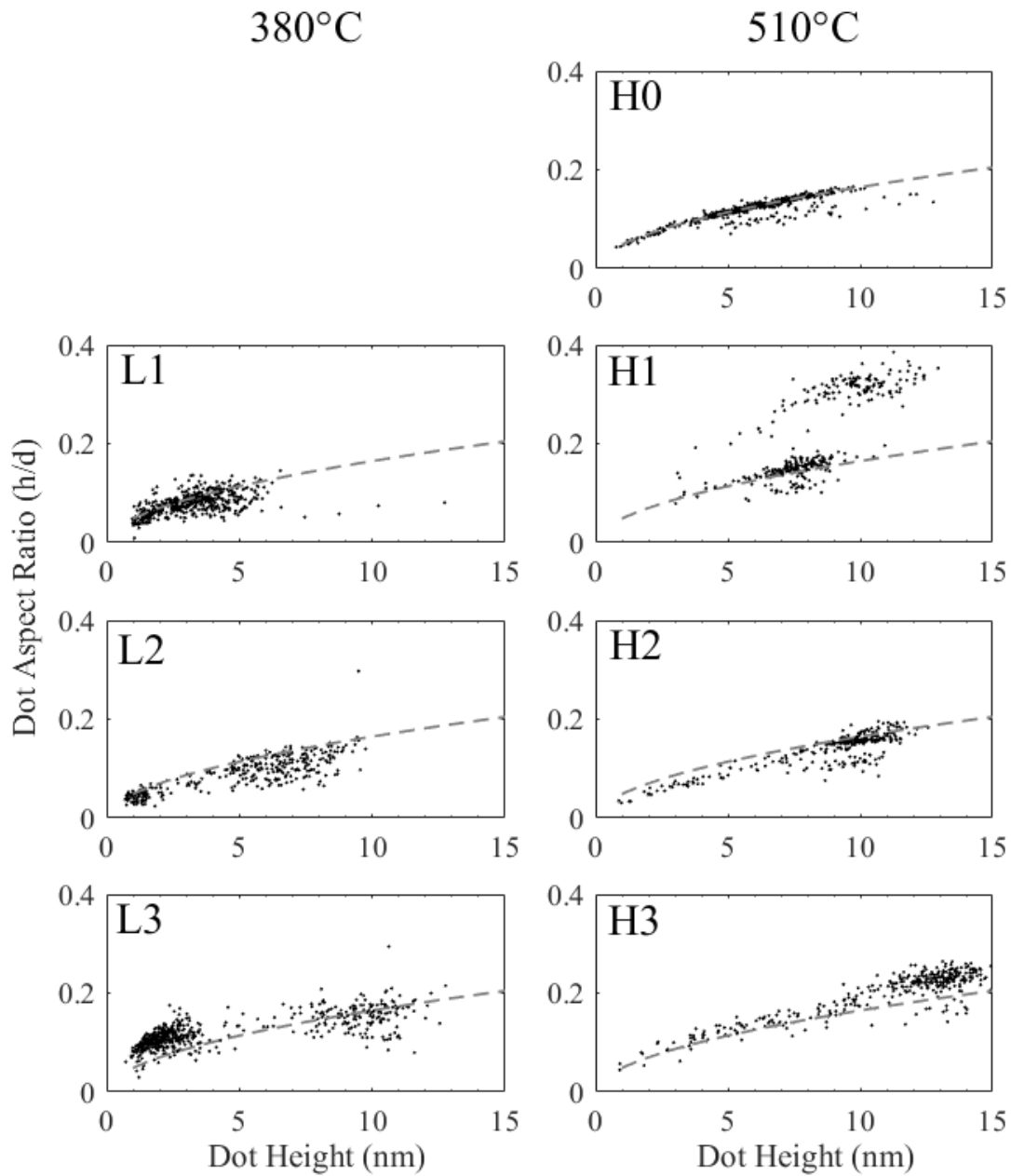


Figure 11.4: Aspect ratio scatter plots for all of the QD layers. Layer L0 has been omitted due to the small identified QD population and difficulty with measuring the dot base area. To aid in comparison across the layers the trendline for H0 (dashed grey) has been overlaid on all axes.

The final piece of analysis which can be performed with the processed AFM data is comparing the total volume of the QDs with the supplied volume of material. It has been reported, however, that at high growth temperatures increased mass transport and  $In-Ga$  alloying results in QD volumes exceeding that which was deposited [26]. Using ex-situ AFM for this does introduce some, however, as there will be some  $InAs$  within the wetting layer which will cannot be measured and accounted for from the AFM data. Therefore it is expected that the values calculated will be an underestimate of the total material. The results of this analysis are shown in Figure 11.5.

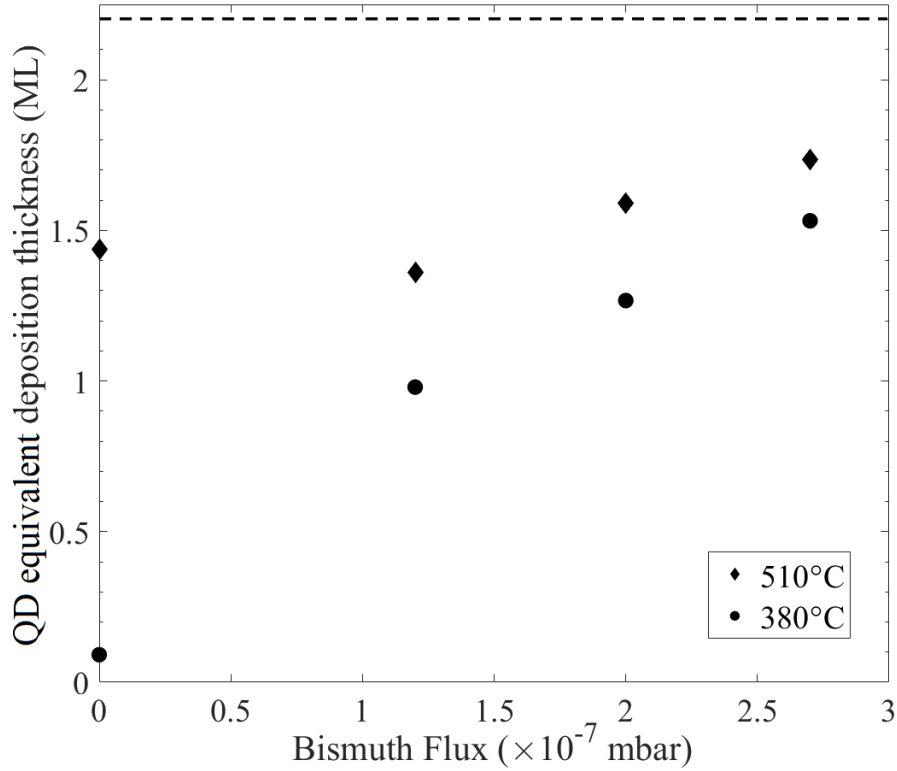


Figure 11.5: The equivalent 2D deposition thickness of the surface QD populations. A black dashed line has been added to show the supplied deposition thickness. The low calculated deposition for layer L0 is expected to be inaccurate as there was negligible QD formation and most of the InAs deposition will have formed a wetting layer.

As mentioned in Section 10.1, 2.2 ML of InAs was deposited in each layer. If all the supplied InAs formed QDs (i.e. VM growth discussed in Section 2.5.1) then the total QD volume would match the dashed, black line at 2.2 ML in Figure 11.5. As seen, in all cases the total QD volume of the layers is below that which was deposited. At a growth temperature of 380 °C the layer grown with the lowest non-zero Bi flux, L1, has an equivalent thickness which has good agreement with that seen elsewhere for the same deposition thickness and temperature range by Joyce *et al.* [26]. In their work changing the deposition thickness of InAs at this temperature yielded a QD volume line which matched the deposited material with consistent offset, suggesting static volume of material forming the wetting layer. With an increase of Bi flux at this temperature the calculated QD equivalent thickness increases, implying a mixture of decreased wetting layer thickness and increased In – Ga alloying from the substrate. A similar effect is seen for medium and high Bi fluxes at 510 °C although with a smaller magnitude. This may be due In – Ga alloying already occurring at this temperature and therefore the additional Bi is only contributing to the effect.

## 11.2 PL RESULTS

PL taken on each of the QD layers at room temperature is shown in Figure 11.6. This data has been normalised to the highest intensity recorded which was for layer H2 at 900 mW. The layers grown at 510 °C all displayed stronger emission intensity than the layers grown at 380 °C for all Bi fluxes. This is expected to be due to

an increase in crystal defect density within the QD and capping layers reducing the non-radiative lifetime of carriers in the 380 °C layers caused by the reduced growth temperature. All of the layers have a broad, long wavelength emission between 0.7 - 0.9 eV which is not considered to be QD emission. This is referred to as the low energy feature (LEF) and appears to not be widely reported on in the literature. Two literature reports have been found which discuss such long wavelength emission for *GaAs* based QDs.

The first is a similar study on *InAs* QD growth using *Bi* by Wang *et al.* which investigated growth of QDs on or capped with *GaAsBi* [15]. In their work this emission was observed in PL at 77 K for several layers with the line-shape of the emission showing a large dependence on the growth structure. They attributed its origin to the surface QD population. This is not expected to be the case in this work as, especially at room temperature, any carriers falling into the surface QDs are expected to be lost to surface states.

The other report is an older study of *InAs* QD growth on *GaAs* at low substrate temperatures or inside quantum well structures, presented by Ustinov *et al.* [27]. The long wavelength emission documented in their work more closely represents the LEF seen in this work although it was not observed in a layer grown 520 °C but was at the next lowest growth temperature of 450 °C. Through transmission electron microscopy it was reasoned that the source of this emission was from cluster and chain shaped agglomerates of QDs. If these were larger *InAs* islands it would be expected that these features would contain a large number of dislocation defects and not be optically active, however as these agglomerates are smaller covering  $\leq 1000 \text{ nm}^2$  it is assumed that the defect density is lower and some radiative recombination is possible.

Of the layers grown at 510 °C the longest wavelength emission was recorded for layer H1 at 0.987 eV. This is notable as this layer did not have the tallest QDs at this growth temperature, yet its emission peak is 11 meV below that of H3 which had QDs that were 4.5 nm taller on average. The only identified difference of this layer from the rest of the series is the higher aspect ratio QDs which were seen in the AFM analysis. It has been modelled elsewhere that the effect of a change in QD aspect ratio can have a large impact on QD emission wavelength [28], however, this still relies on an increase in QD height. As this aspect ratio was only observed here for the surface QDs it is uncertain how this may have affected the buried QDs. Given the differences seen in the PL it is possible the aspect ratio change in layer H1 introduced a mechanism which allowed them to remain taller during capping.

The longest wavelength emission at each *Bi* flux came from the 380 °C layers, with a minimum ground state energy of 0.968 eV for L2 and L3. It is possible these reduced energies are caused by *Bi* incorporation at this lower growth temperature. Another possibility is reduced In-Ga intermixing at 380 °C. However, this is already expected to have been affected by the low growth rate of  $0.01 \text{ ML s}^{-1}$  [29]. Alternatively this could be caused by the low temperature growth of the *GaAs* cap which has been seen to vary dramatically elsewhere [30].

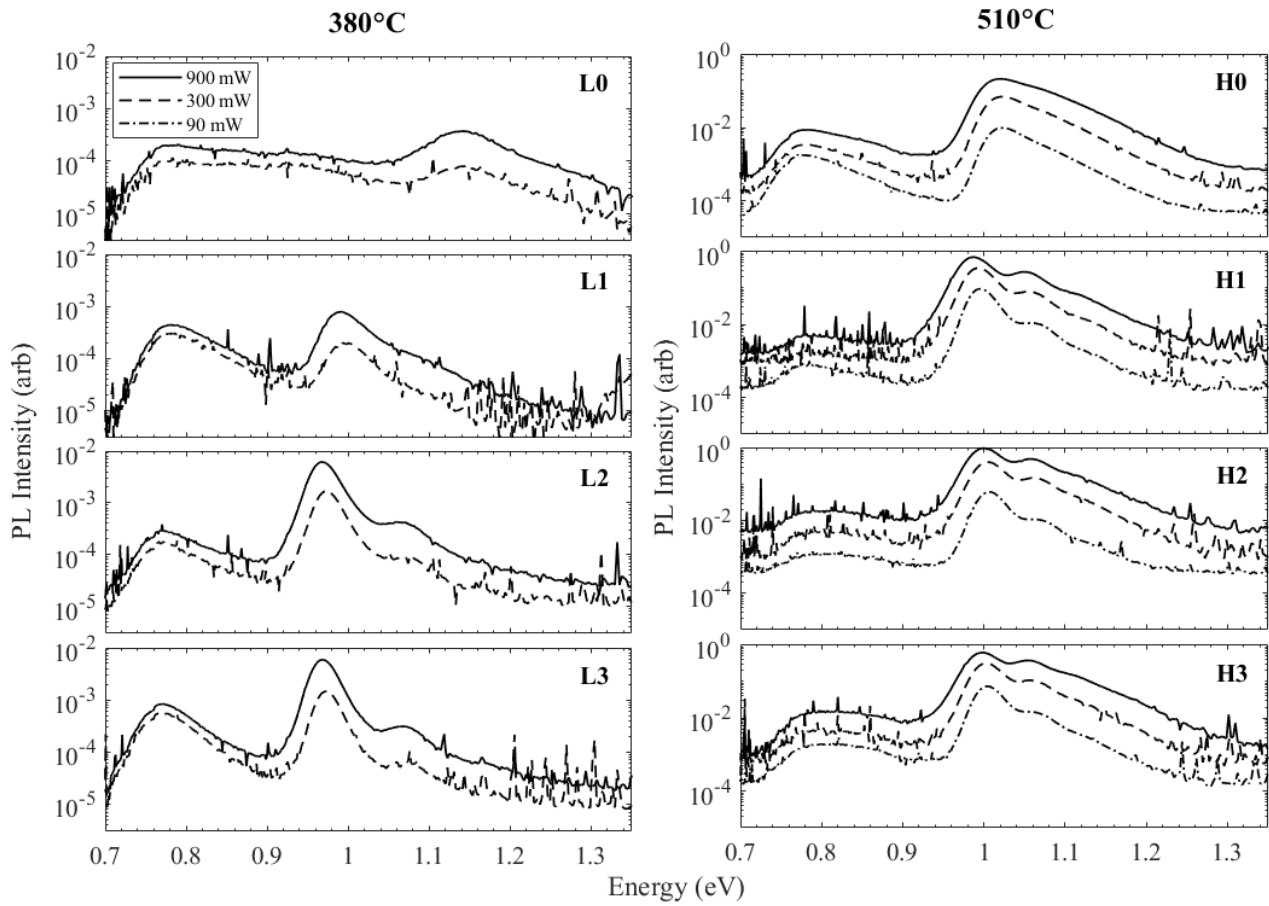


Figure 11.6: PL spectra taken at room temperature for the QD layers.

The integrated PL intensity from the QD layers under 900 *mW* excitation is shown in Figure 11.7. The LEF from each layer has also been added to observe how it changes with the growth conditions. At both growth temperatures the addition of a *Bi* flux increases the total integrated PL intensity with the medium *Bi* flux layers having the highest values for their respective series. The LEF for the layers grown at 510 °C is an order of magnitude below that of the QD PL in all cases although the integrated intensity increases to 2 – 3× for the medium and high flux layers. As these layers also displayed a large reduction in surface QD density these results provide further evidence to indicate the source of the LEF is QD agglomerates which are formed during QD coalescence. However, there is no trend in the LEF intensity for the 380 °C layers.

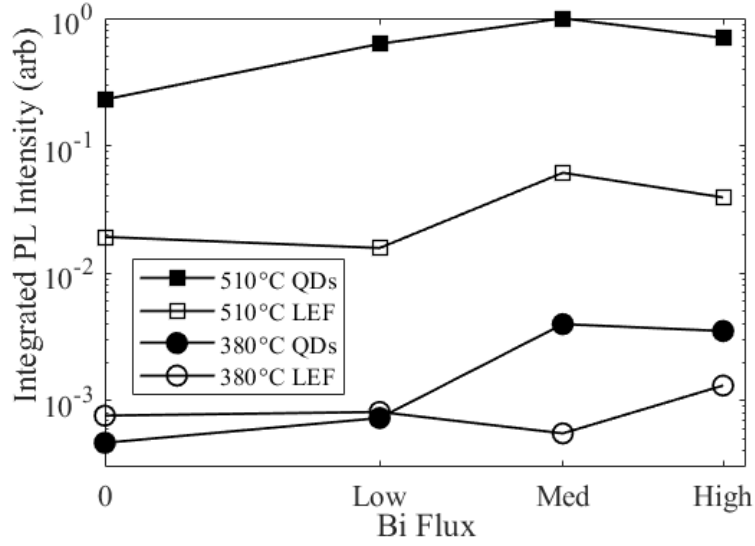


Figure 11.7: Plot of Integrated PL intensity at 900 mW versus Bi flux for the QD layers grown at 510 °C (squares) and 380 °C (circles). The LEF integrated intensity has been added (open symbols) to indicate trends with the growth conditions.

Layer	PL peak (900 mW) (eV)	PL FWHM (900 mW) (eV)	Integrated QD Intensity (900 mW)(arb)	Integrated LEF Intensity (900 mW)(arb)
L0	1.139	0.094	4.65e-4	7.60e-4
L1	0.992	0.051	7.27e-4	8.12e-4
L2	0.968	0.035	3.97e-3	5.52e-4
L3	0.968	0.033	3.51e-3	1.31e-3
H0	1.019	0.076	0.230	1.92e-2
H1	0.987	0.043	0.630	1.57e-2
H2	1.000	0.045	1	6.13e-2
H3	0.998	0.053	0.700	3.92e-2

Table 11.2: Summary of the QD PL characterisation.

## 12 CONCLUSIONS

In summary, it has been shown that the application of a bismuth flux during quantum dot nucleation leads to the formation of taller indium arsenide quantum dots on gallium arsenide in all cases as well as improving emission intensity compared to layers grown without a bismuth flux. Estimations of quantum dot 2D thickness suggests bismuth increases indium-gallium alloying with this effect being most pronounced at low growth temperatures. Expected red-shifts due to reduced confinement energies has been evidenced in Figure 11.6. An additional red-shift which is believed to be caused by a change in quantum dot aspect ratio, recorded by surface atomic force microscopy measurements, has also been observed in layer H2. These results indicate that in addition

to bismuth impacting the size and density of quantum dots, it may also be used to drive changes in surface morphology allowing further reductions in quantum dot emission wavelength. Given that this has only been observed in one layer, however, further study is required to confirm the repeatability of this result.

## REFERENCES

- [1] Y. Arakawa and H. Sakaki, "Multidimensional quantum well laser and temperature dependence of its threshold current," *Applied physics letters*, vol. 40, no. 11, pp. 939–941, 1982.
- [2] X. Lu, N. Kumagai, Y. Minami, T. Kitada, and T. Isu, "Effects of *Sb*-soak on *InAs* quantum dots grown on (001) and (113)B *GaAs* substrates," *Journal of Crystal Growth*, vol. 477, pp. 221–224, 2017.
- [3] T. Matsuura, T. Miyamoto, T. Kageyama, M. Ohta, Y. Matsui, T. Furuhashi, and F. Koyama, "Surfactant effect of *Sb* on *GaInAs* quantum dots grown by molecular beam epitaxy," *Japanese journal of applied physics*, vol. 43, no. 5A, p. L605, 2004.
- [4] L. Dai, S. P. Bremner, S. Tan, S. Wang, G. Zhang, and Z. Liu, "Raman scattering study on *Sb* spray *InAs/GaAs* quantum dot nanostructure systems," *Nanoscale research letters*, vol. 10, no. 1, pp. 1–6, 2015.
- [5] A. Salhi, S. Alshaibani, Y. Alaskar, A. Albadri, A. Alyamani, and M. Missous, "Tuning the optical properties of *InAs* QDs by means of digitally-alloyed *GaAsSb* strain reducing layers," *Applied Physics Letters*, vol. 113, no. 10, p. 103101, 2018.
- [6] Z. Zhang, Y. Huang, P. J. Reece, and S. P. Bremner, "Influence of *GaAsSb* structural properties on the optical properties of *InAs/GaAsSb* quantum dots," *Physica E: Low-dimensional Systems and Nanostructures*, vol. 94, pp. 7–14, 2017.
- [7] Y.-A. Liao, W.-T. Hsu, S.-H. Huang, P.-C. Chiu, J.-I. Chyi, and W.-H. Chang, "Band alignment tuning of *InAs* quantum dots with a thin *AlGaAsSb* capping layer," *Applied Physics Letters*, vol. 102, no. 17, p. 173104, 2013.
- [8] K. Yamaguchi and T. Kanto, "Self-assembled *InAs* quantum dots on *GaSb/GaAs* (001) layers by molecular beam epitaxy," *Journal of Crystal Growth*, vol. 275, no. 1-2, pp. 2269–2273, 2005.
- [9] D. Fan, Z. Zeng, V. G. Dorogan, Y. Hirono, C. Li, Y. I. Mazur, S.-Q. Yu, S. R. Johnson, Z. M. Wang, and G. J. Salamo, "Bismuth surfactant mediated growth of *InAs* quantum dots by molecular beam epitaxy," *Journal of Materials Science: Materials in Electronics*, vol. 24, no. 5, pp. 1635–1639, 2013.
- [10] D. F. Reyes, D. Gonzalez, F. Bastiman, L. Dominguez, C. J. Hunter, E. Guerrero, M. A. Roldan, A. Mayoral, J. P. David, and D. L. Sales, "Photoluminescence enhancement of *InAs(Bi)* quantum dots by *Bi* clustering," *Applied Physics Express*, vol. 6, no. 4, p. 042103, 2013.
- [11] R. B. Lewis, A. Trampert, E. Luna, J. Herranz, C. Pfüller, and L. Geelhaar, "Bismuth-surfactant-induced growth and structure of *InAs/GaAs* (110) quantum dots," *Semiconductor Science and Technology*, vol. 34, no. 10, p. 105016, 2019.
- [12] V. D. Dasika, E. Krivoy, H. P. Nair, S. Maddox, K. Park, D. Jung, M. Lee, E. T. Yu, and S. R. Bank, "Increased *InAs* quantum dot size and density using bismuth as a surfactant," *Applied Physics Letters*, vol. 105, no. 25, p. 253104, 2014.
- [13] X. Chen, Y. Gu, Y. Ma, S. Chen, M. Tang, Y. Zhang, X. Yu, P. Wang, J. Zhang, J. Wu, *et al.*, "Growth mechanisms for *InAs/GaAs* QDs with and without Bi surfactants," *Materials Research Express*, vol. 6, no. 1, p. 015046, 2018.

- [14] S. Francoeur, M.-J. Seong, A. Mascarenhas, S. Tixier, M. Adamcyk, and T. Tiedje, “Band gap of  $GaAs_{1-x}Bi_x$ ,  $0 < x < 3.6\%$ ,” *Applied physics letters*, vol. 82, no. 22, pp. 3874–3876, 2003.
- [15] L. Wang, W. Pan, X. Chen, X. Wu, J. Shao, and S. Wang, “Influence of  $Bi$  on morphology and optical properties of  $InAs$  QDs,” *Optical Materials Express*, vol. 7, no. 12, pp. 4249–4257, 2017.
- [16] H. Okamoto, T. Tawara, H. Gotoh, H. Kamada, and T. Sogawa, “Growth and characterization of telecommunication-wavelength quantum dots using  $Bi$  as a surfactant,” *Japanese Journal of Applied Physics*, vol. 49, no. 6S, p. 06GJ01, 2010.
- [17] B. Zvonkov, I. Karpovich, N. Baidus, D. Filatov, S. Morozov, and Y. Y. Gushina, “Surfactant effect of bismuth in the MOVPE growth of the  $InAs$  quantum dots on  $GaAs$ ,” *Nanotechnology*, vol. 11, no. 4, p. 221, 2000.
- [18] X.-D. Wang, N. Liu, C. Shih, S. Govindaraju, and A. Holmes Jr, “Spatial correlation-anticorrelation in strain-driven self-assembled *ingaas* quantum dots,” *Applied physics letters*, vol. 85, no. 8, pp. 1356–1358, 2004.
- [19] F. Patella, F. Arciprete, M. Fanfoni, A. Balzarotti, and E. Placidi, “Apparent critical thickness versus temperature for  $InAs$  quantum dot growth on  $GaAs$  (001),” *Applied physics letters*, vol. 88, no. 16, p. 161903, 2006.
- [20] K. Y. K. Yamaguchi, K. Y. K. Yujobo, and T. K. T. Kaizu, “Stranski-Krastanov growth of  $InAs$  quantum dots with narrow size distribution,” *Japanese journal of applied physics*, vol. 39, no. 12A, p. L1245, 2000.
- [21] Y. Kim, B. D. Min, and E. K. Kim, “Ripening suppression and large photoluminescence blueshift in aligned *ingaas* quantum dots on a vicinal (100) *gaas* substrate,” *Journal of applied physics*, vol. 85, no. 4, pp. 2140–2145, 1999.
- [22] K. Nishi, H. Saito, S. Sugou, and J.-S. Lee, “A narrow photoluminescence linewidth of 21 meV at 1.35  $\mu m$  from strain-reduced  $InAs$  quantum dots covered by  $In_{0.2}Ga_{0.8}As$  grown on  $GaAs$  substrates,” *Applied Physics Letters*, vol. 74, no. 8, pp. 1111–1113, 1999.
- [23] A. Polimeni, A. Patane, M. Capizzi, F. Martelli, L. Nasi, and G. Salviati, “Self-aggregation of quantum dots for very thin  $InAs$  layers grown on  $GaAs$ ,” *Physical Review B*, vol. 53, no. 8, p. R4213, 1996.
- [24] A. Patane, M. Grassi Alessi, F. Intonti, A. Polimeni, M. Capizzi, F. Martelli, L. Nasi, L. Lazzarini, G. Salviati, A. Bosacchi, *et al.*, “Self-aggregated  $InAs$  quantum dots in  $GaAs$ ,” *Journal of applied physics*, vol. 83, no. 10, pp. 5529–5535, 1998.
- [25] H. Saito, K. Nishi, and S. Sugou, “Shape transition of  $InAs$  quantum dots by growth at high temperature,” *Applied Physics Letters*, vol. 74, no. 9, pp. 1224–1226, 1999.
- [26] P. Joyce, T. Krzyzewski, G. Bell, B. Joyce, and T. Jones, “Composition of *inas* quantum dots on *gaas* (001): Direct evidence for (*in*, *ga*) *as* alloying,” *Physical Review B*, vol. 58, no. 24, p. R15981, 1998.
- [27] V. Ustinov, A. Zhukov, A. Kovsh, N. Maleev, S. Mikhlin, A. Tsatsul’nikov, M. Maximov, B. Volovik, D. Bedarev, P. Kop’ev, *et al.*, “Long-wavelength emission from self-organized  $InAs$  quantum dots on  $GaAs$  substrates,” *Microelectronics Journal*, vol. 31, no. 1, pp. 1–7, 2000.

- [28] M. Usman, H. Ryu, I. Woo, D. S. Ebert, and G. Klimeck, "Moving toward nano-TCAD through multimillion-atom quantum-dot simulations matching experimental data," *IEEE Transactions on Nanotechnology*, vol. 8, no. 3, pp. 330–344, 2009.
- [29] P. Joyce, T. Krzyzewski, G. Bell, T. Jones, S. Malik, D. Childs, and R. Murray, "Effect of growth rate on the size, composition, and optical properties of *InAs/GaAs* quantum dots grown by molecular-beam epitaxy," *Physical Review B*, vol. 62, no. 16, p. 10891, 2000.
- [30] Q. Gong, P. Offermans, R. Nötzel, P. Koenraad, and J. Wolter, "Capping process of *InAs/GaAs* quantum dots studied by cross-sectional scanning tunnelling microscopy," *Applied physics letters*, vol. 85, no. 23, pp. 5697–5699, 2004.

## PART IV

# GROWTH OF $AlGaAsBi$ BY MBE

## 13 LITERATURE REVIEW

To date there has been little literature discussion of aluminium gallium arsenide bismide ( $AlGaAsBi$ ) growth or characterisation in the literature. Currently the only similar growth work is by Wang *et. al* [1] who synthesised  $AlAsBi$  using stationary growth on 2 inch  $GaAs$  substrates. They produced layers at 310 and 270 °C and characterised them by XRD and RBS to produce an experimental estimation for the lattice constant for  $AlBi$  of (6.23Å).

The aim of this chapter is to take the first step towards bridging the gap between  $GaAsBi$  and  $AlAsBi$  by undertaking a growth study looking at  $Bi$  incorporation at multiple  $Al_xGa_{1-x}As$  compositions. Layers will be analysed XRD and RBS in order to characterise how  $Bi$  incorporates into  $AlGaAs$ . For clarity of input, the RBS measurements and modelling were performed by the Ion Beam Centre at the University of Surrey.

## 14 MATERIAL GROWTH CONDITIONS AND CHARACTERISATION

The layers which make up this series are test structures which were designed to cover a wide area of the parameter space between  $GaAs$  and  $AlAs$ . This is illustrated in Table 14.1 which indicates the range of  $Al$  compositions and  $Bi$  fluxes used.

Layer	Target $Al$ (%)	$Bi$ Flux ( $\times 10^{-7}$ ) mbar
STL46	30	1.27
STL43	30	2.62
STL47	30	4.05
STL4A	45	1.27
STL49	45	2.62
STL4G	45	5.2
STL4H	60	2.48
STL4J	80	2.48

Table 14.1: Summary of STL4 growth conditions.

The structure of the layers in this series is displayed in Figure 14.1. As can be seen, multiple growth temperatures were used during each growth sequence, 375 °C was selected to allow efficient  $Bi$  incorporation into the  $AlGaAs$  lattice under the initial assumption the temperature limit would not be lower than for  $GaAsBi$ . 615 °C was used for the first  $AlGaAs$  layer in order to achieve the highest crystal quality possible prior to cooling the

substrate for bismide growth. One notable feature in this structure which is not always seen in bismide literature is the 10 nm host alloy layer (*AlGaAs* in this series) which was also deposited at 375 °C. This was used to prevent segregation of *Bi* from the exposed *AlGaAsBi* surface during the growth interrupt when the substrate temperature was increased for the *AlGaAs/GaAs* cap growth. The nominal flux ratios quoted on the right side of Figure 14.1 are atomic flux ratios which have been calculated using an *As* : *Ga* calibration, as discussed in Section 3.6.3, at the *GaAs* growth rate of 0.31 *ML s*<sup>-1</sup> and have been scaled to the *AlGaAs* growth rate using a linear fit to the dependence of the *As* BEP on the position of the cells needle valve. The temperatures and ratios in Figure 14.1 are accurate to ±5 °C and ±5% respectively. It is noted that the *As*<sub>4</sub> : *III* ratio is at the lower than is generally used for bismide growth, but this is still expected to be within the stable range of *As* fluxes, as displayed in Figure 3.6 in Section 3.6.3.

	GaAs 50 nm	<i>As</i> <sub>2</sub> : <i>III</i> = 1.58
$G_T = 585^\circ\text{C}$	AlGaAs 90 nm	<i>As</i> <sub>2</sub> : <i>III</i> = 1.33
	AlGaAs 10 nm	
$G_T = 375^\circ\text{C}$	AlGaAsBi 100 nm	<i>As</i> <sub>4</sub> : <i>III</i> = 1.72
$G_T = 615^\circ\text{C}$	AlGaAs 100 nm	<i>As</i> <sub>2</sub> : <i>III</i> = 1.33
$G_T = 585^\circ\text{C}$	GaAs 300-400 nm	<i>As</i> <sub>2</sub> : <i>III</i> = 1.58
	GaAs (001)	

Figure 14.1: General Growth Structure of the *STL4* layer series.

Cleaved pieces of these layers were characterised by Nomarski microscopy and XRD before being subjected to RBS experiments in order to independently verify their elemental composition. The results of this are presented next in Section 15.

## 15 RESULTS AND DISCUSSION

### 15.1 NOMARSKI MICROSCOPY RESULTS

Figures 15.1 through to 15.8 show Nomarski microscopy images for all the layers grown at ×5 and ×50 magnification. Unfortunately due to a software change on the Nomarski setup scale bars are no longer added and these images can only be used for qualitative purposes. In order to split up the images and text appropriately; each layer will have a brief discussion below their respective images.



(a)



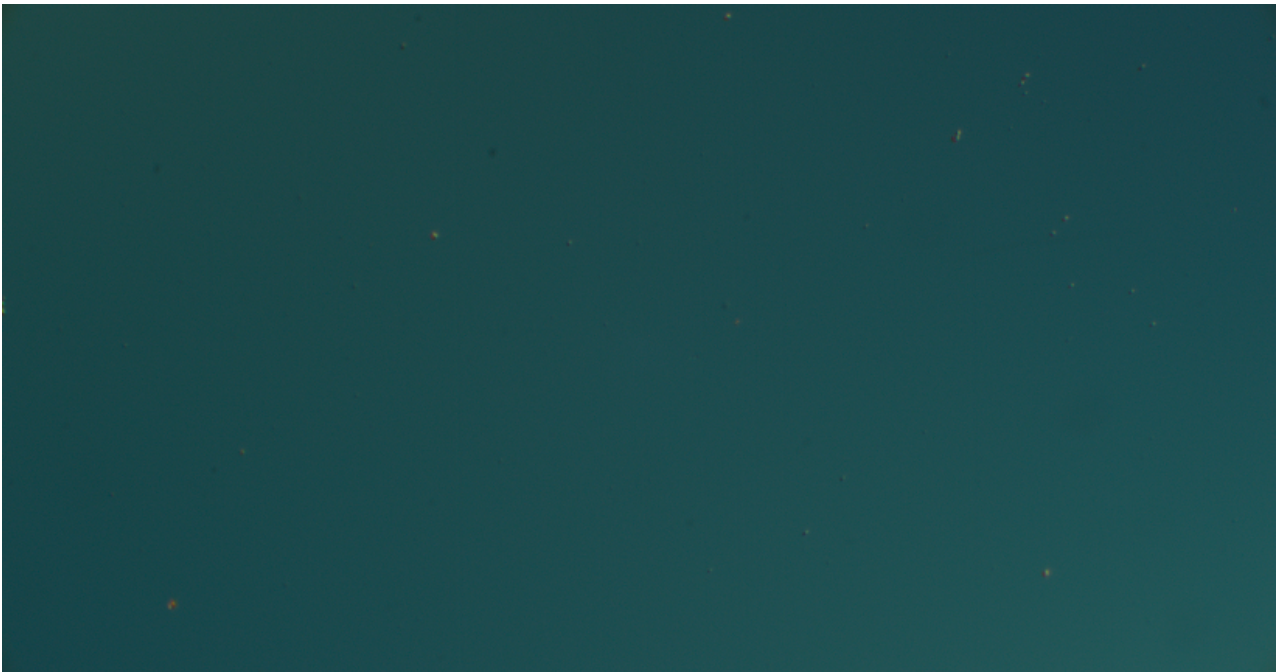
(b)

*Figure 15.1: Nomarski images of STL46 at (a)  $\times 5$  and (b)  $\times 50$  magnification.*

Whilst from Figure 15.1a the surface of STL46 initially appears to be of poor quality, the majority of this surface contamination is from third-party ex-situ handling of this wafer (as well as STL43 and STL47) for PL measurements as the *Al* composition was within the direct band gap range of *AlGaAs*. Looking closer at the surface in Figure 15.1b it can be seen that the background, in between the sporadic defects and handling contamination, is smooth. This indicates that there has been no relaxation in the structure and that the *As* flux ratio is sufficient to prevent either *Ga*-rich growth or the formation of point defects such as vacancies or antisites.



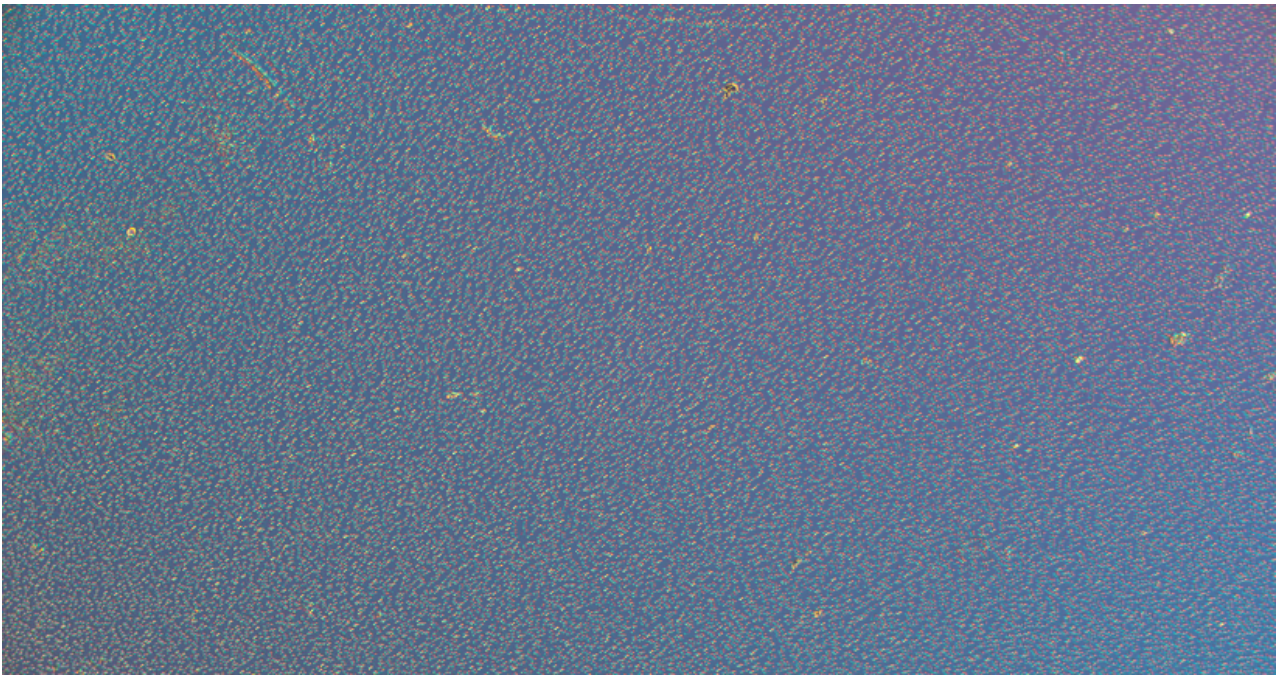
(a)



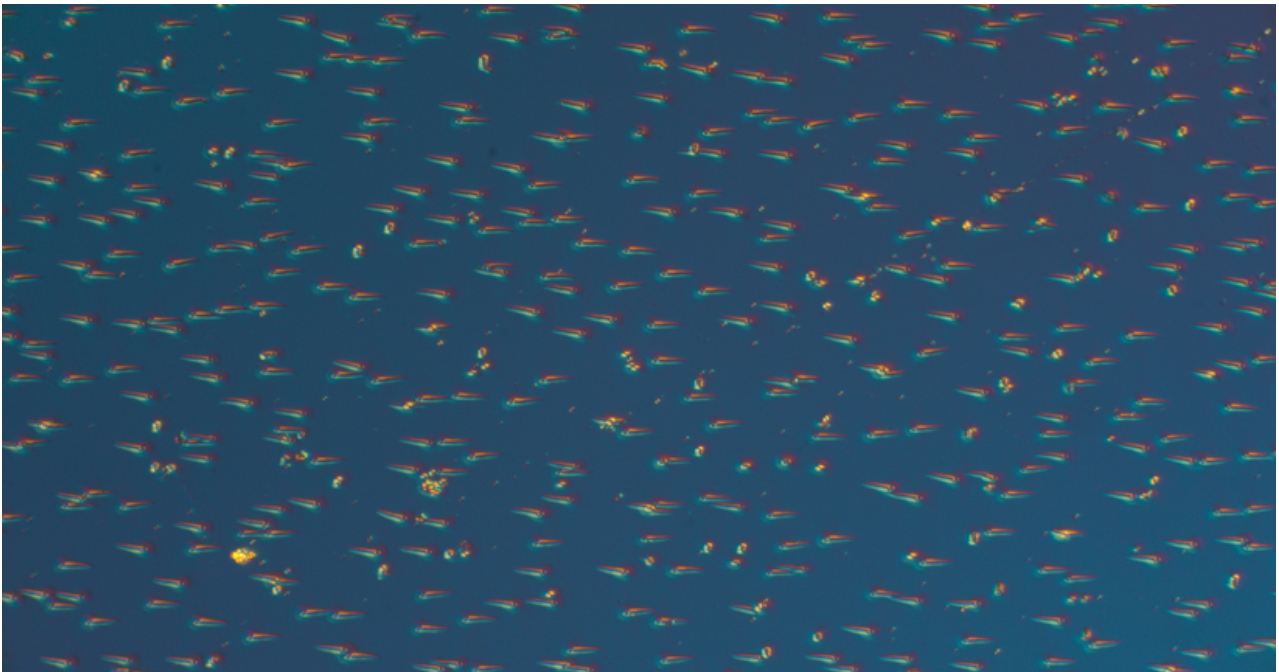
(b)

*Figure 15.2: Nomarski images of STL43 at (a)  $\times 5$  and (b)  $\times 50$  magnification.*

The surface of STL43 follows a similar trend to STL46, with surface contamination from handling visible, in Figure 15.2a, and a smooth background in Figure 15.2b. There do appear to be several faint vertical line dislocations visible around the centre of the image, however, suggesting minor relaxation in the layer.



(a)



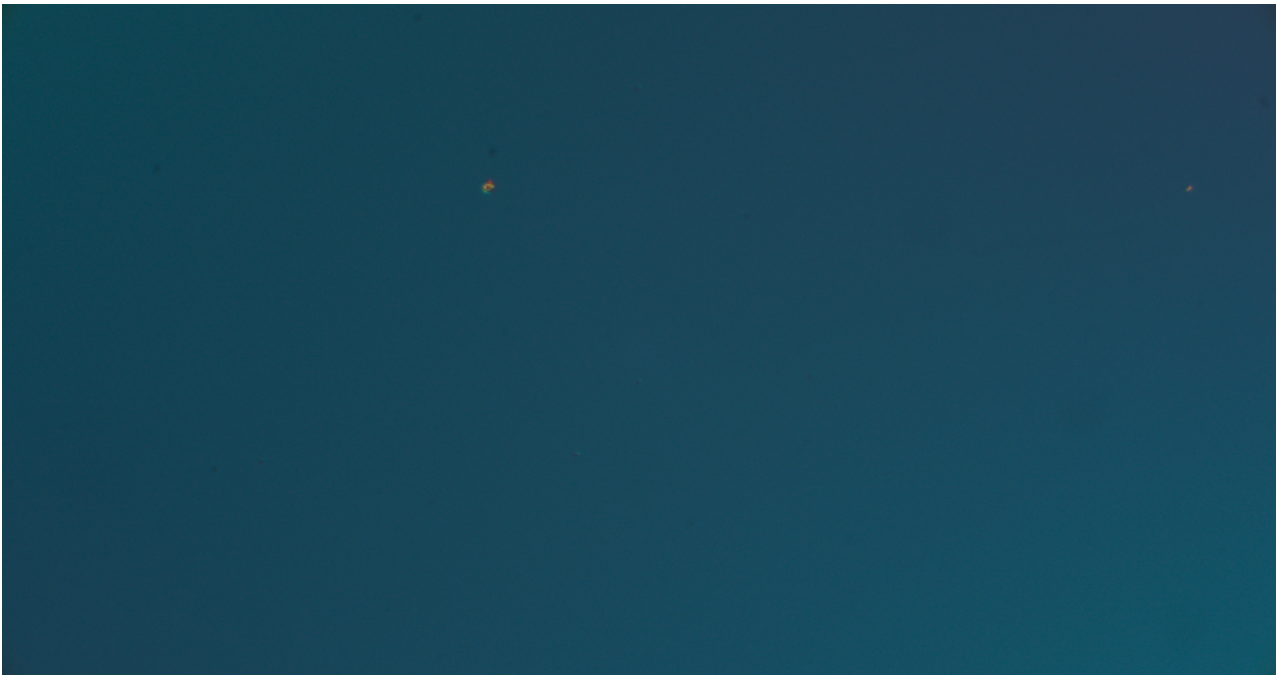
(b)

Figure 15.3: Nomarski images of STL47 at (a)  $\times 5$  and (b)  $\times 50$  magnification.

Grown under the highest *Bi* flux at a nominal *Al* composition of 30 %, STL47 displays a completely different surface morphology to STL46 and STL43. When viewed at  $\times 50$ , in Figure 15.3b, the defects which dominate the surface in both images appear dash-like and orientated along the crystal lattice. These may be the result of droplet nucleation during growth of the *AlGaAsBi* layer which would have led to VLS growth similar to that described in Section 4.3. Despite the disruption to the surface, however, there is no evidence of relaxation in the background of the image.



(a)



(b)

*Figure 15.4: Nomarski images of STL4A at (a)  $\times 5$  and (b)  $\times 50$  magnification.*

Moving onto the layers grown at  $\sim 45\%$  Al, the surface of STL4A has fewer defects than previously seen although this is largely due to it not being handled for PL measurements.



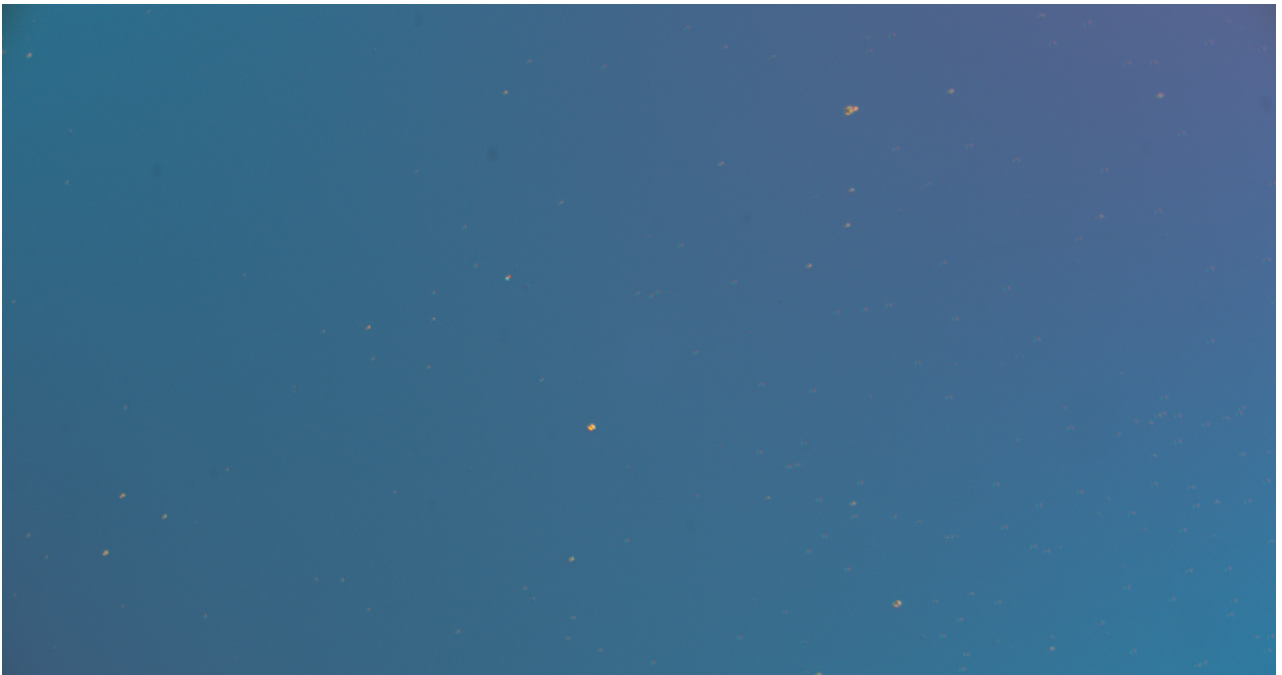
(a)



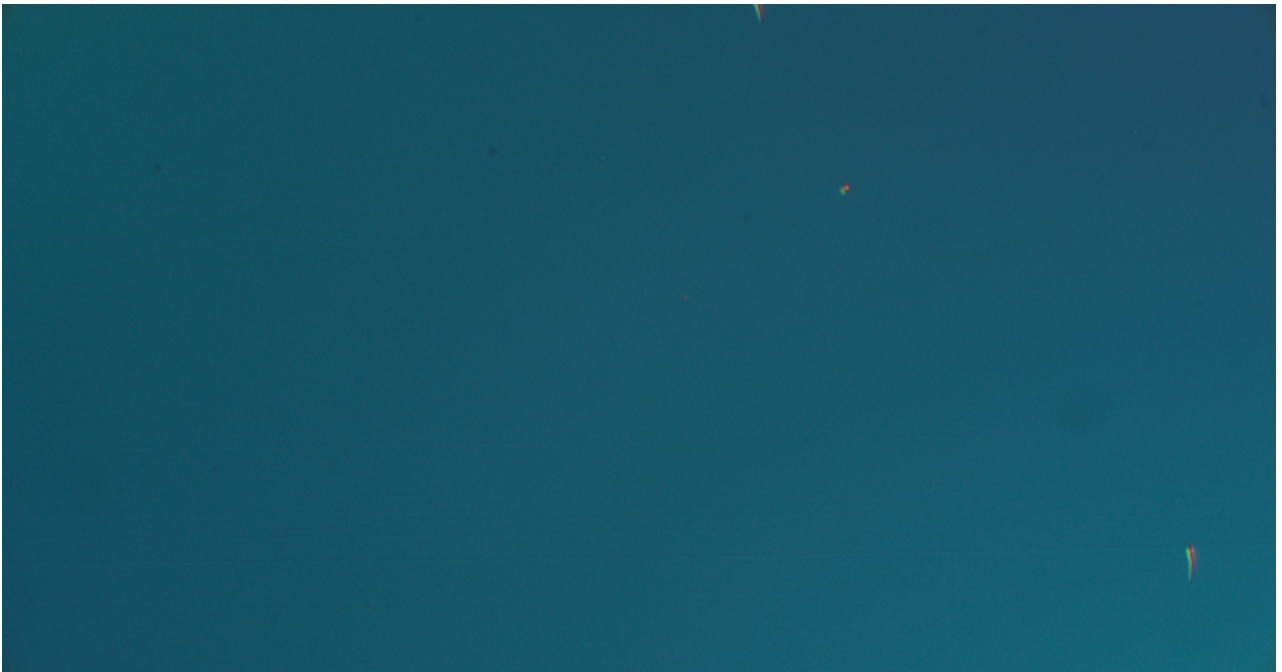
(b)

*Figure 15.5: Nomarski images of STL49 at (a)  $\times 5$  and (b)  $\times 50$  magnification.*

STL49 has noticeably more defects than STL4A at both magnifications. It also has a small number of line dislocations visible in Figure 15.5b, similar to that seen for STL43 which was grown with a similar *Bi* flux.



(a)



(b)

*Figure 15.6: Nomarski images of STL4G at (a)  $\times 5$  and (b)  $\times 50$  magnification.*

Despite being grown with a higher  $Bi$  flux than STL47 which was covered with droplets; STL4G has a much cleaner surface. Considering this, it is possible that the growth of STL47 was influenced by factors outside of the targeted growth conditions and was spoiled by improper substrate cleaning or a recipe error. Imaging of STL4G at  $\times 50$  magnification does indicate higher relaxation than seen in the previous layers, however, which is visible as an increased number of line dislocations at both crystallographic orientations in Figure 15.6b.



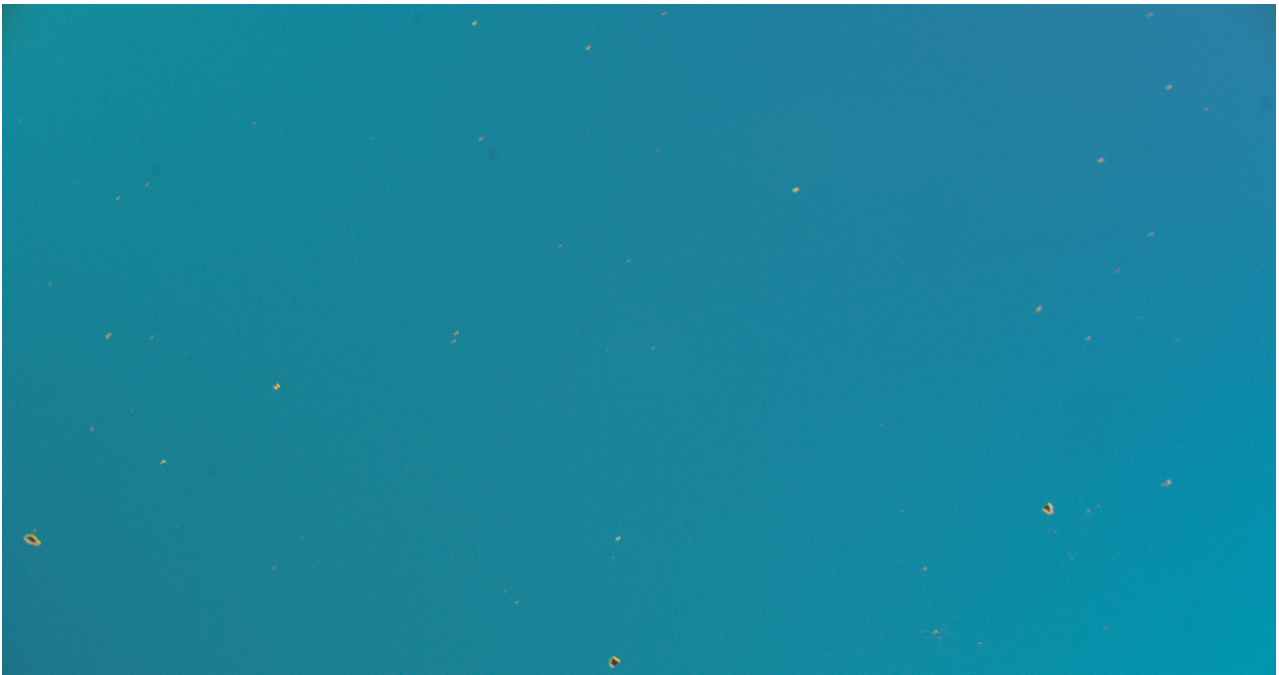
(a)



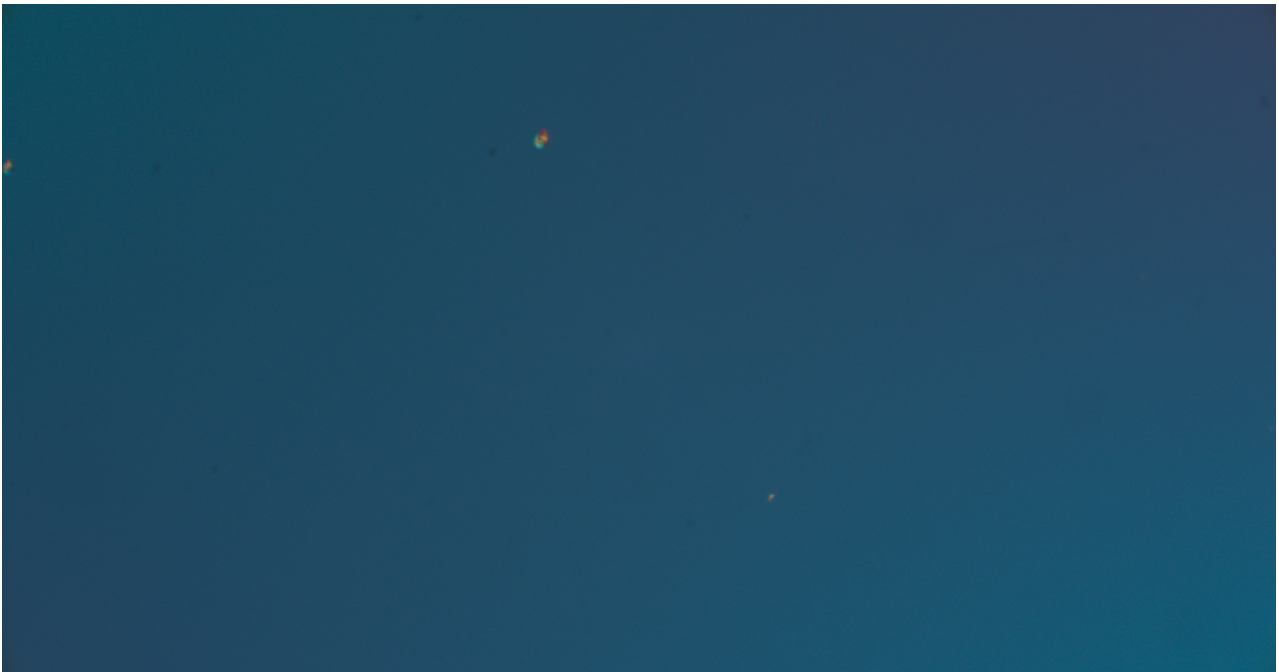
(b)

*Figure 15.7: Nomarski images of STL4H at (a)  $\times 5$  and (b)  $\times 50$  magnification.*

STL4H appears reasonably clear at  $\times 5$  magnification, in Figure 15.7a, although there are a high density of point defects at  $\times 50$  magnification, the cause of which is not known.



(a)



(b)

*Figure 15.8: Nomarski images of STL4J at (a)  $\times 5$  and (b)  $\times 50$  magnification.*

At the highest Al composition of the series, STL4J has a low density of defects and does not display the same high density of point defects at high magnification as STL4H. This indicates that this effect is either unique to Al compositions in a narrow range around 60 %, or, more likely, is the effect of another growth anomaly limited to layer STL4H in the same way that STL47 does not clearly correlate with any other layers.

## 15.2 X-RAY DIFFRACTION RESULTS

The XRD data taken for these layers was in the form of reciprocal space maps (RSMs, 2D images of reciprocal space) around the (004) Bragg reflection of  $GaAs$ . Normally RSMs take many hours to record with a high sensitivity point detector. Instead, through the use of a 1D line-detector and ‘RapidRSM’ feature available on the Bruker D8 XRD system, this data could be recorded in a much shorter time. The benefit to these maps is that they simultaneously record  $\omega - 2\theta$  and  $\omega$  rocking curve scans for each layer, which can be extracted from the bulk data array. Whilst this did necessitate the sacrifice of the larger count rate possible with the 0D point-detector, it did allow accurate rocking curve data to be acquired quickly without requiring lengthy optimisation to find the true  $AlGaAsBi$  peaks which could have shifted with any lattice relaxation. Examples of the successfully extracted  $\omega$  rocking curves are shown in Figure 15.9 for the layers with target  $Al$  compositions of 30%.

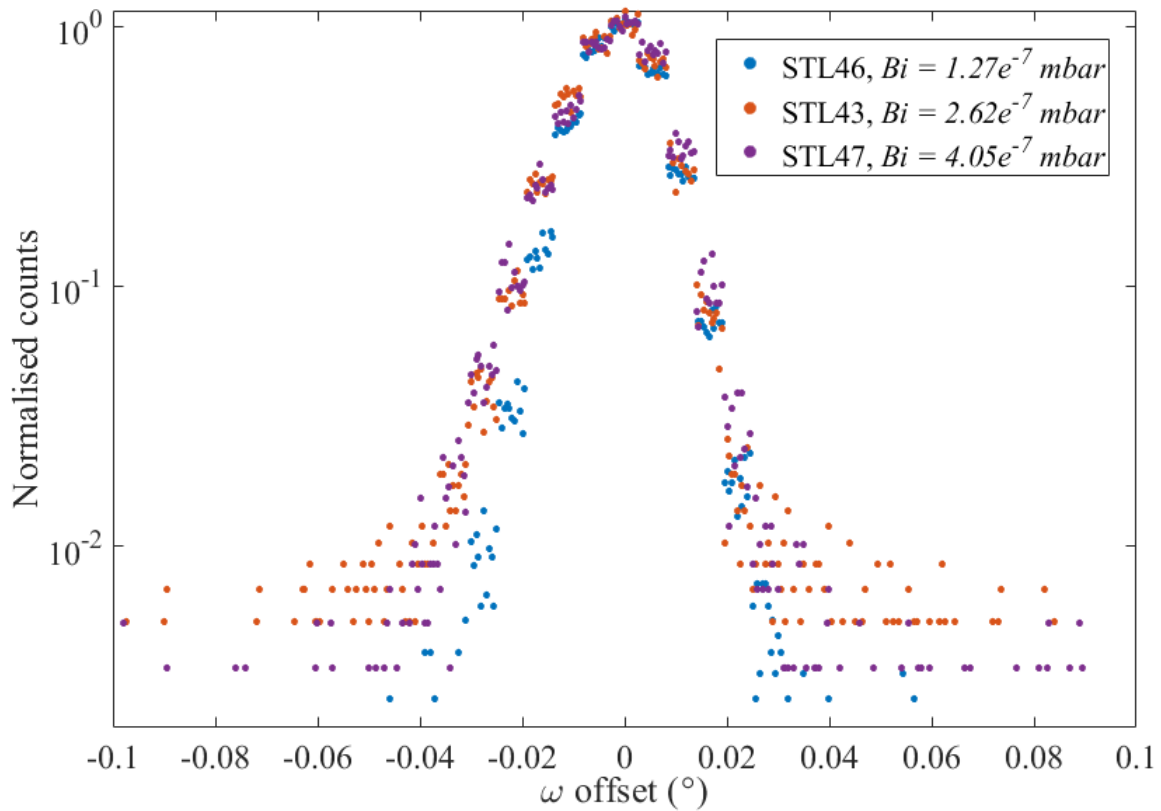


Figure 15.9: Extracted rocking curves for layers  $STL46$ ,  $STL43$  and  $STL47$ .

As seen in Figure 15.9, across these layers there is no significant difference in the rocking curve FWHM and this extends to the rest of the series. The FWHM data for this series is summarised in Table 15.1 where the FWHM for each of the layers was calculated using a Gaussian fit. These values will be compared using the RBS characterisation results further on, along with the  $\omega - 2\theta$  diffraction data which was collected.

Layer	FWHM (arcsec)
STL46	73.8
STL43	64.8
STL47	70.2
STL4A	70.2
STL49	64.8
STL4G	73.8
STL4H	61.2
STL4J	64.8

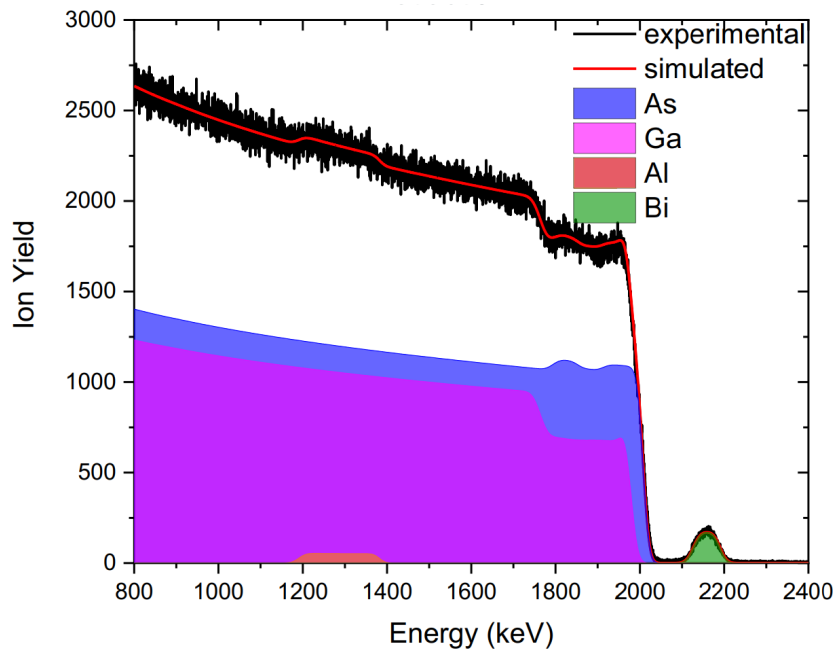
*Table 15.1: Summary of STL<sub>4</sub> rocking curve FWHM.*

### 15.3 RUTHERFORD BACKSCATTERING RESULTS

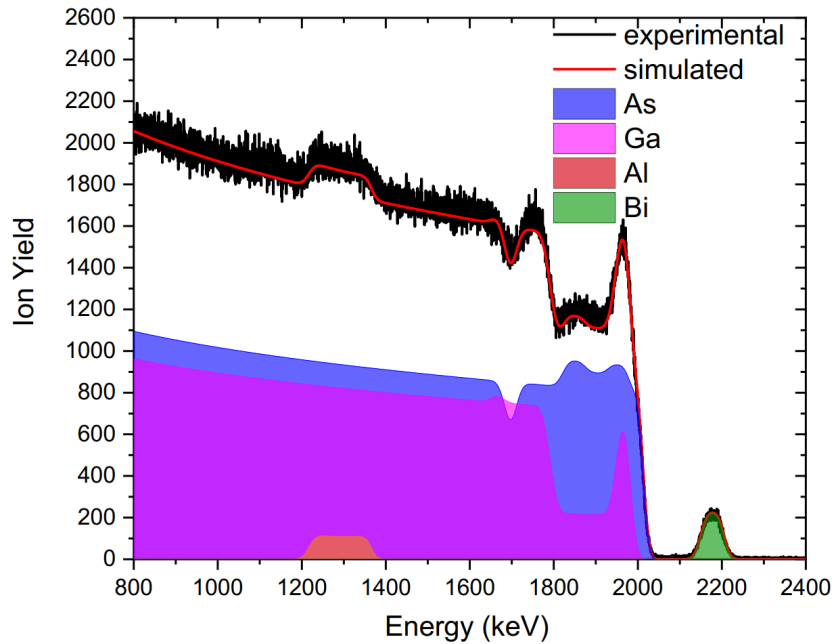
Each wafer was characterised by RBS using two detectors in channelled and random orientations. The results of the fitting to the random orientation data is summarised in Table 15.2 with examples of the raw and simulated data, for STL46 and STL4J, shown in Figure 15.10.

Layer	Al Content (%)	Bi Content (%)	AlGaAsBi Thickness (nm)
STL46	26.2	2.56	102
STL43	36	3.9	98
STL47	24	5	103
STL4A	42	2.24	104
STL49	38	4.5	97
STL4G	42	5.9	105
STL4H	62	4.7	100
STL4J	72	3.66	100

*Table 15.2: Summary of STL<sub>4</sub> RBS characterisation.*



(a)



(b)

Figure 15.10: Experimental RBS spectra of a) STL46 (30 % Al) and (b) STL4J (80 % Al). The Al (orange) peak is almost indistinguishable from the GaAs substrate at the target Al composition of 30 % in STL46 and barely clear in STL4J at 80 %. As the Al content is tied to the decrease in Ga, however, the drop in the Ga signal at 1.8 MeV can be used to increase the accuracy of the fit. Supplied by the Ion Beam Centre, the University of Surrey.

The Al compositions in Table 15.2 are subject to larger uncertainty compared to Bi due to its lower atomic mass. This results in the reflected energy peak for Al being buried in the GaAs substrate signal whereas the Bi, with the largest atomic mass by  $\sim 134$  atomic mass units, has an isolated peak which greatly reduces the uncertainty in its composition. As the increase in Al signal causes a concurrent reduction in the Ga signal, this

can be used in the fitting process to reduce the uncertainty.

Figures 15.10a and 15.10b are representative of fits which were achieved for the whole series and all the layers were reported to be highly crystalline. This is confirmed in Figure 15.11 which indicates the substitutional percentage of *Bi* and other materials. The example here is for STL4G which, despite being the most relaxed layer of the series, maintained  $\geq 92\%$  substitutional rate for *Bi* which is consistent with results obtained for the rest of the layers. It should be noted that the fall-off at lower energies in this figure is due to de-channelling of the *He* ions as they travel deeper into the layer and not due to epilayer defects or otherwise.

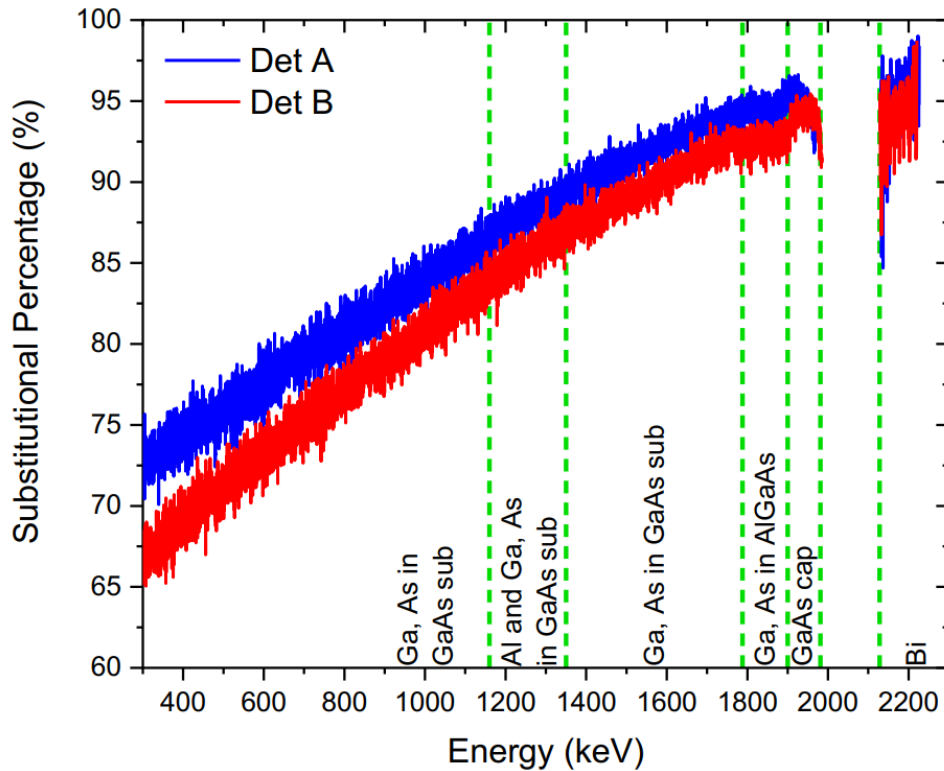


Figure 15.11: Plot of the substitutional percentage against energy. The fall-off at lower energies is caused by de-channelling as the *He* ions travel deeper into the layer and therefore this measurement is most accurate for the *AlGaAsBi* and *AlGaAs* layers near the surface. The substitutional *Bi* % is above 92% which was the case for all the layers. Supplied by the Ion Beam Centre, the University of Surrey.

#### 15.4 XRD AND RBS COMPARISON

One of the interesting comparisons which can be explored in the characterisation for this series of layers is how well the  $\omega - 2\theta$  curves, recorded by XRD, agree with the model structures from RBS. This can be easily tested by simulating the RBS structures and overlaying the curves with the experimental data extracted earlier. At the same time the XRD characterisation values for *Bi* content can also be calculated by fitting the curves freely and comparing the final value to that found by RBS. The lattice constants used for *GaBi* and *AlBi* in this modelling were 6.28 [2] and 6.23 [1] Å, respectively. The results of this analysis is shown in Figure 15.12 and Table 15.3.

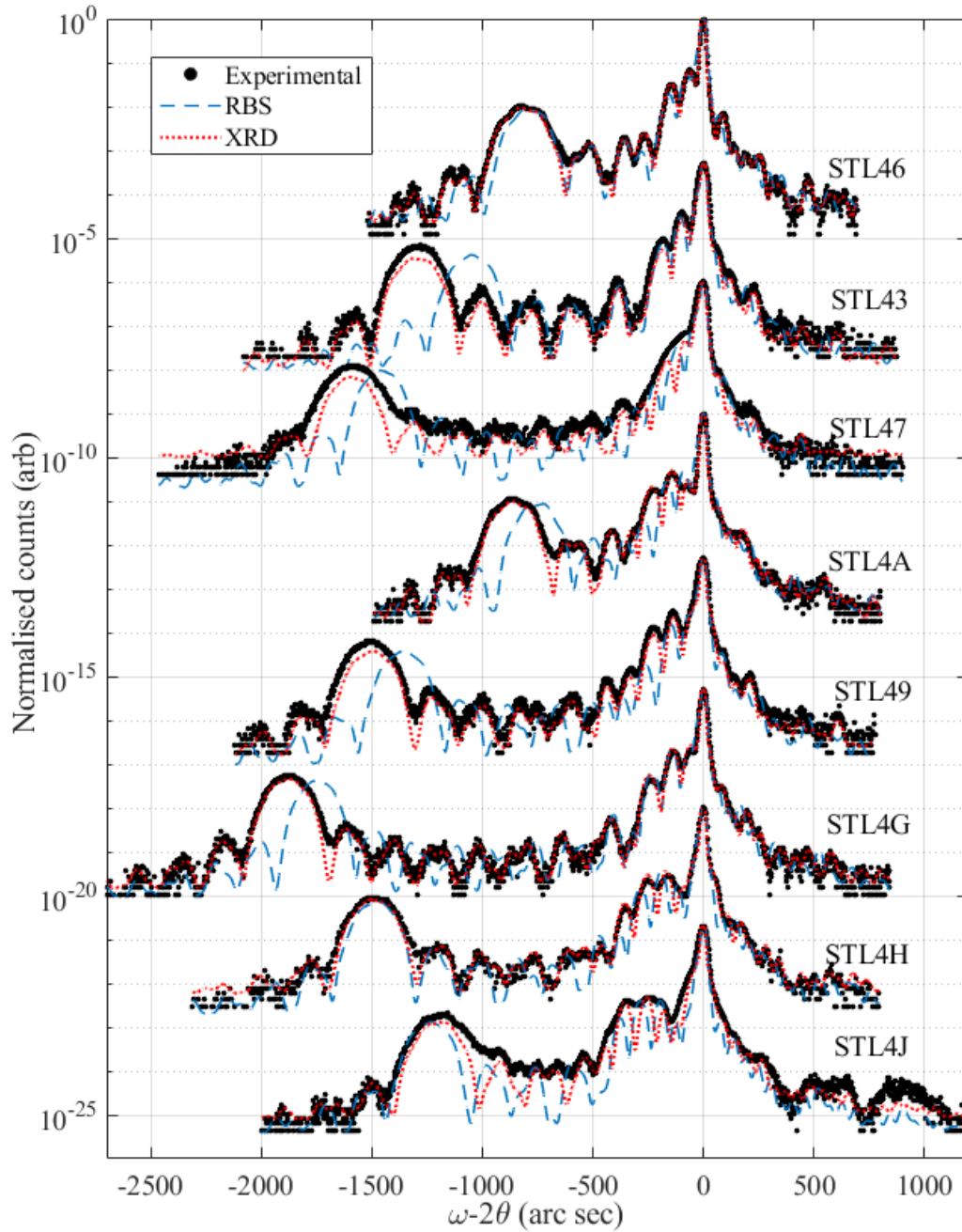


Figure 15.12: Plot of  $\omega - 2\theta$  curves modelled by XRD and RBS. Whilst the RBS results give very close fits for three of the layers, across the series as a whole, it gives a lower estimate for the Bi content than XRD.

Looking at the raw data and RBS fits in Figure 15.12 it can be seen that the RBS structures often do not align with the XRD curves and give a lower estimation for the Bi content. One explanation for this could be inaccuracy in the AlBi lattice parameter which only has one experimental value currently which was based off two layer growths [1]. This may be likely given the RBS and XRD values for Bi content in Table 15.3 show that the XRD generally overestimates the amount of Bi compared to RBS which is considered more reliable in this instance for the reasons discussed for Figure 15.10. Another potential issue is that the uncertainty in the Al peaks and the number of free parameters they offer the XRD modeller, as this may also influence the estimation of layer thicknesses which has a larger impact on the XRD diffraction than the RBS data.

Layer	<i>Al</i> Content (RBS,%)	<i>Al</i> Content (XRD,%)	<i>Bi</i> Content (RBS,%)	<i>Bi</i> Content (XRD,%)
STL46	26.2	26.1	2.56	2.6
STL43	36	34.2	3.9	4.3
STL47	24	25.7	5	5.5
STL4A	42	51.6	2.24	2.5
STL49	38	55	4.5	4.6
STL4G	42	35.2	5.9	6.5
STL4H	62	61	4.7	4.7
STL4J	72	73	3.66	3.5

Table 15.3: Comparison of *Al* and *Bi* compositions of the STL4 layers characterised by RBS and XRD.

Plotting the  $\omega$  rocking curve FWHM values calculated earlier against the *Bi* and *Al* content and characterised by RBS gives the scatter plots displayed in Figure 15.13. It can be seen here that there is no overarching trend in the data with respect to either *Bi* or *Al*. This may suggest that these parameters had little influence compared to the growth temperature, which was in the upper range used for *GaAsBi* to produce high-quality material. Given the thinness of the layers studied here, however, it is likely that not enough growth was performed to see significant differences in their growth quality by this method.

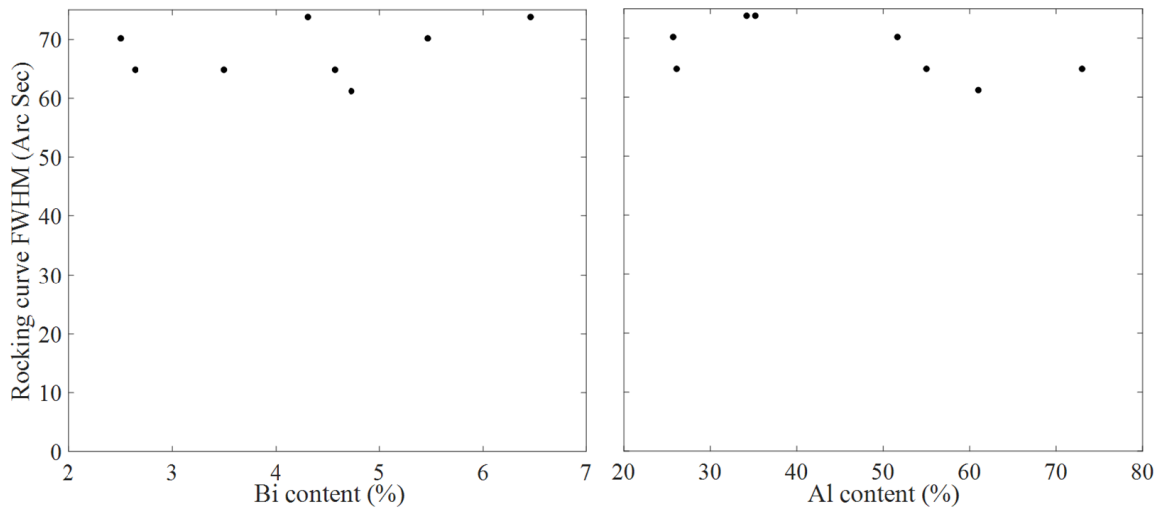


Figure 15.13: Plot of rocking curve FWHM against a) *Bi* content and b) *Al* content. There are no significant trends seen with respect to either element. This is likely due to the low thickness of the *AlGaAsBi* layers.

## 15.5 BISMUTH INCORPORATION IN *AlGaAs*

In order to investigate how *Bi* incorporates into *AlGaAs* compared to *GaAs* a comparison of *Bi* BEP and the resultant *Bi* content was performed between the STL4 layers and the *Bi* BEP subseries of the *GaAsBi* devices discussed in Chapter II. This subseries was ideal for comparison for two reasons. First they were grown in the

same reactor, albeit 6 years prior, and second they were grown at the same nominal temperature which was calibrated in the same way. The variables used are shown in Table 15.4 and the comparison between the two materials shown in Figure 15.15.

Layer	$Bi$ BEP ( $\times 10^{-7} mbar$ )	$Bi$ Content (%) (RBS - STL4) (XRD - STG3)	Growth Rate (ML/s)	Normalised $Bi$ BEP ( $\frac{\times 10^{-7} mbar}{ML/s}$ )
STL46	1.27	2.56	0.45	2.82
STL43	2.62	3.9	0.44	5.95
STL47	4.05	5	0.45	9.00
STL4A	1.27	2.24	0.45	2.82
STL49	2.62	4.5	0.45	5.82
STL4G	5.2	5.9	0.408	12.75
STL4H	2.48	4.7	0.4676	5.30
STL4J	2.48	3.66	0.452	5.49
STG39	2.12	5.37	0.6	3.53
STG3B	1.5	4.12	0.6	2.5
STG34	1.06	3.25	0.6	1.77
STG3A	0.76	2.25	0.6	1.27
STG3D	0.5	1.31	0.6	0.83

Table 15.4: Variables used to calculate  $Bi$  incorporation efficiency for STL4 and STG3 layers. Data for STG3 layers taken from [3]. Growth rate data for the STL4 layers was assumed to match the calibrated values except for some layers where RHEED oscillation data taken for GaAs and AlGaAs beneath the GaAs buffer. STL4G was grown at a lower growth rate than intended due to a recipe error in ramping the Al cell to the correct value.

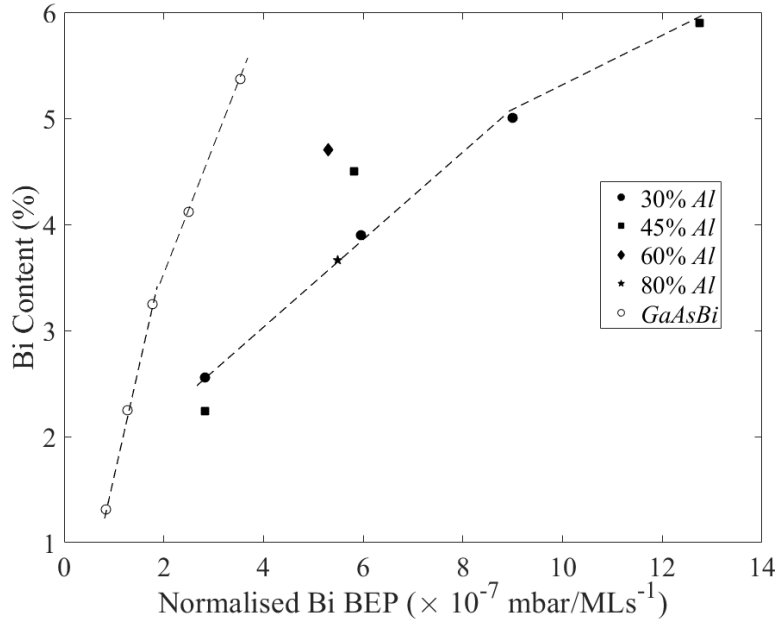


Figure 15.14: Plot of *Bi* content against normalised *Bi* BEP. Whilst the *AlGaAs* layers all have higher normalised *Bi* BEP values, this is expected to be due to ion gauge and cell arrangement changes. The important features to note are the initial linear gradients which both the *AlGaAsBi* and *GaAsBi* series follow and the minor curving of the dashed lines which have been added to guide the eye.

The data in Figure 15.15 has been fitted with lines to indicate how the *Bi* content begins to level off at higher values of  $Bi \times 10^{-7} \text{ mbar/MLs}^{-1}$ . Whilst, due to the scattering of data points for the STL4 layers around  $6 \times 10^{-7} \text{ mbar/MLs}^{-1}$ , it is difficult to estimate a reliable gradient, given that STL4G has at  $\sim 5.9\%$  *Bi* and the highest *Bi* content reported for *GaAsBi* in this temperature range is 5.37% [3], *AlGaAsBi* has already surpassed the ternary alloy. Comparing this layer to a growth overview presented in a recent review paper in Figure 15.15, it can be seen that  $\sim 5.9\%$  *Bi* is also close to the boundary of what is expected for *Bi* content in *GaAsBi* [4]. Also, considering the surface quality observed for STL4G, it is not unreasonable to consider the potential of incorporating more *Bi* at this temperature although thinner *AlGaAs* or *AlGaAsBi* layers would be required to prevent significant relaxation. The overall conclusions from these figures is that *Bi* contents seen in *GaAsBi* can easily be attained with *AlGaAsBi* and there is the implication that the *Bi* content can be taken higher to values which are unobtainable with *GaAsBi* under the same conditions, indicating a higher solubility limit for this new quaternary alloy.

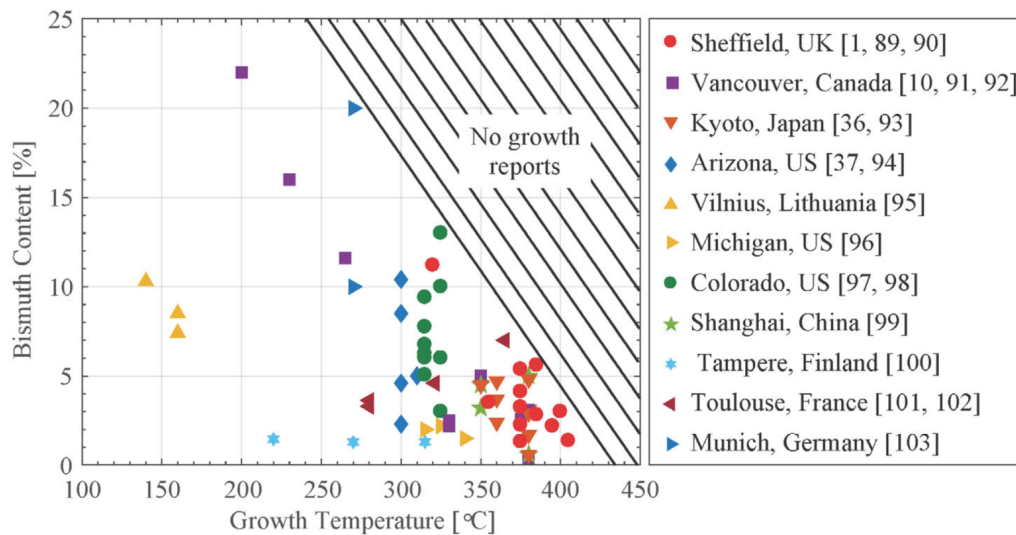


Figure 15.15: Plot of reported GaAsBi growth temperatures and Bi contents from the literature. It can be seen that the values of Bi content for the AlGaAsBi layers discussed here surpass that of those seen for the same growth temperature and, given the clear surface and lack of droplets observed for STL4G in Figure 15.6, higher values may still be possible. Figure taken from [4].

## 16 CONCLUSIONS

In conclusion the scientific interest of aluminium gallium arsenide bismide for advanced avalanche photodetectors has been presented. The growth of a series of layers containing this material has been detailed and it has been seen that bismuth can be readily incorporated into aluminium gallium arsenide at similar temperatures to that used for gallium arsenide. Results obtained from X-ray diffraction and Rutherford backscattering experiments indicate these layers are highly crystalline, with sharp interfaces and with bismuth sitting substitutionally within the host lattice. Finally, high the bismuth composition achieved in layer STL4G without a high density of surface defects suggests the possibility that this new alloy can be used to incorporate more bismuth than possible with gallium arsenide or instead grown at higher temperatures.

## REFERENCES

- [1] C. Wang, L. Wang, X. Wu, Y. Zhang, H. Liang, L. Yue, Z. Zhang, X. Ou, and S. Wang, "Molecular beam epitaxy growth of  $AlAs_{1-x}Bi_x$ ," *Semiconductor Science and Technology*, vol. 34, no. 3, p. 034003, 2019.
- [2] M. Ferhat and A. Zaoui, "Structural and electronic properties of III-V bismuth compounds," *Physical Review B*, vol. 73, no. 11, p. 115107, 2006.
- [3] T. Rockett, R. Richards, Y. Gu, F. Harun, Y. Liu, Z. Zhou, and J. David, "Influence of growth conditions on the structural and opto-electronic quality of GaAsBi," *Journal of Crystal Growth*, vol. 477, pp. 139–143, 2017.
- [4] R. D. Richards, N. J. Bailey, Y. Liu, T. B. Rockett, and A. R. Mohmad, "*GaAsBi*: From Molecular Beam Epitaxy Growth to Devices," *physica status solidi (b)*, p. 2100330, 2021.

## PART V

# CONCLUSIONS

This thesis has presented the theory behind molecular beam epitaxy growth and its use in growing III-V materials containing bismuth. The reasoning for the scientific interest in bismide materials has been discussed with the advantages they offer and the complexities in their growth.

In the first results chapter, a comprehensive photo-luminescence model for low-temperature gallium arsenide bismide material has been developed based on previous literature work and successfully applied to a wide set of semiconductor layers to inform on the effect growth conditions have on gallium arsenide bismide. The implications of this work are that through simple, non-destructive characterisation the device quality of gallium arsenide bismide layer can be qualitatively estimated, allowing for faster growth optimisation at any arbitrary bismuth composition.

The second results chapter discussed a growth study investigating the effect of different bismuth fluxes on the nucleation of indium arsenide quantum dots. The results from this indicated that bismuth can be used to trigger quantum dot formation when it would not normally occur and has consistent effects on quantum dot height. It has also been evidenced that bismuth may be able to control a transition in quantum dot morphology to a higher aspect ratio which could prove instrumental in reliably red-shifting quantum dot emission even further, if proven to be replicable.

In the finally experimental chapter, a fundamental growth study of aluminium gallium arsenide bismide has been presented. The results of this suggest that incorporation into aluminium gallium arsenide is broadly similar to gallium arsenide where bismuth is predominantly substitutional. Bismuth contents above that which have been seen for gallium arsenide bismide suggest the growth temperature limit for this quaternary alloy may be above 400 °C which could be expected to have a higher solubility limit for bismuth.

## PART VI

# FUTURE WORK

There are several directions in which this research could be further explored. These are discussed below in order of which experimental chapter they are most relevant to.

Chapter II - Photo-luminescence modelling of localised states in *GaAsBi*:

- As discussed in Section 3.6.3, *As* overpressure has a significant impact on the solubility of *Bi* outside the stoichiometric ratio. Therefore, instead of using the substrate growth temperature to segregate *Bi* to the surface as in Chapter II, the question which arises is: can *As* overpressure be used to control *Bi*

surface coverage without disrupting the growth process? If so would this allow for  $Bi$  to be controllably segregated to induce a surfactant effect arbitrarily at any  $GaAsBi$  composition and temperature within the flux limited regime.

- So far this model has only been applied to photo-luminescence at low temperatures where the effects of thermal broadening and non-radiative losses can be reasonably ignored. Is it possible, however, to account for these effects and apply the model at higher temperatures which would enable the model to be used for rapid feedback on growth quality without the requirements of a cryostat?

Chapter III -  $InAs$  quantum dots growth under various  $Bi$  fluxes:

- Considering the wide range of growth parameters associated with QD growth, deposition thickness, growth interrupts and  $As$  overpressure to name but a few, the series covered in Chapter III could be considered quite narrow. It is therefore well worthy of a significant growth campaign to see how the use of  $Bi$  can be combined with these other variables, some of which are used to produce the current state-of-the-art devices with low densities and narrow line-widths etc.

Chapter IV - Growth of  $AlGaAsBi$  by MBE:

- As the layers covered in Chapter IV represent one of the first literature reports on growth of this material, there is a lot of fundamental work left to cover. Whilst it is expected from the work discussed in Chapter IV is that there will be significant parallels to  $GaAsBi$  growth. Further fundamental  $AlGaAsBi$  growth investigations (temperature, growth rate,  $As$  overpressure, higher  $Bi$  fluxes etc.) would be most beneficial to continue mapping out the parameter space and critical growth condition limits for this material.
- It was mentioned in Section 2.8.1 that the main scientific interest in  $AlGaAsBi$  is focussed on its potential in avalanche photo-detectors. As characterising this requires fabricated devices, this was not able to be addressed in Chapter IV. Therefore, growth and fabrication of doped structures are needed in order to investigate how well this material performs.

## REFERENCES

## GLOSSARY

- AFM** Atomic Force Microscopy, a topographical surface characterisation technique. Can be performed in vacuum or ambient and is often used to investigate the morphology of semiconductor quantum dots. 60
- AlAs** Aluminium arsenide, a III-V semiconductor. 18
- APD** Avalanche Photo-Diode, a high sensitivity photo-diode which produces internal amplification of photo-excited electrical signals through the impact ionisation effect. 29
- Be** Beryllium, a group II element. Commonly used as a p-dopant in gallium arsenide and other materials. 19
- Bi** Bismuth, a group V metal. The heaviest element with stable isotopes. 14
- DBR** Distributed Bragg Reflector, a semiconductor mirror produced using near lattice-matched materials with different refractive indices. These are of great importance for state-of-the-art optoelectronics, particularly vertical-cavity surface-emitting lasers. 26
- EDX** Energy Dispersive X-ray spectroscopy, a chemically sensitive technique for identifying elemental fractions within a sample. 62, 79
- FEL** Fast Entry Load-lock, the smallest chamber on MBE reactors. Through this chamber finished layers and fresh substrates are exchanged and therefore this chamber is regularly exposed to ambient conditions.. 33
- GaAs** Gallium arsenide, a III-V semiconductor. 14
- GaAsBi** Gallium arsenide bismide, a III-V semiconductor formed through alloying of gallium arsenide with bismuth during growth. 26
- InAs** Indium arsenide, a III-V semiconductor. 14
- LED** Light Emitting Diode, a electronic device composed of a direct band gap semiconductor doped to form a PN junction. Indirect band gaps can be used but are as much use as a paper umbrella. 22
- MBE** Molecular Beam Epitaxy, a growth process which takes place in an ultra-high vacuum chamber containing ultra-high purity elemental sources. 14
- PL** Photo-Luminescence, a characterisation technique using optical excitation of carriers leading to recombination and photon emission within a semiconductor. 47
- QD** Quantum Dot, a nanoscale semiconductor structure which approximates confinement of a carrier in three dimensions. Often synthesised through strain-induced self-assembly, their dimensions are typically  $\sim 20\text{ nm}$  vertically with diameters  $\sim 50\text{ nm}$ . 23, 93

- RBS** Rutherford Backscattering Spectroscopy, a material characterisation technique utilising accelerated helium nuclei. Named after experiments in the early 20th century which led to the discovery of the positively charged atomic nucleus. 58
- RHEED** Reflection High-Energy Electron Diffraction, a diffraction imaging technique used on almost all molecular beam epitaxy reactors. Utilises a focused beam of electrons accelerated to  $keV$  energies directed onto a semiconductor surface. Produces reciprocal space images of surface reconstructions and can be used to measure semiconductor growth rates and monitor surface structure. 38
- RMSE** Root Mean Square Error, a statistical value used to measure the discrepancy between two pieces of data. Represented mathematically as  $\sqrt{(a - b)^2}$ . 77
- RSM** Reciprocal Space Map, a two-dimensional X-ray diffraction image taken of the reciprocal space for a semiconductor. Normally constructed from a series of one-dimensional scans using a high-sensitivity point-detector or a single scan using a line detector. These images can be used to examine strain and relaxation of complex semiconductor structures. 56
- Sb** Antimony, a group V metal sitting above bismuth. 14
- SEM** Scanning Electron Microscopy, a high resolution imaging technique which surpasses standard optical microscopes. 61
- Si** Silicon, a group IV element. The most processed material in the semiconductor industry but also a common n-dopant for gallium arsenide and other semiconductors. 19
- SK** Stranski Krastanov, referring to a semiconductor growth process reported by Ivan Stranski and Lyubomir Krastanov in 1938. Often used to describe quantum dot growth in semiconductor physics. 24
- UI** User Interface, a graphical display of data and functions designed to make programs more accessible and easy to use. 76